

AN ABSTRACT OF THE THESIS OF

James H. Vlieg for the degree of Master of Science in Industrial Engineering
presented on June 10, 2010.

Title: Development of a Radial Microlamination Architecture for Cylindrical Microchannel Arrays.

Abstract approved:

Brian K. Paul

Microchannel arrays are being developed across a wide spectrum of microfluidic applications including blood processing, fuel cells and thermal management among many others. Typical arrays are based on a flat laminated architecture produced in a vacuum hot press (VHP) through solid-state diffusion bonding. Due to the cylindrical nature of certain microfluidic applications, such as chemical processing within chemical facilities and heat rejection within Stirling cycle engines, the packaging of microchannel devices within cylindrical geometries would greatly simplify interconnect to other systems and expand practical application. This thesis describes the development of a novel technique for axisymmetric diffusion bonding capable of producing cylindrical microchannel arrays. Uniaxial bonding pressure is converted to axisymmetric pressure through an expandable cylinder, the design of which was aided by finite element analysis. Cylindrical test articles were produced by patterning thin

metal foils by laser machining a single roll of metal shim stock, which was then coiled within an outer tube shell and axisymmetrically bonded with a VHP to produce a cylindrical microchannel array. Further, a mathematical model was developed to provide a means of channel alignment during device design. Bonding results show quality bond lines with minimal void fractions and good agreement with the channel alignment model. This new architecture provides a robust means for producing cylindrical microfluidic devices by microlamination using traditional equipment.

© Copyright by James H. Vlieg
June 10, 2010
All Rights Reserved

Development of a Radial Microlamination Architecture for Cylindrical
Microchannel Arrays

by
James H. Vlieg

A THESIS
submitted to
Oregon State University

in partial fulfillment of
the requirements for the
degree of

Master of Science

Presented June 10, 2010
Commencement June 2011

Master of Science thesis of James H. Vlieg presented on June 10, 2010.

APPROVED:

Major Professor representing Industrial Engineering

Head of the School of Mechanical, Industrial, and Manufacturing Engineering

Dean of the Graduate School

I understand that my thesis will become part of the permanent collection of Oregon State University libraries. My signature below authorizes release of my thesis to any reader upon request.

James H. Vlieg, Author

ACKNOWLEDGEMENTS

I would foremost like to communicate my deepest gratitude to Dr. Brian Paul for his valuable guidance as my major professor and research advisor. I have benefited professionally and personally from our cordial relationship, and I will always be grateful that he presented the opportunity for me to learn about and contribute to such an exciting and promising field of manufacturing.

My deepest thanks are further extended to my minor professor, Dr. Richard Peterson, for his considerable support and encouragement of this work. I offer my sincerest appreciation also to the rest of my committee, Dr. Karl Haapala and Dr. Goran Jovanovic, for continued guidance and encouragement. And special thanks are due to Dr. Bill Warnes for his valuable advice on so many occasions.

I would like to also offer genuine gratitude to Dr. Jack Rundel and Mr. Steve Etringer for their invaluable technical laboratory support at the Microproducts Breakthrough Institute throughout all stages of this thesis, as well as for their advice and interminable patience.

I am also truly appreciative of the help and friendship of the members of my research group, with whom I look forward to maintaining lasting personal and professional relationships.

I am so grateful for the support of all of my friends and family as well, and especially for my parents, Diane and Henry Vlieg, for their ceaseless love, encouragement, and support in all ways.

Finally, and most importantly, I would like to thank my partner, Cristy Coughlin, for her endless love and support. Hopefully this thesis is the first step in gaining a fraction of her brilliance.

TABLE OF CONTENTS

1. Introduction	1
2. Background and Literature Review.....	3
<i>2.1. Microfluidic Technology.....</i>	<i>3</i>
<i>2.2. Microlamination</i>	<i>4</i>
<i>2.3. Applications.....</i>	<i>6</i>
<i>2.4. Radial Diffusion Bonding.....</i>	<i>7</i>
3. Pressure Delivery System Design and Analysis	9
<i>3.1. Pressure.....</i>	<i>9</i>
<i>3.1.1. Limits on Pressure Magnitude</i>	<i>9</i>
<i>3.1.2. Pressure Distribution Discussion</i>	<i>10</i>
<i>3.2. Design Evolution.....</i>	<i>11</i>
<i>3.2.1. Concept 1: Differential Thermal Expansion.....</i>	<i>11</i>
<i>3.2.2. Concept 2: Pneumatic Expansion Spring</i>	<i>13</i>
<i>3.2.3. Concept 3: Wedge-Driven Expansion Spring.....</i>	<i>15</i>
<i>3.2.4. Concept 4: Multi-Component Platen System</i>	<i>16</i>
<i>3.3. Materials</i>	<i>16</i>
<i>3.4. Detailed Final Design</i>	<i>17</i>
<i>3.4.1. Platens.....</i>	<i>18</i>
<i>3.4.2. Conical Wedges</i>	<i>21</i>
<i>3.4.3. Shell Reinforcement.....</i>	<i>21</i>
<i>3.4.4. Diffusion Barrier</i>	<i>25</i>

TABLE OF CONTENTS (CONTINUED)

3.5. <i>Channel Alignment Model</i>	27
3.6. <i>Device Design Procedure</i>	30
4. Experimental Investigation	32
4.1. <i>Overview</i>	32
4.2. <i>Lamina Fabrication and Preparation</i>	32
4.3. <i>Process Parameters</i>	34
4.3.1. Bonding Environment	35
4.3.2. Surface Conditions	35
4.3.3. Temperature	36
4.3.4. Pressure and Time	37
4.3.5. Metallographic Preparation	40
4.3.6. Creep of Steel Platens.....	41
4.4. <i>Pressure Magnitude and Distribution Experiment</i>	41
4.4.1. Test Article Design.....	41
4.4.2. Experimental Design.....	42
4.4.3. Void Fraction Measurement	42
4.4.4. VHP Pressure Validation.....	43
4.5. <i>Channel Alignment Experiment</i>	44
4.5.1. Test Article Design.....	44
4.5.2. Experimental Design.....	45

TABLE OF CONTENTS (CONTINUED)

5. Results and Discussion.....	46
<i>5.1. Pressure Delivery.....</i>	46
5.1.1. Void Fraction Results.....	46
<i>5.2. Channel Characteristics.....</i>	48
5.2.1. Channel Alignment Results	49
5.2.2. Effects of Misalignment	50
5.2.3. Effects of Channel Aspect Ratio.....	52
5.2.4. Defect Mode: Direct Pressure Transmission	54
5.2.5. Summary of Channel Characteristic Tests	55
<i>5.3. Application of Alignment Model.....</i>	55
5.3.1. Geometry Measurement Precision	57
5.3.2. Non-Linearity of k Value in Model	59
6. Conclusions.....	61
<i>6.1. Key Findings.....</i>	61
<i>6.2. Recommendations for Future Work.....</i>	61
7. References	64
8. Appendices.....	68

LIST OF FIGURES

Figure 2-1. Spectrum of microfluidic applications.	3
Figure 2-2. Schematic of traditional microlamination architecture.	5
Figure 2-3. Cross section of Stirling engine (courtesy Infinia, Inc.).	6
Figure 3-1. Example of slightly maldistributed pressure falling within pressure limits.	11
Figure 3-2. Fabrication setup for preliminary CTE tests.	12
Figure 3-3. Effect of varying copper tube OD on expansion pressure for preliminary CTE tests.	13
Figure 3-4. Example of one of the pneumatically driven expansion cores simulated (half section).	14
Figure 3-5. Example of one-piece tapered wedge driven expansion core (half section).	15
Figure 3-6. Final design for expandable core.	18
Figure 3-7. Tangential FEA contact results at (a) end of device, and (b) center of device.	19
Figure 3-8. FEA contact stress results along axial direction, from center to edge of device.	20
Figure 3-9. Various thicknesses of TiN reactive sputter films.	26
Figure 3-10. (a) Rotation fixture with platens attached, (b) BN application environment, and (c) results of BN application.	27
Figure 3-11. Micrograph showing the overlap interface as well as the gap.	30

LIST OF FIGURES (CONTINUED)

Figure 3-12. Design concept where layers are designed separately, scaled, and placed end-to-end.	31
Figure 4-1. Channel edge profile after laser machining.	33
Figure 4-2. Channel edge profile after de-burring procedure.	34
Figure 4-3. Creep map for pure copper [40].	39
Figure 4-4. Test article design for first series of bonding runs.	42
Figure 4-5. Test article for second run of bonding tests.	44
Figure 5-1. Void fraction results for each sample measured, shown at center and edge of sample.	47
Figure 5-2. Overall void fraction results for edge and center locations, as well as results by Pluess [4].	48
Figure 5-3. Channel misalignment vs k value, with 95% confidence intervals.	49
Figure 5-4. Resulting channel height vs channel misalignment, with 95% confidence intervals.	50
Figure 5-5. Channel warpage in order of increasing misalignment for 10:1 aspect ratio channels.	51
Figure 5-6. Channel height vs channel aspect ratio, with 95% confidence intervals.	52
Figure 5-7. Channel misalignment vs channel height by aspect ratio.	53
Figure 5-8. Standard deviation of channel misalignment by aspect ratio.	54

LIST OF FIGURES (CONTINUED)

Figure 5-9. Sensitiviy plot of the effect of mismeasurement of sheel ID.	58
Figure 5-10. Micrograph of header region in final alignment test.	59
Figure 5-11. Misalignment of header region.	60

LIST OF TABLES

Table 3-1. High-temperature (800° C) properties of materials.	17
Table 4-1. Laser mill parameters for 203-μm copper through-cut.	33
Table 5-1. Results of final alignment model confirmation tests.	56

Development of a Radial Microlamination Architecture for Cylindrical Microchannel Arrays

1. INTRODUCTION

Over the past several years, there has been a growing research effort in the development of arrayed microchannel manufacturing technology for producing Microchannel Process Technology (MPT), also known as Micro Energy and Chemical Systems (MECS). MPT is being developed across a wide variety of applications including blood processing, fuel cells, and thermal management, among many others. MPT devices are microfluidic systems with the ability to process bulk volumes of fluid within highly parallel microchannel arrays. Small characteristic sizes are enabled by high surface-to-volume ratios, laminar flow conditions, and accelerated heat and mass transfer [1].

A common fabrication architecture used to produce MPT devices is called microlamination. Microlamination involves the patterning, alignment (or registration), and bonding of individual layers of material, called laminae. This process produces monolithic, multi-layered devices with complex shapes, internal cavities, flow chambers, and interconnects suitable for microfluidic applications. Figure 2-2 displays a schematic of a traditional microlamination architecture.

The bonding step of microlamination is commonly realized through solid-state diffusion bonding. Diffusion bonding is traditionally achieved in a vacuum hot press (VHP) through uniaxial loading at elevated temperature under vacuum. This method

of pressure application imposes inherent geometry constraints on the device being fabricated. More specifically, geometry is limited to planar, two-dimensional forms. Many traditional macro-scale fluidic devices diverge from planar geometries to cylindrical or tubular forms, such as in single-piston Stirling engines. Figure 2-3 shows a cylindrical heat exchanger within a Stirling engine.

Adaptation of microlamination to cylindrical geometry would offer cylindrical devices, such as heat exchangers in Stirling engines among many others, the benefits of increased efficiency and miniaturization offered by MPT. Therefore, the objective of this thesis is to develop a robust fabrication architecture capable of producing cylindrical microchannel arrays. This manuscript documents the following successful efforts: design and development of a suitable axisymmetric pressure application system within a VHP and the development and experimental investigation of a mathematical model for proper alignment of embedded microchannels.

2. BACKGROUND AND LITERATURE REVIEW

2.1. Microfluidic Technology

Microfluidic technology has been a topic of research for decades. Microchannels are commonly accepted as being defined by hydraulic diameters under 200 μm [2], and generally offer many benefits including increased mass and heat transfer. Generally, microfluidics can be divided into two major categories offering different advantages and constraints: analytical microfluidics and arrayed microfluidics. Figure 2-1 illustrates the broad suite of applications involving microfluidic technology.

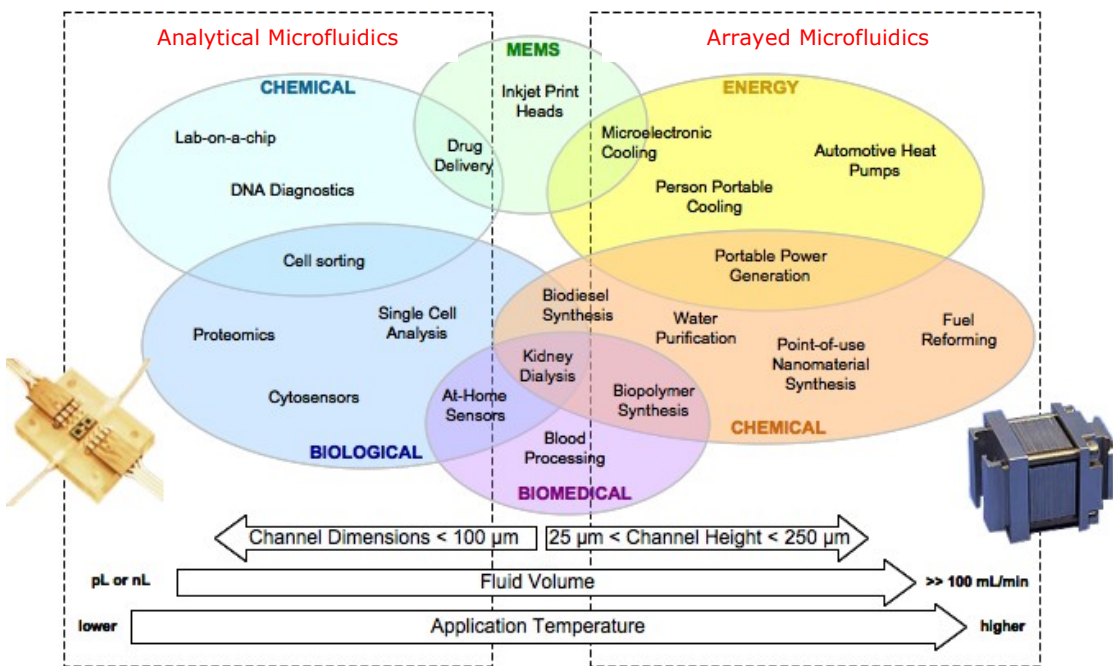


Figure 2-1. Spectrum of microfluidic applications.

The devices and applications on the two sides of the diagram in Figure 2-1 vary significantly in function and fabrication methods. Analytical microfluidics is applied to batch analysis of samples, typically in the chemical, biological and medical fields. These applications tend to run at low pressures, at or near room temperature, and tend to require high levels of precision, control, and sensing, and therefore commonly utilize polymers or silicon microfabrication architectures. In contrast, arrayed microfluidic systems process bulk amounts of fluid in continuous processes. They are typically fabricated using microlamination architectures and can operate at high pressures and temperatures, utilizing common engineering materials such as metals and polymers.

2.2. *Microlamination*

Microlamination involves the patterning, registration, and bonding of thin layers of materials, known as laminae, to produce multi-layered microchannel arrays [1]. Patterning can be performed by laser machining, chemical etching, and other machining, molding or forming techniques. Registration, or alignment, of laminae is commonly achieved by the use of alignment pins. Bonding is typically performed in a hydraulic vacuum hot press (VHP), whereby uniaxial pressure is delivered to the lamina stack under vacuum at high bonding temperatures. This process is known as solid-state diffusion bonding. Use of a transient liquid-phase interlayer to accelerate diffusion is known as diffusion brazing. Developments in microlamination techniques

aim to improve economics. Bose [3] has demonstrated an internal convective heating technique for accelerating the diffusion bonding microchannel arrays. Pluess [4] demonstrated a method for replacing the capital-intensive VHP with a differential thermal expansion fixture for pressure application.

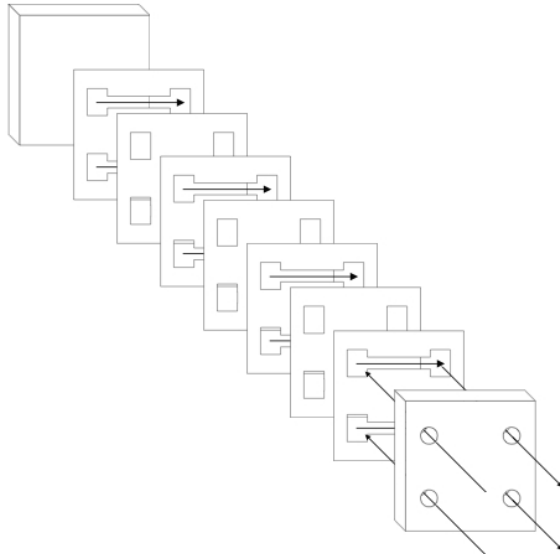


Figure 2-2. Schematic of traditional microlamination architecture.

Solid-state diffusion bonding relies on the Brownian motion of atoms across faying surfaces to fuse materials together into monoliths. Engineering metals, such as stainless steel, copper, and nickel, are the most common base materials used in microlamination and MPT.

2.3. Applications

Traditional radial and cylindrical fluidic systems are numerous. Heat management systems are perhaps the most common application of this geometry. For example, the blue section of the Stirling engine shown in Figure 2-3 represents a cylindrical heat extractor on the cold side of the system, through which the piston displaces and heat is removed. Further, though, Rohsenow et al. [5] has sub-classified cylindrical, or in their terms “tubular”, heat exchangers into double-pipe, shell-and-tube, and spiral plate categories. With proper design, the cylindrical microlamination architecture presented in this thesis should enable the miniaturization of these forms.

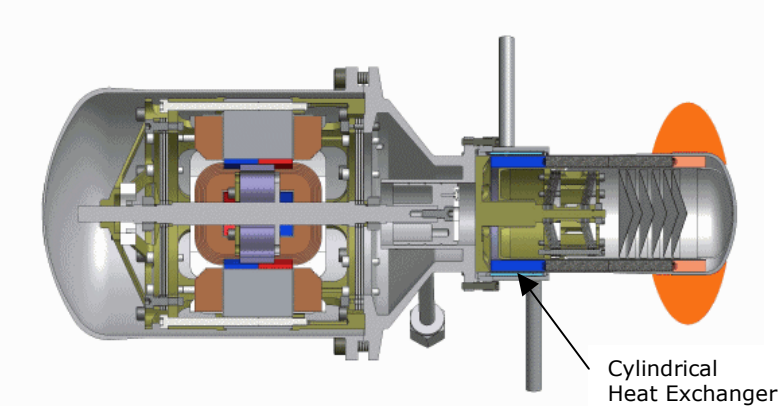


Figure 2-3. Cross section of Stirling engine (courtesy Infinia, Inc.).

Other forms of microfabrication have also been applied to radial heat management systems. Tew et al. [6] proposed and tested a series of cylindrical microchannel regenerators for Stirling cycle applications based on an involute-foil geometry. The design was intended to replace and improve upon common random-fiber regenerators.

The fabrication approach utilized LIGA, which involves electroforming around a polymer mandrel and is limited in material selection and cost effectiveness.

2.4. Radial Diffusion Bonding

Various diffusion bonding methods have been demonstrated for producing cylindrical geometries. During design development for the International Thermonuclear Experimental Reactor (ITER), Visca and colleagues [7][8] developed a method for radially bonding a copper alloy tube within a round hole in a tungsten block using an interlayer and high internal pressure. Differential thermal expansion was also described in later work to aid in the application of radial pressure [9]. The setups used for these designs, however, relied on deformations of the tube walls, which had no internal features. Deformation of microchannel fins by buckling and other phenomena has been shown to cause flow maldistribution in MPT applications, significantly decreasing the efficiency and function of devices [10].

The patent literature contains a number of methods to produce compound cylinders through diffusion mechanisms. Many involve mismatched coefficients of thermal expansion, followed by heating, for radial pressure application [11][12][13][14]. Others require composite cylinders to be drawn or extruded in order to initiate close contact and interfacial stress, followed by heating to induce interfacial diffusion [15][16]. Both of these approaches are not highly controlled and could induce fin warpage and yielding.

Quinby's patent [17] utilizes a conical wedge design to apply radial pressure to a uranium foil in a hot press to support diffusion brazing. However, diffusion brazing can be less attractive for radial geometries, the curved surfaces of which would be more difficult to apply brazing interlayer (typically by electroplating). Further, diffusion brazing of high-temperature components (as in Stirling cycle engines) can lower operating temperature limits [1]. Finally, Quinby's patent did not demonstrate the ability of this pressure delivery mechanism to provide the required stress distributions necessary to produce cylindrical microchannel components.

No cylindrical MPT devices fabricated by diffusion bonding have been reported. Prior literature would suggest that the diffusion bonding of microchannel structures requires the precise control of pressure delivery and stress distribution within the device being bonded. Pressure delivery and stress distribution within a cylindrical MPT device during bonding is particularly challenging. The objective of this research is to demonstrate a reliable method of producing cylindrical microchannel arrays via diffusion bonding. This objective will include the need to develop a reliable method to deliver axisymmetric pressure during cylindrical diffusion bonding. Attainment of these objectives will provide a new architecture for the fabrication of cylindrical microchannel arrays.

3. PRESSURE DELIVERY SYSTEM DESIGN AND ANALYSIS

3.1. *Pressure*

The solid-state diffusion bonding process requires the control of five process variables: time, temperature, surface conditions, bonding environment, and pressure. The system described in this chapter controls all of these variables precisely as they have been with traditional arrayed microchannel manufacturing, with the exception of pressure delivery. Pressure magnitude and pressure distribution must be considered for the proper bonding of laminated structures. The following sections discuss pressure in more detail.

3.1.1. *Limits on Pressure Magnitude*

The role of pressure in diffusion bonding is to deform the asperities on the surfaces of laminae to be bonded, providing intimate contact and helping to initiate grain boundary formation. The magnitude of pressure required to perform this task can be considered a lower pressure limit for the bonding process. Sharp et al. [18] have modeled material response to plastic indenture, and Orhan et al. [19] have adapted this model for predicting surface stresses required to form intimate contact at the surface interface for diffusion bonding. However, these models are highly complex and were not utilized for this thesis. A more useful approach for determining lower pressure limits has been empirical, as exemplified by Islam and Ridley [20] and Pluess [4].

Determination of an upper limit on pressure magnitude is a more complex question as a number of mechanisms lead to failure of arrayed microchannel devices under excessive bonding pressure, as defined by various measures. These failure sources include the following: misregistration of microchannels [21], non-uniform diffusion mechanisms [22], thermal gradients in the arrayed structure during bonding [3], side loading of laminae during bonding [23], effects due to Poisson's ratio [24], and creep [3]. Misregistration is not a function of pressure magnitude, non-uniform diffusion mechanisms apply only to reactive diffusion, and side loading and Poisson's ratio effects are only relevant in traditional planar geometries with uniaxial bonding. Therefore, creep is the only remaining source of failure that is a known potential defect mode for cylindrical bonding of arrays, and can be considered an upper limit which should not be breached if possible.

3.1.2. Pressure Distribution Discussion

Because it is possible to establish lower and upper limits for pressure, it is then possible to more fully understand the role of pressure distribution. Poor pressure distribution is a common claim for poor bonding results [4]. However, the cause of poor bonding is simply localized regions of low or high pressure, falling below or above the limits previously established, within the greater pressure region. Therefore, slight pressure maldistribution can still produce good bonding results so long as pressure does not fall outside the limits in any region. This concept is illustrated in

Figure 3-1. Thus, a requirement for the pressure delivery system developed for this thesis was to deliver pressure within this limiting pressure regime.

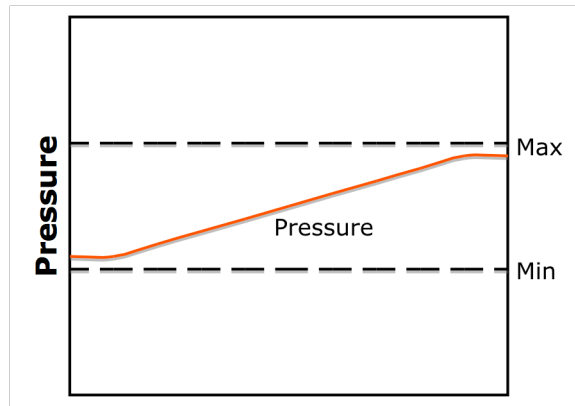


Figure 3-1. Example of slightly maldistributed pressure falling within pressure limits.

3.2. Design Evolution

Given these pressure constraints and the extensive review of the literature, a series of designs was explored that were to deliver pressure to a cylindrical array properly. The designs developed in a sort of evolution, whereby individual failure modes and other limiting factors were extracted and eliminated between design steps. The following sections summarize each step in this evolution.

3.2.1. Concept 1: Differential Thermal Expansion

In order to obtain axisymmetric pressure application inside a cylindrical microchannel array, it was initially conceived that layering cylinders with differing coefficients of thermal expansion (CTE), followed by heating to bonding temperatures, would be an

elegant and sufficient solution. Preliminary tests were run, with the fabrication setup as illustrated in Figure 3-2. An inner, high-expanding copper tube (CTE at high temperatures about $23.2\text{e-}6 \text{ mm/mm}^{\circ}\text{C}$) and a low-expanding outer tube of pure zirconium (CTE about $7.6\text{e-}6 \text{ mm/mm}^{\circ}\text{C}$) were used to bond cylindrical copper laminae. Results were poor. The reasons for poor bonding under these conditions are numerous. Most importantly, in order to achieve the proper theoretical pressures for bonding, extremely precise tube geometries would be necessary, beyond practicality. In fact, for the geometry used for these tests, a $25.4\text{-}\mu\text{m}$ (0.001-in) tolerance on the outer diameter of the inner copper tube produces a 2.9-MPa (421-psi) difference in expansion pressure between the lower and upper tolerance limits, based on ductile material mechanics theory. To more effectively show this sensitivity, Figure 3-3 illustrates the effect of varying outer copper tube diameter on expansion pressure of the setup.

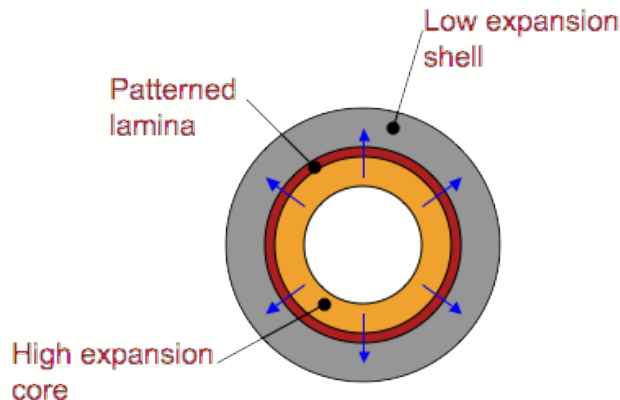


Figure 3-2. Fabrication setup for preliminary CTE tests.

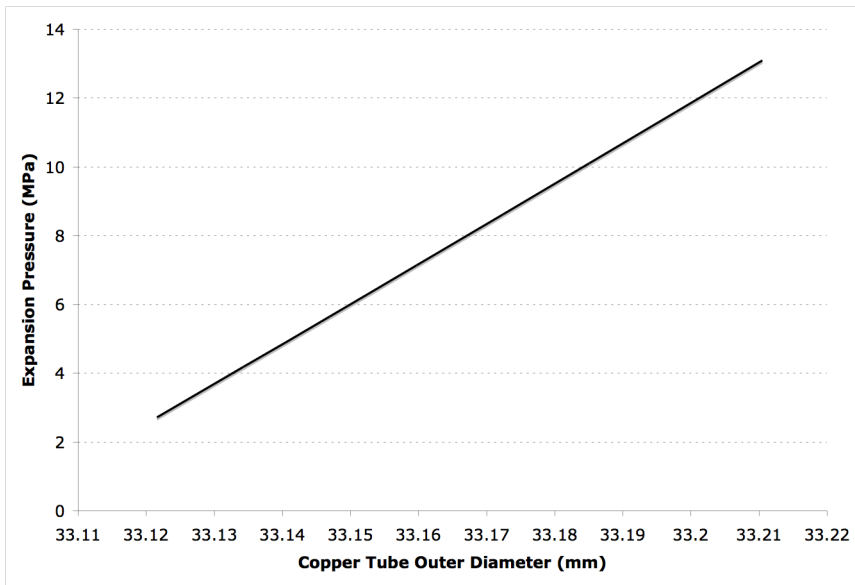


Figure 3-3. Effect of varying copper tube OD on expansion pressure for preliminary CTE tests.

3.2.2. Concept 2: Pneumatic Expansion Spring

A second concept for uniform pressure delivery for radial arrayed microchannels was to apply pneumatic pressure within an expansion diaphragm. Figure 3-4 exemplifies one of the configurations developed during the design process for this diaphragm. Design requirements for the diaphragm were as follows: (a) to supply sufficient assembly clearance for insertion of the diaphragm into the device setup prior to bonding, (b) to expand the radial distance of this clearance under pneumatic pressure to contact the device setup during bonding (therefore allowing the pneumatic pressure to serve as bonding pressure), and (c) to avoid yield or creep issues at high bonding temperatures (in the range of 500-1000° C) completely. Requirement (c) calls for a

high-temperature material in order to avoid yielding and creep at bonding temperature, while requirement (b) requires a low-modulus material in order to expand a sufficient distance to overcome assembly clearance. These requirements are somewhat conflicting and FEA-supported designed failed to produce a design that came close to meeting them. The driving reason for this was material constraints. Any material, such as steel, with high temperature properties sufficient to hold its strength under bonding conditions for a lower temperature material like copper simply would not be ductile enough to overcome assembly clearances of about 500 μm [25]. The design requirements could not be met on the scale of microlaminated device fabrication. Further, this design did not offer the many benefits of using traditional VHP equipment for process control.

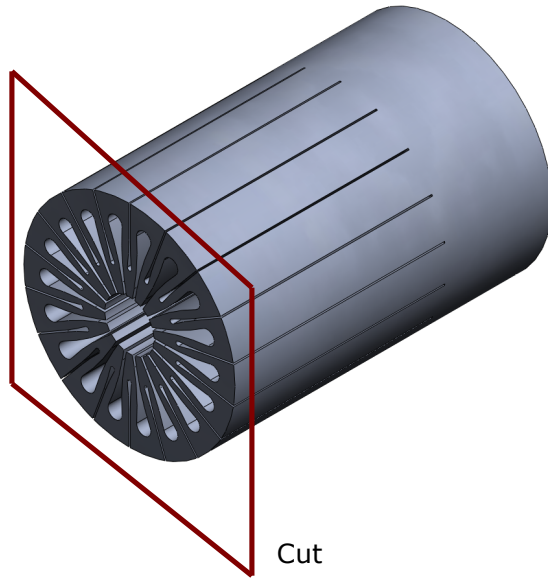


Figure 3-4. Example of one of the pneumatically driven expansion cores simulated (half section).

3.2.3. Concept 3: Wedge-Driven Expansion Spring

A third concept for an expansion spring was developed. Rather than pneumatic pressure driving the expansion, however, tapered wedges, in the shape of truncated cones, were designed to contact tapered holes in the spring, as illustrated in Figure 3-5. Design requirements were similar to the pneumatic design: (a) to supply assembly clearance, (b) to expand a sufficient distance to overcome this clearance, and (c) to completely avoid creep and yielding in the expansion core. Again, FEA results came up short for meeting these requirements due to material constraints. Any design that would sufficiently expand a radial distance required to overcome assembly clearance (again, about 500 μm) would face catastrophic yielding, again according to FEA studies. Conversely, designs that would avoid yielding would not expand the necessary radial distance to overcome assembly clearance.

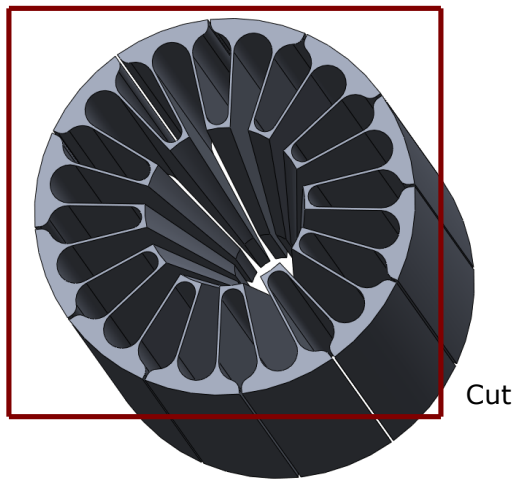


Figure 3-5. Example of one-piece tapered wedge driven expansion core (half section).

3.2.4. Concept 4: Multi-Component Platen System

The previous concept presented the opportunity to utilize traditional microlamination equipment, specifically the vacuum hot press (VHP), for bonding by converting uniaxial loading into axisymmetric pressure application. Therefore, the wedge design was carried over into a final multi-component concept whereby the expansion spring was split into a series of individual pressure delivery components, henceforth referred to as platens. The decoupled design separated the expansion core components and therefore eliminated the requirement to expand and contract elastically. This system also offered the use of common engineering materials, such as steel, copper, and graphite. The following sections discuss the details of this design, and Appendix A contains detail drawings of each component within the system.

3.3. Materials

The pressure delivery system was designed to prove the concept of cylindrical arrayed microchannel manufacturing. Therefore, materials were selected based on this premise. Copper was selected as the device material for its ease of fabrication, low-temperature bonding condition, and availability. Stainless steel 316 was selected for the platen material for its combination of relative ductility and good mechanical properties at copper's bonding temperature. Finally, graphite was selected for the wedge material for its very high compressive strength at high temperatures and natural lubricative properties.

Material properties at elevated temperatures can be difficult to find in the literature, especially at bonding temperatures, which are typically at 60-80% of the material's absolute melting temperature [26]. For the base material, pure copper, this indicates a bonding temperature of over 800° C. Relevant mechanical properties to the design of the pressure delivery system and device include elastic modulus, Poisson's ratio, and yield strength. The properties used for all calculations and FEA simulations for this thesis are displayed in Table 3-1. Some properties for copper had to be extrapolated due to lack of documentation. Appendix B shows these extrapolations. Further, room-temperature properties of graphite were used due to lack of documentation and the fact that 800° C is only a small fraction of the melting temperature of graphite.

Table 3-1. High-temperature (800° C) properties of materials.

	Elastic Modulus, E [GPa]	Poisson's Ratio, ν	Yield Strength, σ_y [MPa]
Copper	57.3 [27] [28][29](See Appendix B)	0.34 [30]	30.0 [31]
316SS	133.8 [32]	0.27 [32]	137.9 [32]
Graphite	35.0 [33]	0.19 [34]	480.0 [33]

3.4. Detailed Final Design

The final design for the pressure delivery system consists of six platens and two wedges, and is designed to bond a wrapped laminated structure of five full layers. The final design is shown in Figure 3-6, and Appendix A contains detailed drawings.

Further, the copper tube, henceforth referred to as the copper shell, had to be reinforced by a steel shell in order to avoid yielding. Each of these components will be discussed in detail in the following subsections.

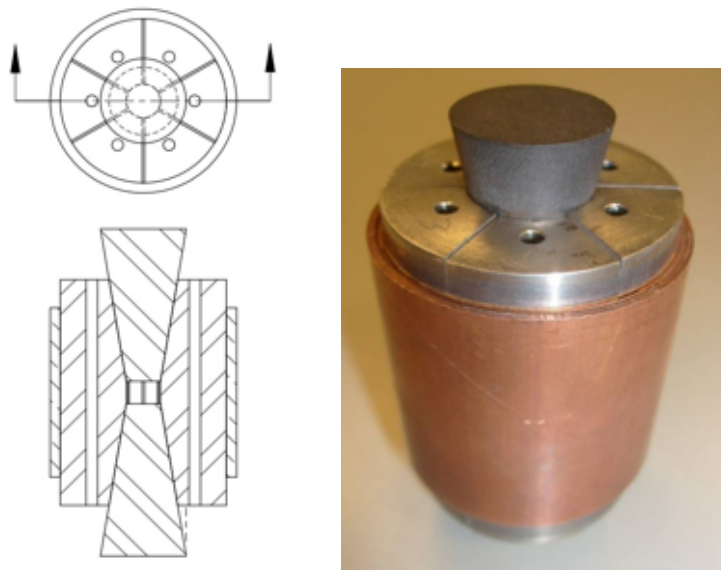


Figure 3-6. Final design for expandable core.

3.4.1. Platens

The six platens were designed with the aid of FEA to deliver reasonably evenly distributed pressure to the laminated device during bonding at elevated temperature. Tetrahedral mesh elements were used for each simulation, and mesh size was incrementally reduced until convergence was achieved, at which point mesh size was approximately 0.762 mm (0.030 in). The primary concern for the platens was designing them to deliver evenly distributed pressure to the laminated copper structures in both the tangential and radial directions. Best results were achieved by

adding a small through-hole in the platen face, which provides a small amount of flex and disallows pressure concentration in the center. The position and size of this hole was optimized using FEA. Contact stress analysis with the FEA software (COSMOS) was utilized to incrementally improve the distributions until results were satisfying (nominal pressure was 1,000 psi for these studies). Figure 3-7 shows the tangential contact stress results, and Figure 3-8 shows the axial contact results.

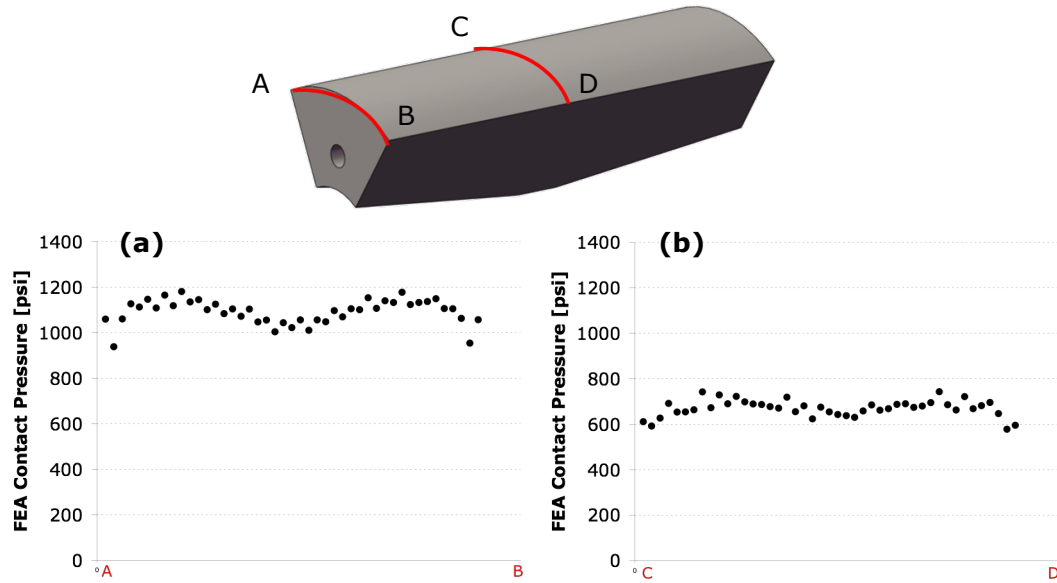


Figure 3-7. Tangential FEA contact results at (a) end of device, and (b) center of device.

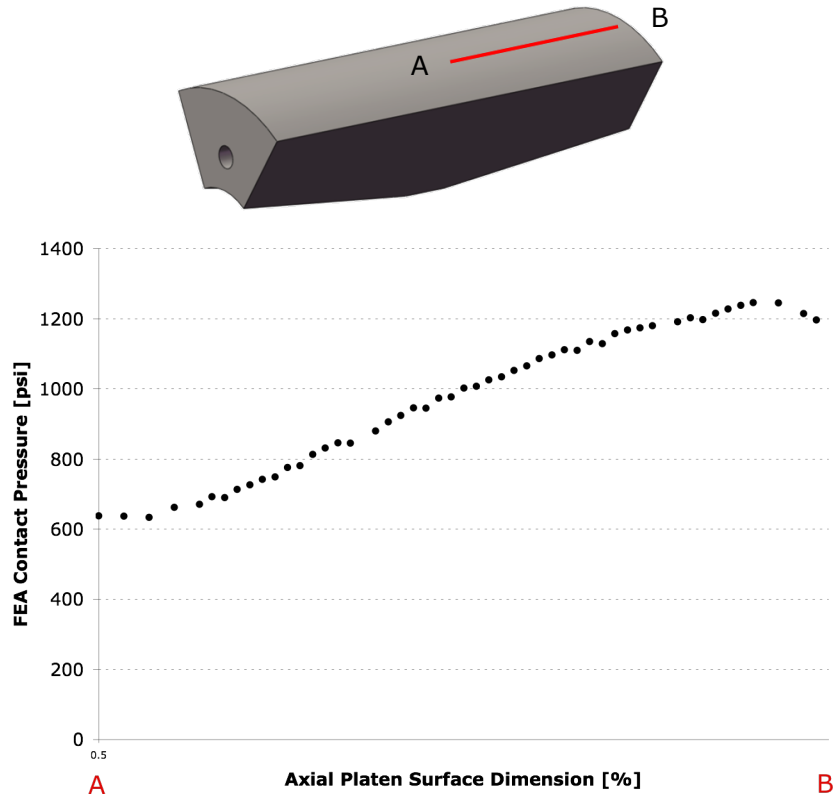


Figure 3-8. FEA contact stress results along axial direction, from center to edge of device.

As is evident from these FEA plots, there is reasonably even pressure distribution along the tangential direction of the surface of the platens, but poorer, sloping distribution along the axial direction. This slope is due to decreasing area of contact between the wedges and the platens from the edge axially inward. This is unavoidable with a wedge-driven expansion core. Figure 3-8 shows that pressure is roughly 67% of the nominal pressure at the center, and 125% at the edge. This rule of thumb was used for calculations that will be discussed in a later section.

3.4.2. Conical Wedges

The wedges were designed simply to make intimate contact with the platens when fully extended and constrained by the device being bonded. The same lathe taper cutting tool was used to turn the tapers on the platens and on the wedges. They have a 6:1 taper, implying that every unit of force delivered axially from the VHP rams would be converted to six units of force axisymmetrically delivered to the laminated device.

3.4.3. Shell Reinforcement

Due to the poor mechanical properties of copper at its diffusion bonding temperature (up to 800° C), it was necessary to investigate the robustness of the outer copper shell in order to avoid potential catastrophic yielding. Stress conditions of axisymmetric components are dependent only on geometry and not on mechanical strength [35]. Therefore, using the geometry of the outer copper shell, it is possible to calculate the maximum radial and tangential stresses in the copper cylinder using Eqs. 1 and 2 [35].

$$\sigma_r = \frac{a^2 p_i}{b^2 - a^2} \left(1 - \frac{b^2}{a^2} \right) \quad (1)$$

$$\sigma_\theta = \frac{a^2 p_i}{b^2 - a^2} \left(1 + \frac{b^2}{a^2} \right) \quad (2)$$

where a is the inner radius of the cylinder, b is the outer radius, and p_i is the internal pressure. These values can then be used to calculate the stress at which the cylinder will yield using the maximum distortion energy yield criterion (von Mises), or Eq. 3 [35].

$$\sigma_y = \sqrt{\sigma_r^2 - \sigma_r\sigma_\theta + \sigma_\theta^2} \quad (3)$$

Using an internal pressure of 11.25 MPa (1,632 psi), which was selected as the maximum bonding pressure and will be discussed in a later section, this leads to a yield stress of 187.7 MPa (27.2 ksi) for a copper cylinder of outer diameter 41.275 mm (1.625 in) and wall thickness of 1.2446 mm (0.049 in). Because this result is higher than the reported yield strength of copper at 800° C of 30.0 MPa (see Table 3-1), catastrophic yielding is expected. Therefore, it was necessary to reinforce the outer copper shell.

A common solution to reinforcing an internally pressurized tube is to create a composite wall by press fitting a surrounding, stronger tube [35]. Therefore, a 316 stainless steel cylinder (OD = 50.8 µm, ID machined to match copper) was press fit onto the outer copper shell for reinforcement. The interference pressure formed by the press fit was ignored analytically, because of the extended time it would be held at high temperatures during ramping for bonding, annealing all internal stresses. However, when the composite tube is internally pressurized by the expansion system,

a virtual interference is created by the potential over-expansion of the copper. This virtual interference pressure can be calculated using Eq. 4 [35]:

$$p = \frac{\delta}{\frac{b}{E_s} \left(\frac{c^2 + b^2}{c^2 - b^2} + \nu_s \right) + \frac{b}{E_c} \left(\frac{b^2 + a^2}{b^2 - a^2} - \nu_c \right)} \quad (4)$$

where δ is the radial interference, a is the innermost radius, and b is the nominal radius, calculated as the square root of the product of the two contact radii, and subscripts s and c denoting properties for steel and copper, respectively. Using the value calculated for the interference pressure, it is possible to calculate the yield conditions for the steel and copper shells separately. For the steel shell, Eqs. 1, 2, and 3 apply as they did for copper, using the interference pressure as internal pressure, p_i . Yield conditions for the copper must now take into consideration the interference pressure as an external pressure as well at the applied internal pressure from the previous section. The following cylinder stress equations apply [35]:

$$\sigma_r = \frac{a^2 p_i - b^2 p_o}{b^2 - a^2} - \frac{(p_i - p_o) a^2 b^2}{(b^2 - a^2) a^2} \quad (5)$$

$$\sigma_\theta = \frac{a^2 p_i - b^2 p_o}{b^2 - a^2} + \frac{(p_i - p_o) a^2 b^2}{(b^2 - a^2) r^2} \quad (6)$$

where a and b are the inner and outer radii, respectively, and p_i and p_o are the inner and outer applied pressures, respectively. For the tangential case, it is necessary to investigate the stresses at the innermost and outermost radii, as either could mathematically be found to be the maximum stress, depending on the inner to outer pressure ratio and ultimately hence the variable r in the second denominator. In the case at hand, the maximum value was found to be at the inner radius of the copper tube, where $r = a$. Once maximum radial and tangential stresses were calculated, yield conditions were calculated individually for the steel and copper cylinders using Eq. 3.

After reinforcement by the press-fit steel shell, the interference pressure between the two tubes was calculated to be 9.62 MPa, inducing a yield condition on the steel tube of 53.3 MPa (compared to a yield strength of 137.9 MPa; see Table 3-1). The yield condition on the copper tube was recalculated to be 24.4 MPa (compared to yield strength of 30.0 MPa). The design was robust¹ and yielding would not be a potential problem. It should also finally be noted that the copper and steel tubes, under the conditions described, would be permanently bonded. This was not considered a problem in the laboratory but could be a major economic inefficiency in future production.

¹ It should be noted that the low safety factor on the copper shell (1.23) is not of high concern, considering that, should the copper yield, the steel shell would be present to prevent failure of the setup.

3.4.4. Diffusion Barrier

This design calls for stainless steel platens to be in intimate contact and under high pressure with copper at elevated temperatures. Without the application of some barrier, these materials would diffuse and form an irreversible bond under these conditions. Therefore a diffusion barrier had to be applied to the platens.

Several papers have indicated that some specific thin films, namely titanium nitride [36], aluminum oxide [37], and silicon dioxide [38], serve as effective diffusion barriers for stainless steel and/or copper in integrated circuit (IC) and other micro-scale applications. Each of these was explored as a potential barrier for the pressure platens. TiN and SiO₂ were applied to stainless steel test coupons by sputtering for varying lengths of time (and therefore varying thicknesses), and Al₂O₃ was applied by atomic layer deposition (ALD) at varying thicknesses. The TiN coupons are shown in Figure 3-9. Each test coupon was alternatively stacked with copper coupons and subjected to common bonding conditions for copper diffusion bonding. None of the barriers succeeded in preventing bonding. This is likely due to the extreme conditions under which the samples were subjected. Few if any IC and other micro/nano-scale applications withstand such high temperatures in conjunction with high pressures. The high temperature especially serves to drive the atomic diffusivity exponentially higher, greatly extending diffusion distances as compared to traditional IC applications (thin films were on the order of tens to hundreds of nanometers).

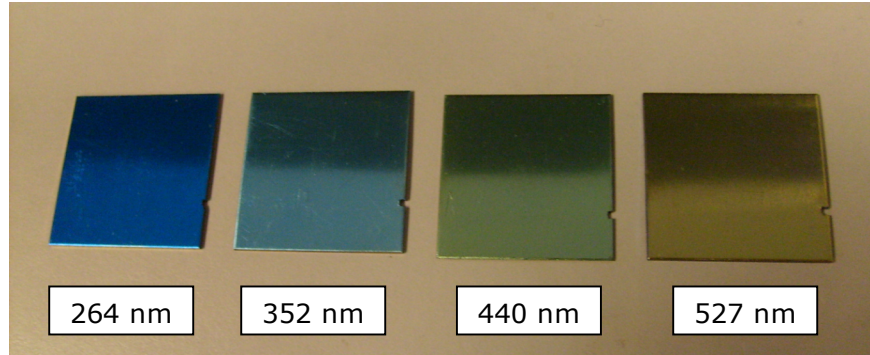


Figure 3-9. Various thicknesses of TiN reactive sputter films.

In traditional planar microlamination, interfaces that show the potential for undesired diffusion are commonly sprayed with the aerosol ceramic release agent, boron nitride (BN). This option was explored for the application at hand. However, BN is applied evenly to flat surfaces, but evenly distributed application to a round mandrel (the platen assembly) is much more complex.

To solve this problem, a platen assembly rotation fixture was designed and fabricated, shown in Figure 3-10 (full drawings in Appendix D). The platens were fixed to the pinned end caps and screwed onto the steel rod. This rod was then placed and affixed to a handheld drill. The assembly, save the platen surfaces, was taped off for protection, and the device was rotated by the drill in a closed environment while simultaneously spraying the aerosol BN from a distance of about 12 inches for about 15 seconds. This produced a barrier layer about $25 \mu\text{m}$ thick. This method proved successful after testing, and a view of the application environment and the results of this design and protocol can also be seen in Figure 3-10.

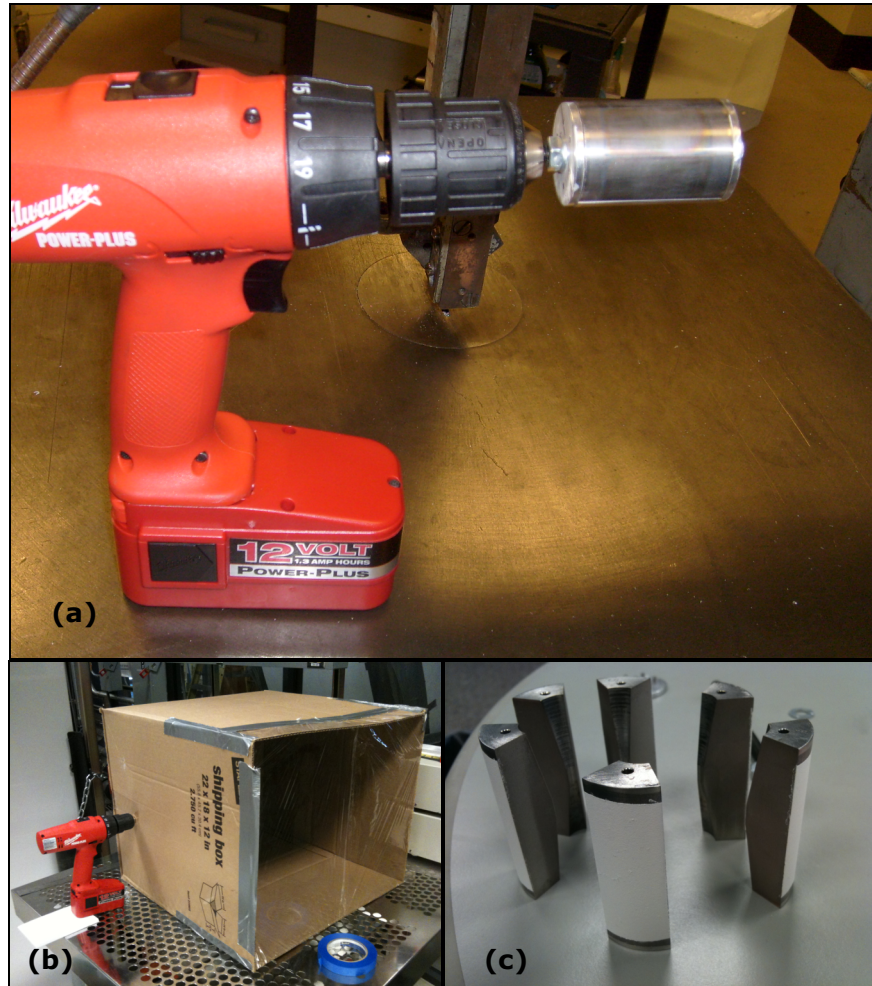


Figure 3-10. (a) Rotation fixture with platens attached, (b) BN application environment, and (c) results of BN application.

3.5. Channel Alignment Model

An alignment model for design of cylindrical arrayed microchannel devices was investigated whereby the lamina was cut as a single, long roll of shim with embedded features, rather than individual layers, and coiled to produce a layered structure. This offered the benefit of avoiding other more complicated methods of alignment, such as

registration pins that are common in planar geometry, and offered the potential to develop a geometric model for design of proper alignment. For design purposes, the layers were treated individually as if separate; however, they were cut as one long lamina. The model developed is based on calculating theoretical lengths of the “individual” layers, and finding a multiplier factor based on these lengths.

First, the length of the innermost layer of the device was calculated. Sheet metal bending theory was applied. Eq. [7] provides the total length of flat, straight stock required before bending:

$$L = \frac{\theta}{90} \left[kt + \frac{\pi}{2} r \right] \quad (7)$$

where θ = angle of bend in degrees, k = bend constant, t = thickness of stock, and r = inside radius of bend [39]. For a fully coiled shim, θ is 360° , so the equation for a single wrap was refined as Eq. [8]:

$$L = 4kt + 2\pi r \quad (8)$$

To calculate the required length of a multi-coiled geometry with n wraps, a summation was written as follows:

$$L = \sum_{j=1}^n (4kt + 2\pi r_j) \quad (9)$$

where r_j is the inside radius of wrap number j , starting from the innermost wrap. This was further simplified, however, by relating an equation for r_j :

$$r_j = r_1 + t(j - 1) \quad (10)$$

where r_1 is the inside radius of the innermost wrap. By substituting Eq. 10 into Eq. 8, a solution for the straight length of shim stock required for a single layer j was determined:

$$L_j = 4kt + 2\pi(r + t(j - 1)) \quad (11)$$

and the total length of shim needed for all n layers:

$$L = \sum_{j=1}^n [4kt + 2\pi(r + t(j - 1))] \quad (12)$$

which can further be solved and simplified as follows:

$$L = n[4kt + 2\pi r + (n - 1)\pi t] \quad (13)$$

One additional consideration must be taken, however. Eq. 13 assumes n wraps that are perfectly circular, but fails to consider the bending effects that occur at the overlap interface between wraps. This is shown in Figure 3-11. Furthermore, in order to eliminate stress concentrations at the overlap interface, a tangential gap needs to be considered, also as shown in Figure 3-11.

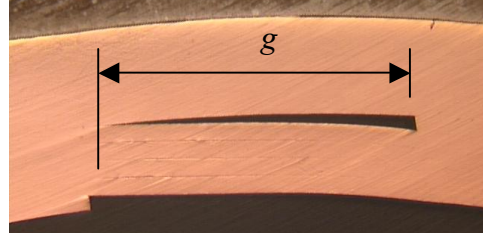


Figure 3-11. Micrograph showing the overlap interface as well as the gap.

Thus, Eq. 14 was developed as follows, adding in this gap, g :

$$L = n[4kt + 2\pi r + (n-1)\pi t] - g \quad (14)$$

where g is a prescribed gap that disallows stress concentrations at this interface. Though this gap is a complex curved shape, it was estimated to be linear for simplicity.

Finally, the multiplier, m_j , that can be used to scale the geometry of each subsequent layer can be calculated as a ratio of the length of layer j to the length of the first layer:

$$m_j = \frac{L_j}{L_1} = 1 + \frac{\pi t(j-1)}{2kt + \pi r} \quad (15)$$

3.6. Device Design Procedure

Using this model, a simple design protocol was developed. The design process can be broken up into the following steps:

- Calculate the length of the first layer of the device, L_1 , using Eq. 11.

- Design a microchannel array of the desired number of layers, n , temporarily using L_1 for each layer.
- Scale each layer only in the direction of wrap by the factor, m_j , from Eq. 15. Note that the positions of the channels should also be scaled by this factor, but not the sizes of channels (in order to maintain constant flow cross section).
- Place the layers end to end.

The concept of this design procedure is shown in Figure 3-12. Notice that on the left side of the figure the layers have already been scaled according to Eq. 15 (scale factors are generally quite small; for this study they were on the order of 1.01-1.06, depending on layer number).

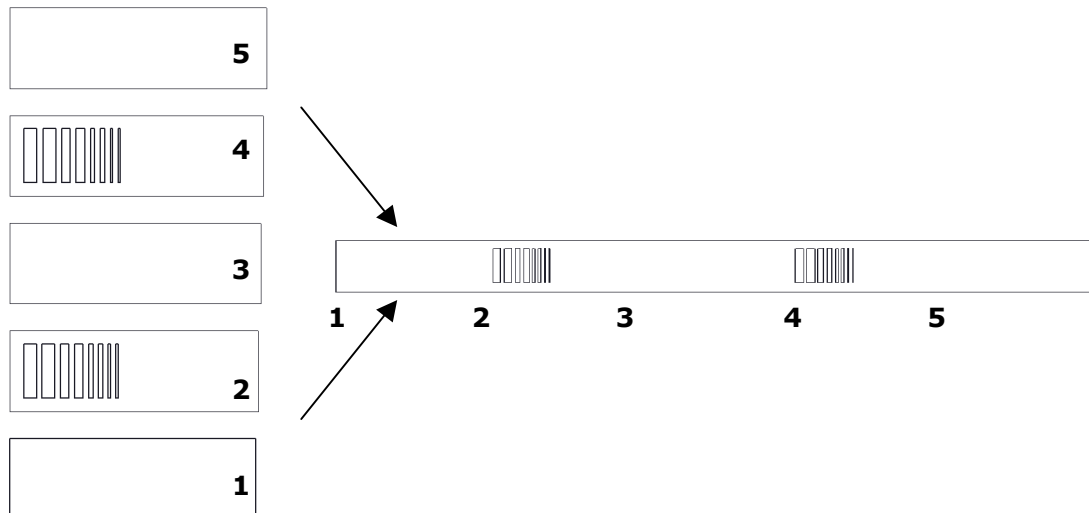


Figure 3-12. Design concept where layers are designed separately, scaled, and placed end-to-end.

4. EXPERIMENTAL INVESTIGATION

4.1. Overview

The primary objective of experimentation was to prove the capability of the pressure delivery system to apply adequate pressure for diffusion bonding. Secondarily, the alignment model in Section 3.5 was applied and analyzed. Initial experiments were performed to accurately test for bond integrity through void fraction measurement, to broadly test the alignment model, and to observe the characteristics of the channels produced. Secondly, tests were run with a narrowed scope to more precisely test the alignment model and to draw conclusions on its usefulness and effect on channel characteristics. The following subsections describe these experiments in details.

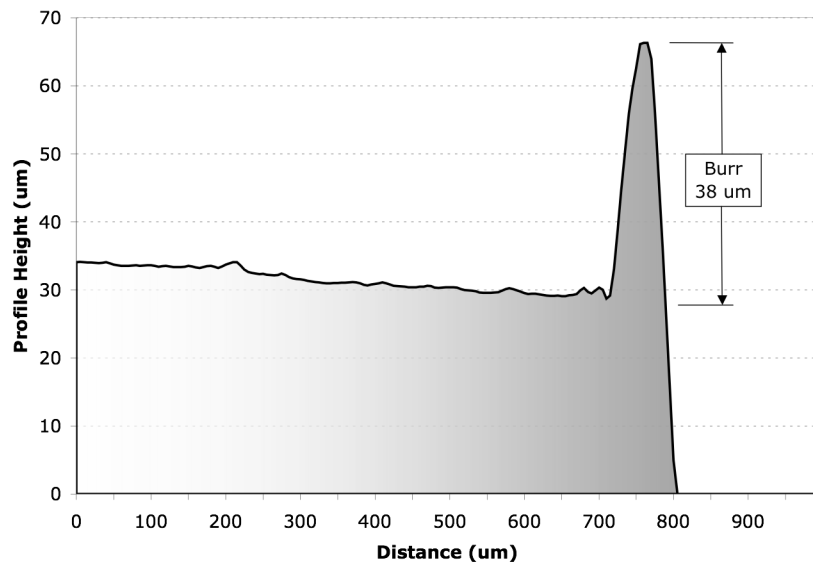
4.2. Lamina Fabrication and Preparation

All laminae were cut using an Electro Scientific Industries (ESI) Model 5330 UV Laser μ VIA Drill. The laser process “recipe” shown in Table 4-1 was followed to produce complete through-cuts in the 203- μ m thick copper shim stock.

Table 4-1. Laser mill parameters for 203- μm copper through-cut.

Parameter	Value
Velocity	60 mm/s
Rep Rate	30.0 kHz
Laser Power	5.000 W
Bite Size	2.00 μm
Pulse	16.667 μJ
Steps	4
Repetitions	45

The laser cutting process produced burrs adjacent to the cut line. Figure 4-1 shows the profile of this edge as measured by the Veeco Instruments DEKTAK³ surface profilometer. These burrs had to be removed in order to provide contact between adjacent surfaces during bonding.

**Figure 4-1. Channel edge profile after laser machining.**

The shims were hand-polished with an 800 grit silicon carbide micro-abrasive paper (average particle size 10 μm). After this procedure, the surface profile was re-measured to confirm the removal of burrs, and the results are shown in Figure 4-2. The de-burring process was repeated for every experiment after laser machining.

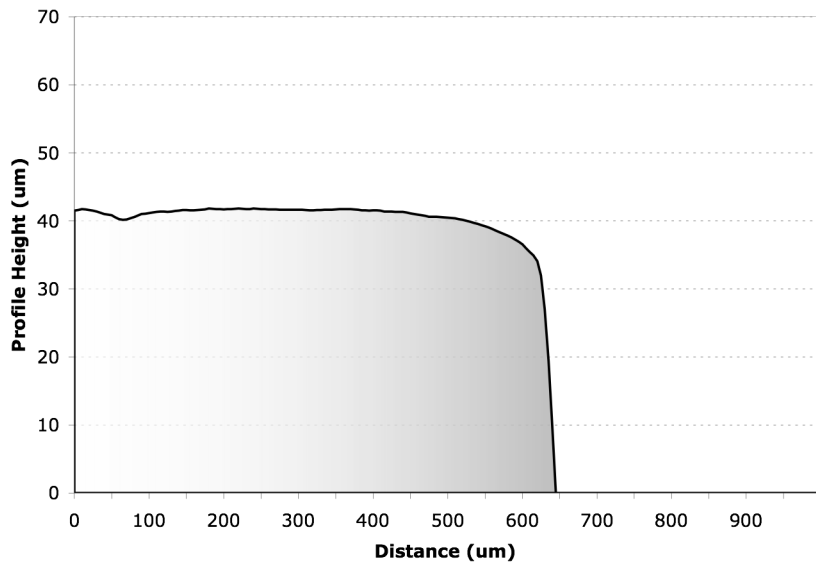


Figure 4-2. Channel edge profile after de-burring procedure.

4.3. Process Parameters

For these experiments, it was possible to control four of the five conditions identically to the traditional diffusion bonding process: surface, environment, time, temperature, but not pressure, which was discussed previously. Proper process parameters had to be selected for all five of these conditions.

4.3.1. Bonding Environment

First, bonding environment is simply controlled within the VHP. Vacuum was held throughout the bonding process, defined by pressure less than 10^{-4} torr. The hot press utilized was a Thermal Technology Model HP30-4560. The onboard cold cathode gage (CCG) was used to measure high vacuum pressure. All bonding runs were recorded as meeting the 10^{-4} torr target.

4.3.2. Surface Conditions

Surface conditions include both surface roughness as well as surface cleanliness. Roughness was measured on the DEKTAK³ surface profilometer. Scan lengths of 3 mm were taken. A general rule of thumb for diffusion bonding is that surface roughness of base materials, based on the arithmetic average of absolute values (R_a), of 0.4 μm or less is sufficient for successful bonding. Initial profilometer measurements showed a surface roughness of $0.23 \pm 0.08 \mu\text{m}$ for the copper shims and $0.21 \pm 0.11 \mu\text{m}$ for the inner surface of the copper shell, as delivered. However, after the de-burring process the shim roughness was measured to be $0.16 \pm 0.04 \mu\text{m}$, well within the desired range.

After de-burring and immediately before bonding, the laminae and shell were carefully cleaned. After a five-minute ultrasonic cleansing of these components (and all other components in the pressure delivery system) in a soapy solution (Citanox) to

remove surface contaminants, each part was rinsed with acetone for degreasing, methanol for oxide removal, and de-ionized water for final rinsing (AMD rinse). This was immediately followed by drying with high-pressure nitrogen.

4.3.3. Temperature

Diffusion bonding processes are effectively carried out at temperatures between 60% and 80% of the base material's absolute melting temperature [26]. For copper ($T_m = 1085^\circ \text{ C} = 1358 \text{ K}$), this rule of thumb yields a range for temperature selection of between 542° C and 813° C . Pluess [4] showed good void fraction results at 800° C , which is within the desired range. Therefore, 800° C was selected as a process temperature for all final experimentation, allowing comparison to other work.

Due to the bulky geometry of the pressure system and device itself, a very low temperature ramp of 5° C/min was chosen, disallowing significant temperature gradients. Further, for each bonding cycle temperature was monitored with two, independent type K thermocouples during ramp, dwell, and the beginning of cooling. The flexible thermocouples were placed directly in contact with the top and bottom surfaces on the expansion platens, and were routed to a data logger (Omega Multilogger model HH506RA) which took temperature readings every 10 seconds throughout the cycle. The thermocouples remained consistently equal within a few degrees for every run, and the results for each cycle are shown in Appendix E.

4.3.4. Pressure and Time

For the pressure delivery system, Figure 3-8 indicated that pressure magnitude would reduce by about 33% from the nominal pressure near the center of the platen assembly and increase by about 25% at the end of the device being bonded. Good bonding results have been shown in other work for pure copper at a pressure magnitude of 6.0 MPa (870 psi) [4]. Therefore, 9.0 MPa was selected as a nominal pressure for each experiment, resulting in approximately 6.0 MPa pressure in the center and 11.25 MPa near the axial end of the device, and allowing comparison at the center to the other work.

As was established in Section 3.1, however, creep is a potential concern as a failure mode during cylindrical bonding. The creep map for pure copper is shown in Figure 4-3. Creep is driven by time, temperature, and shear stress, which is high for an internally pressurized cylinder. In a cylinder, the maximum shear stress can be calculated by the following equation [35]:

$$\tau_{\max} = \frac{1}{2}(\sigma_{\theta} - \sigma_r) \quad (16)$$

where σ_{θ} and σ_r are the maximum tangential and radial stresses, respectively, calculated from Eqs. 1 and 2 above. The shear modulus of copper at bonding

temperature (800° C) is also required, and can be estimated from the known elastic modulus, E , and Poisson's ratio, ν , by the following equation [35]:

$$G = \frac{E}{2(1+\nu)} \quad (17)$$

The stresses calculated from Eqs. 3, 4, 5 and 6, with the maximum input pressure of 11.25 MPa, yield a maximum shear stress of 14.0 MPa (2,029 psi) and a shear modulus of 21.4 GPa (3,101 ksi). Therefore the normalized shear stress (shear stress divided by shear modulus) at 800° C is about 6.4e-4. This places the sample in the high-temperature power law creep regime of the creep map, indicating potential creep issues. However, following these calculation steps for traditional microlamination often places samples in the same creep regime. For example, Pluess [4] used a bonding pressure of 6.0 MPa for several tests on pure copper. Maximum shear stress for planar geometries can be calculated by the following equation:

$$\tau_{\max} = \frac{1}{2}(\sigma_1 - \sigma_2) \quad (18)$$

where σ_1 and σ_2 are the principal stresses in the x-y plane. This can be simplified by simply dividing the bonding pressure by two (as σ_2 is equal to zero). Therefore, the maximum shear stress for Pluess' work was about 3.0 MPa, and the normalized shear

stress for this work was about 1.2×10^{-4} , well within the high temperature creep regime for pure copper at 800°C , and very close to the conditions for the tests in this work.

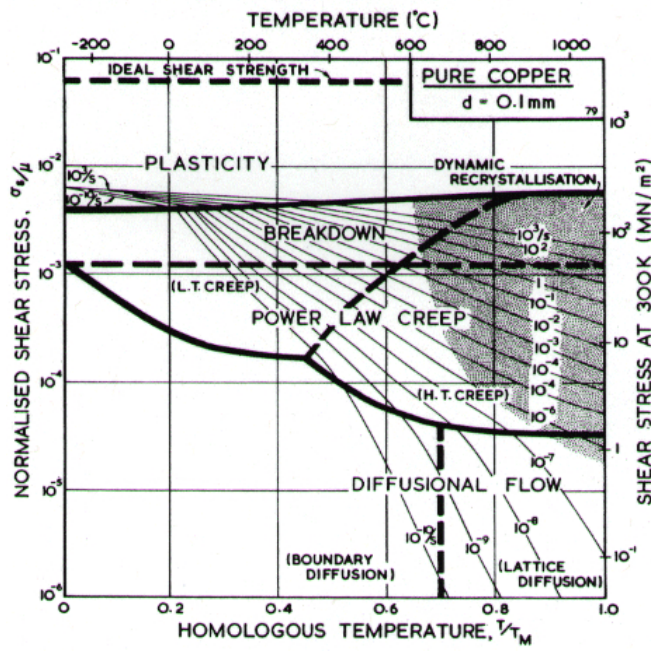


Figure 4-3. Creep map for pure copper [40].

The source for the creep map, Frost and Ashby [40], contains the following assessment:

The maps, then, should be used as the first phase of a design procedure only... Be cautious of attributing too much precision to the maps.

They are only as good as the equations and data used to construct them—and both are often poor.

Therefore, because previous work has been shown to produce good results within roughly the same region of the creep map as was calculated for this thesis, experiments were run under these conditions and creep was monitored. Because of

this potential for creep, however, bonding time was minimized and, finally, one hour was chosen for the final tests. It should also be noted that creep is common in many high-temperature, high-stress applications, such as microlamination. Therefore, though creep is undesirable, controlled and predictable creep strain can still produce effective microchannel arrays.

4.3.5. Metallographic Preparation

After each bonding cycle, careful metallography was carried out in order to take accurate data measurements of the measures of importance (to be discussed shortly). The bonded samples were first rough cut on a band saw in regions of non-interest. These cut sections were then mounted in a metallographic thermoset polymer (Buehler EpoThin Epoxy resin and hardener) for reinforcement during sectioning. The samples were then cross-sectioned on a Buehler Isomet 11-1180 low speed saw with a Buehler 4-inch diamond wafering blade. The cross sections were then rough-polished on a metallography wheel with silicon carbide abrasive papers of decreasing grit size (120, 240, 400, and 600) at 300 rpm, followed by fine polishing with diamond suspension (abrasive sizes of 6 μm and 1 μm , Buehler MetaDi polycrystalline diamond suspension) on a metallography cloth at 150 rpm.

Because copper is such a soft, ductile material, it was difficult to locate bond interfaces after only fine polishing. Therefore, the polished surfaces were lightly etched in a 30% nitric acid (HNO_3) aqueous solution for 20 seconds until the grain

structures were just revealed. This provided an unobstructed view of the bond lines under optical microscopy.

4.3.6. Creep of Steel Platens

As a precaution, the radial size of the steel platens was measured prior to and after each bonding cycle in order to monitor creep. No significant changes of dimension were found, resulting in no indication of creep in the stainless steel. The location of the measurement taken and the resulting graph over time can be seen in Appendix F.

4.4. Pressure Magnitude and Distribution Experiment

The first series of samples were for investigating the bond line integrity as a result of the pressure application system, measured by void fraction, as well as for gaining a broad set of data for the alignment model and channel heights.

4.4.1. Test Article Design

The test article for this series of bonding runs is illustrated in Figure 4-4. The sample was designed to be wound five full times (minus a small gap), creating a five-layer device. Channels were cut into the second and fourth layers, providing a means of testing the alignment model by measuring the tangential misalignment of the two sets of channels. The widths of the channels were designed to result in channel aspect ratios of 5:1, 10:1, 20:1, and 30:1, as each of these ratios have been proven possible in traditional microlamination tests. With two channels of each of these widths, eight

channels were produced on the channel layers, providing sixteen measurements of misalignment (the left and the right edges of each set of misaligned channels). Further, this design provided room to take a sample of channel-free region for void fraction analysis.

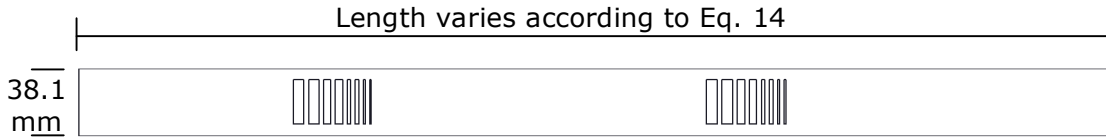


Figure 4-4. Test article design for first series of bonding runs.

4.4.2. Experimental Design

The only parameter that was varied throughout this test was the k-value in the alignment model. Four bonding runs were completed, with k-values of 0.0, 0.3, 0.7, and 1.0. Therefore, sixteen data points for each cylinder were created for both channel misalignment and for channel height (a measure of deformation). Eight measurements of void fraction were taken from the center and from the edge of the bonded samples, providing 32 data points for each for comparison.

4.4.3. Void Fraction Measurement

The one-dimensional fraction of void formation along the bonding interface after diffusion bonding is often called the void fraction, and is a good measure of the robustness of the bond formed. Void fraction, v_f , is calculated by the following simple equation:

$$v_f = \frac{\sum l_{void}}{l_0} \cdot 100\% \quad (19)$$

where l_{void} is the length of a single void in the direction of the bond line, and l_0 is the full length of the bond line sample.

The measurements were carried out on an optical microscope (Leica DMLM) after proper metallographic cross sectioning and polishing. Randomly located bond line samples were measured in 250- μm increments under 500X zoom. The microscope was equipped with a camera routed to a PC. Screen shots were captured for each sample segment. After all micrographs were captured, a marker was used on a transparent film to trace the void locations and sizes. The markings on these transparencies were then linearly measured and the void fraction calculated.

4.4.4. VHP Pressure Validation

Prior to each bonding cycle, the hydraulic ram in the VHP was calibrated with the use of an Omegadyne load cell (model LC304-5K). Data points were taken up to the load cell's maximum allowable sensitivity of 22.2 kN (5000 lb), and back down to zero load. These points were plotted and compared to the VHP's on-board load sensor (Omega brand). The results of the auxiliary load cell were always found to correlate linearly with the on-board sensor, and the results were used to calculate the required load for controlled pressure application during bonding. There was no observed

significant change in the regression over time. The calibration results are shown in Appendix G.

4.5. Channel Alignment Experiment

After the initial experiment was completed, the misalignment data was compiled and analyzed (and will be discussed in the results section). The k value from the alignment model was optimized based on the findings from the previous work, and a new test article was designed and fabricated. All process parameters remained the same as in the previous test.

4.5.1. Test Article Design

The test sample for this second run of tests was designed with four sets of channels of 5:1 and 10:1 aspect ratios (eliminating the higher-aspect-ratio-channels from the previous design). Also, rather than placing these channels in the second and fourth layers, fins were designed in these layers, with channels cut into the first, third, and fifth. The reasons for this will be discussed in the results section. Also, headers were designed into the fin layers, providing a means for metallography mount material (epoxy) to flow for more precise measurement. The final test article design is shown in Figure 4-5.

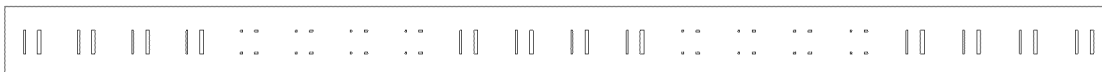


Figure 4-5. Test article for second run of bonding tests.

4.5.2. Experimental Design

Two bonding cycles were run for this final set of tests. This allowed two full sets of measurements for alignment (32 total data points) and for channel height (16 total data points). The k value was set the same for both cycles at 0.22 (reasoning to be discussed in results section).

5. RESULTS AND DISCUSSION

5.1. Pressure Delivery

The foremost objective of this thesis was to develop and demonstrate a method for delivering axisymmetric pressure for the purpose of arrayed microchannel applications within traditional diffusion bonding equipment. This section discusses the results of bonding quality as a result of this new pressure application method.

5.1.1. Void Fraction Results

The overall mean void fraction for the entirety of the tests run was 7.1%, with a 95% confidence interval of between 5.9% to 8.3%. There were noticeable differences between final void results at the center of the device versus at the edge, though not statistically significant ($p = 0.17$). Figure 5-1 shows the results of individual samples taken. Notice that for three of the four, in addition to the overall result, there was a higher mean void fraction at the center of the bonding sample than at the edge. This is consistent with expectations due to the FEA contact pressure results (see Figure 3-8).

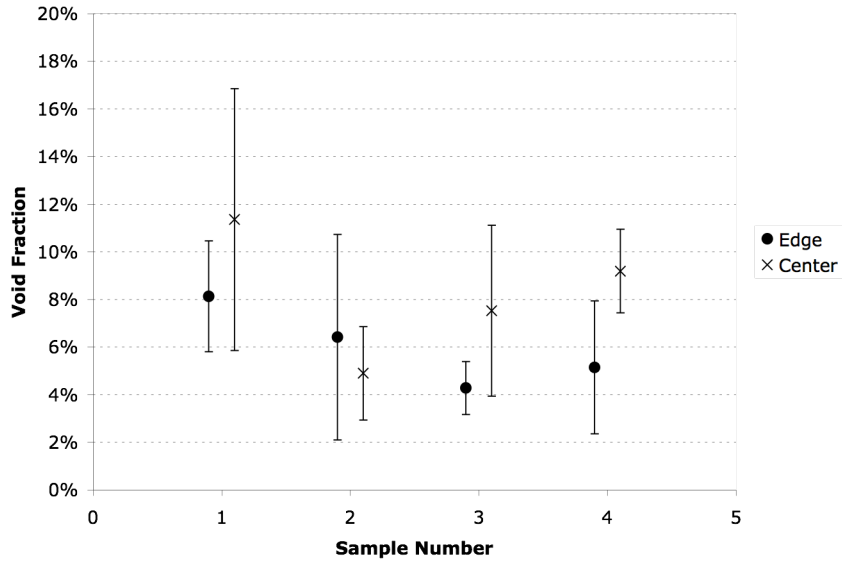


Figure 5-1. Void fraction results for each sample measured, shown at center and edge of sample.

Moreover, results were compared to the planar bonding results obtained by Pluess [4]. Pluess showed that under 6.0 MPa bonding pressure, at 800° C, for 60 minutes, mean void fraction results were 9.6%, with a 95% confidence interval of 7.9% to 11.3%. These results show no statistical difference from the results of the void fractions at the center of the samples in this work, where the pressure is about the same (6.0 MPa). Figure 5-2 shows the overall results for the edge and center of these samples, as well as the results obtained by Pluess.

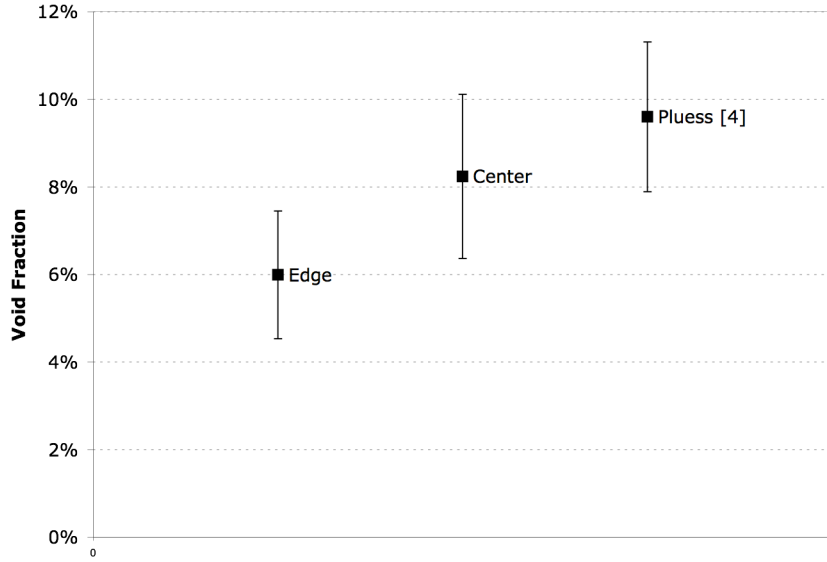


Figure 5-2. Overall void fraction results for edge and center locations, as well as results by Pluess [4].

These results support the hypothesis that the radial diffusion bonding method developed in this work is able to supply appropriate pressure to fabricate microchannel arrays.

5.2. Channel Characteristics

The model described in Section 3.5 was developed to provide a means to radially align channels within a cylindrical array. The model contains a bending factor, k , which must be empirically optimized in order to fabricate a functional device. The experiment described in Section 4.4 was carried out to test the adequacy of this alignment model, specifically by varying the values of k . It was found that this bending factor has direct effects on two main channel characteristics: alignment and

resulting channel height. These results are described in the following sections in detail.

5.2.1. Channel Alignment Results

The alignment model analytically predicts a linear relationship between the bending factor and the alignment (or misalignment) of the bonded channels within the cylindrical array. Figure 5-3 seems to confirm this linear relationship ($R^2 = 0.9644$).

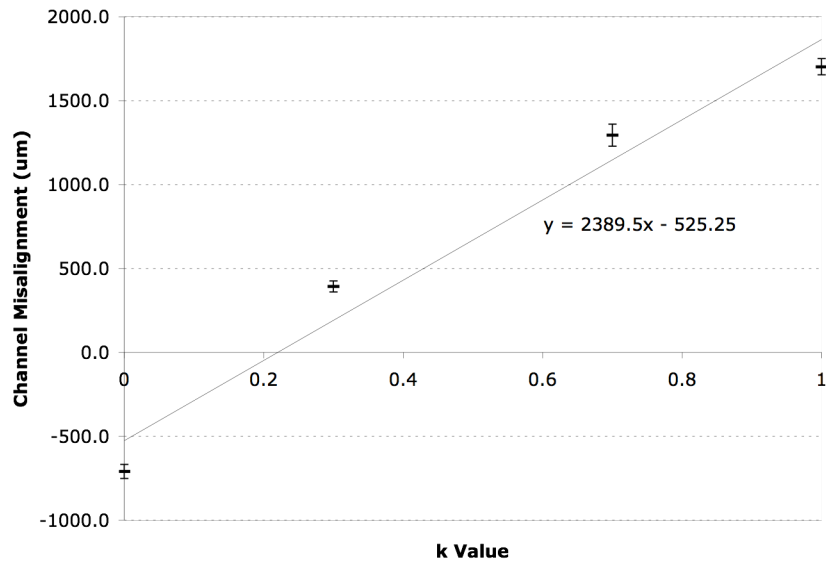


Figure 5-3. Channel misalignment vs k value, with 95% confidence intervals.

Once the fit line was determined, the deviation from the fit was calculated for each data point. The resulting average deviation from the fit line, in terms of absolute values of misalignment, was $181.9 \pm 19.1 \mu\text{m}$. This can be interpreted as that for an

optimized bending constant for any material (i.e., for the k value that would predict zero misalignment), one can expect alignment within about 200 μm , based on the measurement and design protocols used for these tests. 200- μm alignment is not necessarily adequate for fabrication of highly efficient microchannel arrayed devices; however, these results are somewhat skewed by channel and fin warpage due to the misalignment, which will be discussed shortly.

5.2.2. Effects of Misalignment

A strong correlation between channel misalignment and reduction in channel height was found. Figure 5-4 shows the effect of varying channel misalignment on the resulting channel height, including 95% confidence intervals.

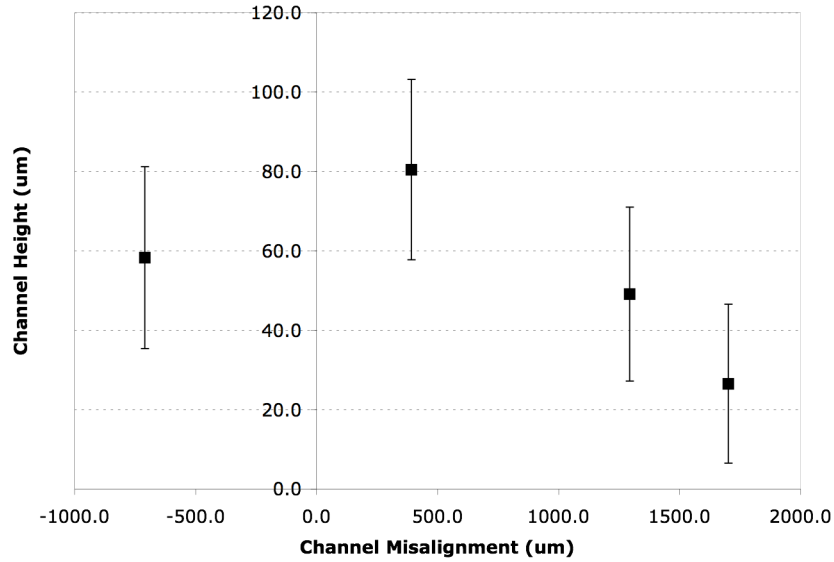


Figure 5-4. Resulting channel height vs channel misalignment, with 95% confidence intervals.

This figure shows that average channel heights for the test articles increase significantly as misalignment decreases toward perfect alignment. This can be explained by observing several micrographs of these channels. Figure 5-5 shows the resulting channel warpage from increasing misalignment.

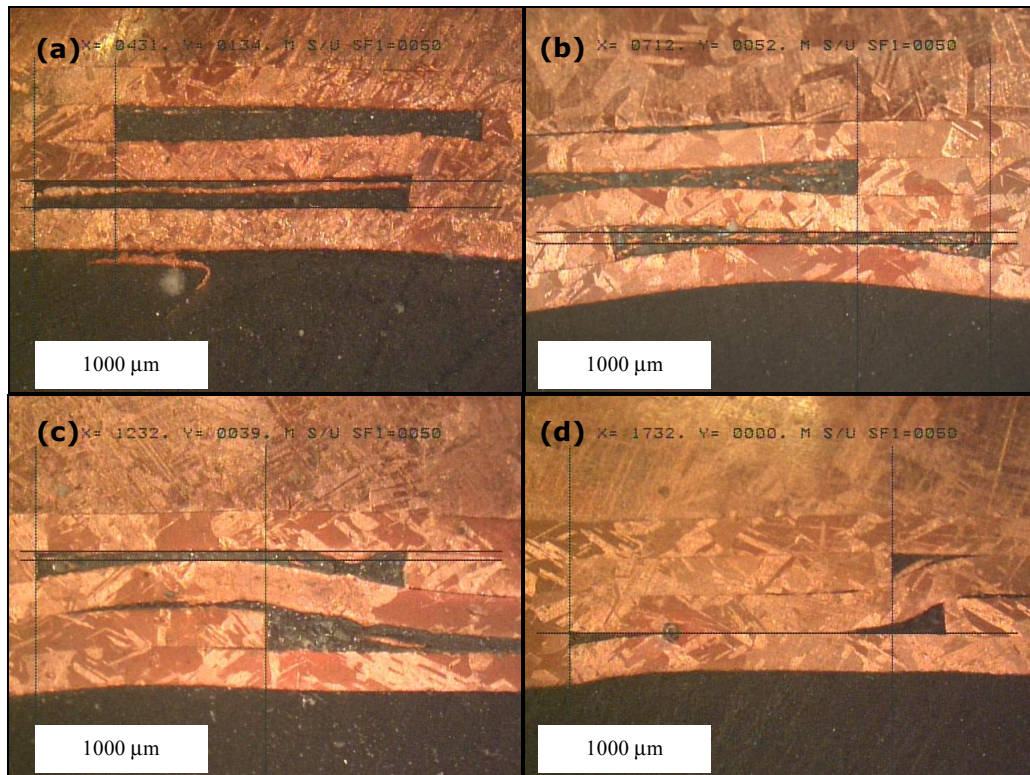


Figure 5-5. Channel warpage in order of increasing misalignment for 10:1 aspect ratio channels.

As can be seen from this figure, direct pressure application to severely misaligned channels acts to completely deform the array, producing a channel height of zero. This explains Figure 5-4, in that average channel heights are greatly reduced by the kinds of deformation mechanisms shown in these example micrographs. These

observations are directly in line with hypotheses presented by other microlamination studies [24].

5.2.3. Effects of Channel Aspect Ratio

There is also a strong relationship between the aspect ratios of the channels and the resulting channel heights. As would be expected, larger aspect ratios produce much more highly deformed channels, resulting in reduced channel heights. This is shown in Figure 5-6.

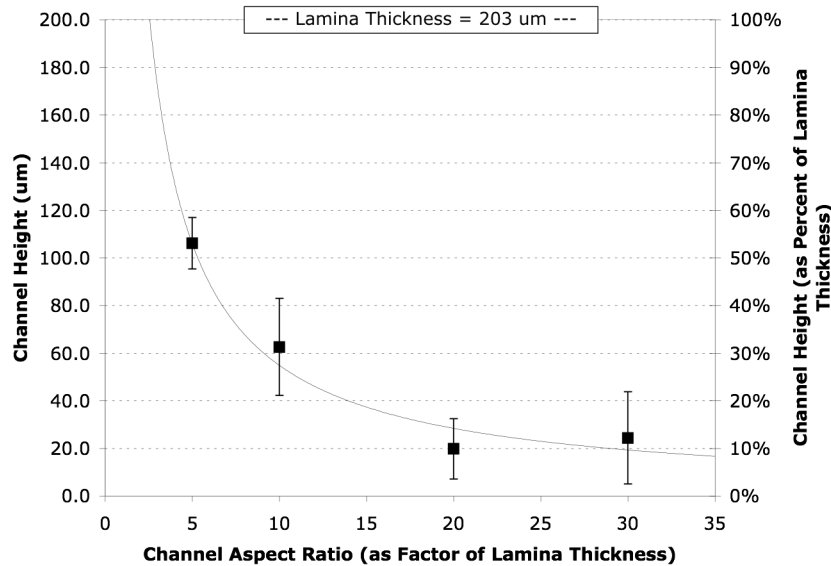


Figure 5-6. Channel height vs channel aspect ratio, with 95% confidence intervals.

However, the relationship shown in Figure 5-4 appears to decrease significantly as channel aspect ratio decreases. Figure 5-7 below shows the same data separated by channel aspect ratio. This figure shows drastic differences in average channel height

for higher aspect ratio channels (e.g., 20:1 and 30:1) as misalignment approaches zero, but for lower aspect ratio channels (e.g., 5:1) there is significantly less difference in channel height as misalignment increases.

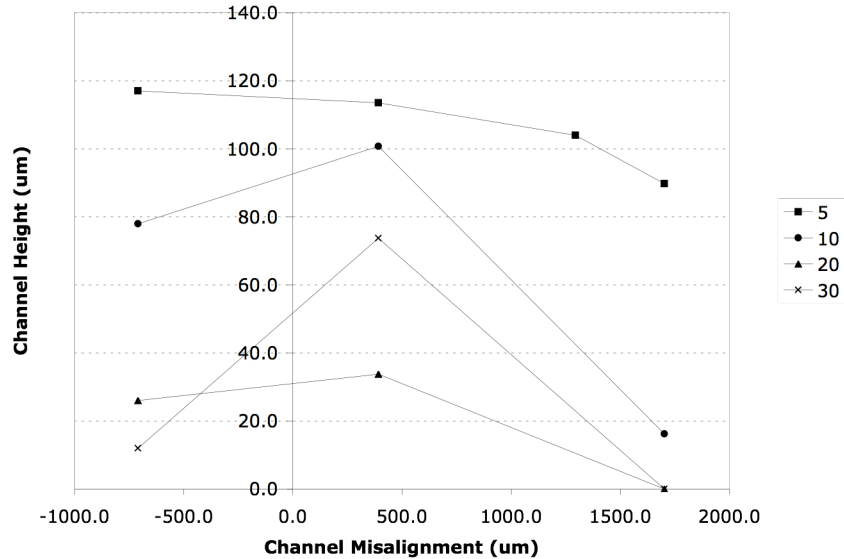


Figure 5-7. Channel misalignment vs channel height by aspect ratio.

Further, as indicated in the previous section regarding alignment, channel warpage also may play a reverse role in misalignment measurement. More specifically, highly warped channels undergo severe shape deformations, skewing the misalignment data. The standard deviations of the misalignment measurements against varying aspect ratios are shown in Figure 5-8. It is important to remember that higher aspect ratio channels are the more highly deformed. The graph illustrates much higher deviation for more highly deformed channels. This high deviation is having an effect on the precision of misalignment measurement for the purposes of optimizing k . Therefore,

if there was no significant channel warpage, misalignment data would be more precise and we would expect a better fit to the misalignment regression in Figure 5-3. This is a likely culprit for a portion of the 200- μm deviation discussed in the previous section.

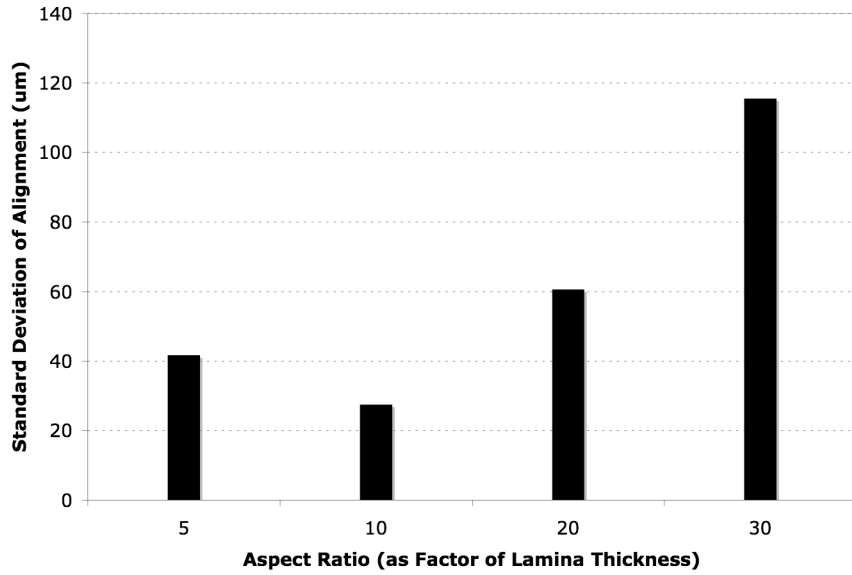


Figure 5-8. Standard deviation of channel misalignment by aspect ratio.

5.2.4. Defect Mode: Direct Pressure Transmission

A final observation resulting from this series of tests regards the effect of direct pressure transmission to fin structures. As seen in Figure 5-5(b), (c), and (d), pressure delivery transmitted directly to the first fin layer of the arrayed structure, especially when highly misaligned, has caused severe warping of the fin. This seems to be contributing to many of the poor channel characteristics described in this section. This

defect mode should be avoided by placing channel features on the first layer of a laminated structure, as will be discussed shortly.

5.2.5. Summary of Channel Characteristic Tests

The following conclusions were made based solely on this series of tests:

- Judging from this test, the alignment model appears to be adequate to produce channels within about 200 μm alignment precision using the protocol form this testing.
- Increasing channel misalignment significantly decreases resulting channel height.
- Increasing channel aspect ratio significantly decreases channel height for high aspect ratio channels (not necessarily so for lower aspect ratio channels).
- Increasing channel aspect ratio increases the standard deviation of misalignment, contributing to lower precision for use in the alignment model.
- Direct pressure transmission to a fin structure significantly decreases the resulting channel heights and likely contributes to all of these negative effects.

5.3. Application of Alignment Model

Referring again to Figure 5-3, the optimal k value for producing perfectly aligned channels is calculated to be 0.22. Again, however, it is important to understand the limits of this model as it was calculated, as was described in the previous section.

Two more bonding tests were run using this optimal k value of 0.22, with the expectation that alignment would fall within the $\pm 200 \mu\text{m}$ range previously described.

In short, however, the alignment tests did not confirm the correctness of the alignment model. Table 5-1 summarizes the results of the final alignment model tests. Because there are three channels, there are three separate misalignment values to calculate; this table lists the results organized by which layers from they were measured (e.g., “3-5” indicates the misalignment between the channels in layers three and five).

Table 5-1. Results of final alignment model confirmation tests.

Sample Number	Misalignment ± St. Dev. (μm)		
	1-3	3-5	1-5
1	937 ± 135	80 ± 148	1017 ± 281
	1559 ± 178	468 ± 125	2027 ± 302
Total	1248 ± 352	274 ± 239	1522 ± 588

As seen in this table, mean misalignment values are substantially higher than the expected 200-μm level. Interestingly, the results between layers one and three are statistically significantly lower than the results between layer three and five. This indicates that the k value in the alignment model is not linear, as assumed. Furthermore, the results for the first sample are significantly different from the results of the second sample, indicating that there is a level of imprecision in the design and/or fabrication process resulting in drastically different results for supposed equal inputs.

5.3.1. Geometry Measurement Precision

The first step in device design when applying the alignment model is to determine the length of the first layer, as described in Section 3.6. This initial calculation requires the input of two manually measured values: copper shell inside radius and lamina thickness. For this thesis, the inside diameter was measured with a digital caliper ten times, with an average taken as the final result, and the laminae with a micrometer averaged over ten measurements. It is theorized that the poor results seen in Table 5-1 are a results of imprecise measurements.

A brief sensitivity analysis of the effect of mismeasurement of the inside diameter of the copper shell versus the resulting calculated length of the first layer was conducted. The following figure plots this relationship.

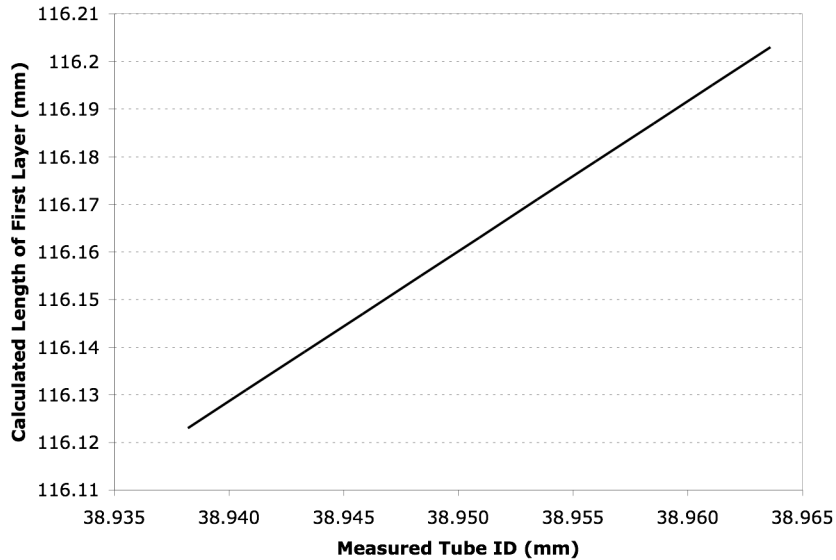


Figure 5-9. Sensitiviy plot of the effect of mismeasurement of sheel ID.

This plot shows that for very small variations in the measurement of the inside diameter of the copper shell (this plot shows a range of only 25 μm), there is a significant change in the calculation for the length of the first layer of the device (80 μm in this case). When considering that this is only that first layer of several, this error will compound quickly as the subsequent layer scale factors are calculated. This fully explains the major disagreement between the results of samples one and two in Table 5-1. Very precise and accurate measurement would be required for the alignment model to work effectively.

5.3.2. Non-Linearity of k Value in Model

Table 5-1 also indicated very different misalignment results among different sets of layers. Therefore another cross-sectioning and metallographic preparation was made at the header region of one of the samples in order to see features in all five layers. The resulting micrograph is shown in Figure 5-10.

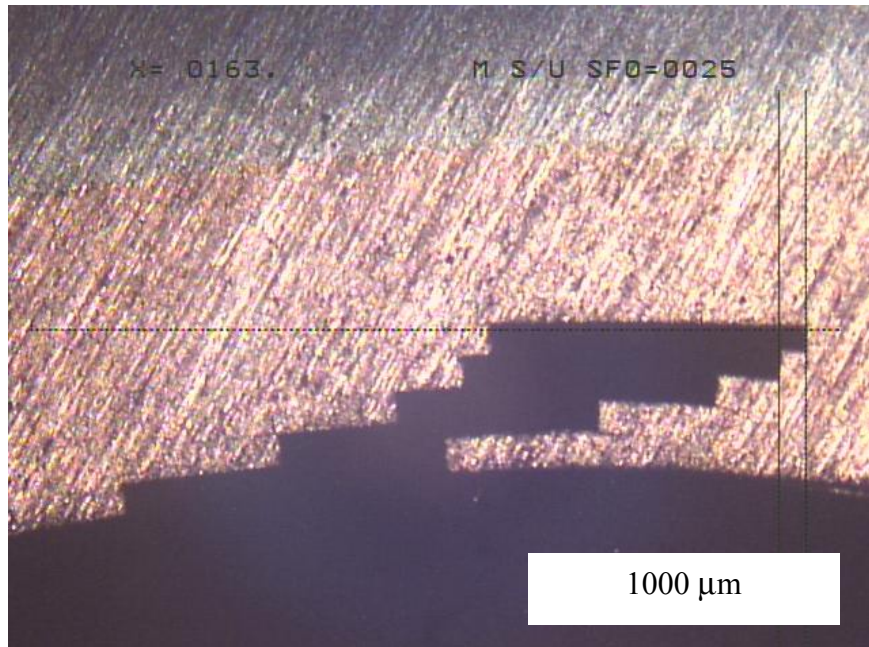


Figure 5-10. Micrograph of header region in final alignment test.

The alignment model would predict that the misalignment between adjacent channels would be equal throughout; that the misalignment would be linearly related to the layer number. This doesn't appear to be the case in Figure 5-10. Therefore, for this one sample the misalignment values were measured and plotted (see Figure 5-11).

The results are surprising, as the relationship is strongly second-degree polynomial ($R^2 = 0.9999$).

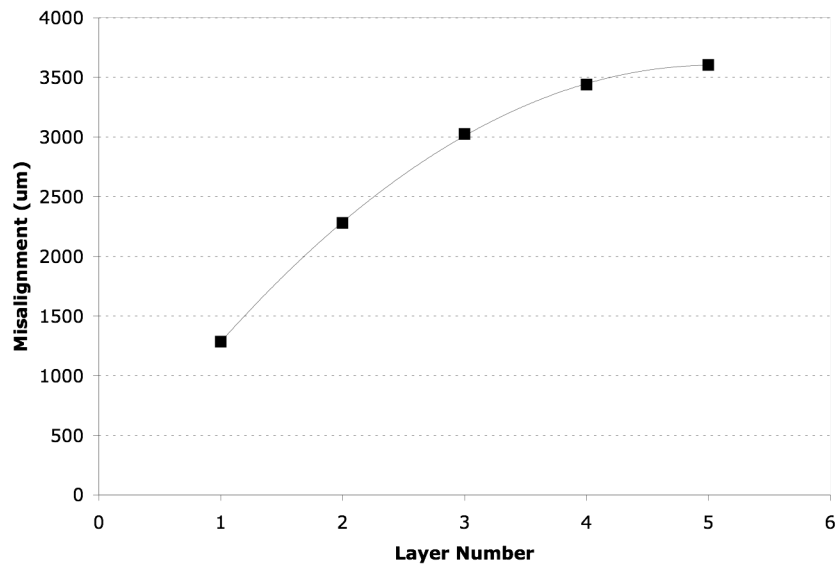


Figure 5-11. Misalignment of header region.

This relationship indicates not only that k is not linear, but that it is predictably second-order polynomial. Therefore, though outside the scope of this thesis, it is entirely feasible to remodel the alignment mathematics to provide a very predictable means of aligning channels in a cylindrical array (again, provided very precise measurement of input parameters).

6. CONCLUSIONS

This thesis documents the effort to develop and test an architecture for enabling the fabrication of cylindrical microchannel arrayed devices. The system developed involves the use of an expandable pressure delivery system that can be used within traditional VHP equipment. This study has proven that the concept of cylindrical microchannel arrays is entirely feasible, and has made a number of important findings.

6.1. Key Findings

- The pressure delivery system is capable of distributing pressure to cylindrical laminated structures for diffusion bonding with resulting bond lines statistically indeterminate from traditional planar geometry bonding.
- The alignment model was shown to be insufficient in its current state; however, post-bonding tests indicate that the model could be reworked to provide very close alignment.
- Direct pressure application to fin structures in an array results in drastically reduced channel heights.
- Contrary to previous claims, maldistribution of pressure, when carefully controlled, can still produce quality solid-state diffusion bonds.

6.2. Recommendations for Future Work

This work is the first known attempt to develop a method of diffusion bonding radially for MPT applications, and has shown this concept to be feasible. There are several directions future studies could explore. The first broad topic that should be more deeply explored is device geometry. Future work should look at the effects of geometrical parameters on bond quality, such as varying the device diameter and/or

device length. This could be difficult and/or expensive, however, because each new device size would require fabrication of a different expansion core.

Another topic that should be investigated is material use, both in the device and in the expansion core. For the device, a material less susceptible to creep than pure copper should be looked at, and for the pressure delivery system it would seem that the use of ceramic materials could offer a more elegant solution. Some ceramics would not require the use of a diffusion barrier and would withstand the high-temperature compressive stresses with a much higher factor of safety.

Furthermore, axial pressure distribution from the platens to the workpiece could also be improved through more complex design alterations in the platens. For example, axial slots could feasibly be cut into the ends of the platens, reducing pressure magnitude at the ends and more evenly distributing pressure axially.

Moreover, alignment of microchannels should be completely re-investigated. First, the alignment model should be reworked and adjusted for appropriate non-linearity of the k value, and this should be done in conjunction with more precise measurement of geometry prior to bonding (perhaps by CMM). Secondly, for devices with more than a few layers, pre-wrapped lamina lengths would get very long: likely too long for any laser mill. Therefore it should be looked at to cut each layer individually, as is done in planar microlamination, and to align the cylindrical laminae in a new, novel way. For

all of this future work, misalignment of 5-50 μm should be targeted, as this is common for traditional microlamination [41].

There are obviously many opportunities for future work in this topic. With this thesis and some further studies, though, it is evident that functional cylindrical MPT devices are feasible and well within the reach of development.

7. REFERENCES

- [1] B.K. Paul and R.B. Peterson, "Microlamination for microtechnology-based energy, chemical, and biological systems," *ASME International Mechanical Engineering Congress and Exposition, AES*, Nashville, Tennessee: 1999, pp. 45-52.
- [2] S. Kandlikar and W. Grande, "Evolution of microchannel flow passages—thermohydraulic performance and fabrication technology," *Heat Transfer Engineering*, vol. 24, 2003, pp. 3-17.
- [3] S. Bose, "An internal convective heating technique for diffusion bonding highly parallel microchannel architectures," Thesis, Oregon State University, 2009.
- [4] C. Pluess, "Application of Controlled Thermal Expansion in Diffusion Bonding for the High-Volume Microlamination of MECS Devices," Thesis, Oregon State University, 2004.
- [5] W.M. Rohsenow, J.P. Hartnett, and E.N. Ganić, Eds., *Handbook of Heat Transfer Applications*, New York: McGraw-Hill, 1985.
- [6] R. Tew, M. Ibrahim, D. Danila, T. Simon, S. Mantell, L. Sun, D. Gedeon, K. Kelly, J. McLean, G. Wood, and S. Qiu, *A Microfabricated Involute-Foil Regenerator for Stirling Engines*, St. Louis, Missouri: National Aeronautics and Space Administration, 2007.
- [7] E. Visca, B. Riccardi, A. Orsini, and C. Testani, "Manufacturing and testing of monoblock tungsten small-scale mock-ups," *Fusion Engineering and Design*, vol. 56, 2001, pp. 343-347.
- [8] E. Visca, S. Libera, A. Mancini, G. Mazzone, A. Pizzuto, and C. Testani, "Pre-brazed casting and hot radial pressing: A reliable process for the manufacturing of CFC and W monoblock mock-ups," *Fusion Engineering and Design*, vol. 82, 2007, pp. 1651-1656.
- [9] E. Visca, S. Libera, A. Mancini, G. Mazzone, A. Pizzuto, and C. Testani, "Hot radial pressing: An alternative technique for the manufacturing of plasma-facing components," *Fusion Engineering and Design*, vol. 75, 2005, pp. 485-489.

- [10] B.K. Paul, R.B. Peterson, and W. Wattanutchariya, "The effect of shape variation in microlamination on the performance of high-aspect-ratio, metal microchannel arrays," *Microreaction Technology: 3rd International Conference on Microreaction Technology*, W. Ehrfeld, Ed., Berlin: Springer-Verlag, 2000.
- [11] R.I. Batista, "Diffusion bonding process," U.S. Patent 3703032, November 1972.
- [12] C.E. Bowling and G.B. Meginnis, "Bonding," U.S. Patent 3762032, October 1973.
- [13] E.S. Bunn, "Method of bonding," U.S. Patent 3481024, December 1969.
- [14] T. Kawasaki, I. Takada, and H. Ohtsubo, "Method of manufacturing bimetallic tubes," U.S. Patent 4533806, August 6, 1985.
- [15] J.K. Eckert, J.M. Farina, J.P. Gadda, J.C. Kelly, and J.G. Thomas, "Multilayer composite tubular structure and method of making," U.S. Patent 5858556, January 12, 1999.
- [16] K.T. Jackson and L. Porter, "Tubular products," U.S. Patent 4028785, June 14, 1977.
- [17] T.C. Quinby, "High-temperature, high-pressure bonding of nested tubular metallic components," U.S. Patent 4231507, November 4, 1980.
- [18] S.J. Sharp, M.F. Ashby, and N.A. Fleck, "Material response under static and sliding indentation loads," *Acta Metallurgica et Materialia*, vol. 41, Mar. 1993, pp. 685-692.
- [19] N. Orhan, M. Aksoy, and M. Eroglu, "A new model for diffusion bonding and its application to duplex alloys," *Materials Science and Engineering A*, vol. 271, Nov. 1999, pp. 458-468.
- [20] M.F. Islam and N. Ridley, "Isostatic Diffusion Bonding of a Microduplex Stainless Steel," *Scripta Materialia*, vol. 38, Mar. 1998, pp. 1187-1193.
- [21] W. Wattanutchariya and B.K. Paul, "Effect of Fixture Compliance on Thermally Enhanced Edge Registration in Microlamination," *Journal of Manufacturing Science and Engineering*, vol. 126, 2004, p. 845.

- [22] H. Hasan, "Development of microchannel arrays in aluminides," Dissertation, Oregon State University, 2006.
- [23] W. Wattanutchariya and B.K. Paul, "Bonding fixture tolerances for high-volume metal microlamination based on fin buckling and laminae misalignment behavior," *Precision Engineering*, vol. 28, Apr. 2004, pp. 117-128.
- [24] C.H. Tseng, "Sources of flow maldistribution in microreactor-assisted synthesis of ceria nanoparticles," Dissertation, Oregon State University, 2008.
- [25] E. Oberg, F.D. Jones, H.L. Horton, and H.H. Ryffel, "Allowances and Tolerances for Fits," *Machinery's Handbook*, C.J. McCauley, R.M. Heald, and M.I. Hussain, Eds., New York, NY: Industrial Press, 2004, pp. 645-691.
- [26] W.H. Kearns, "Diffusion Welding and Brazing: Fundamentals of the Processes," *Welding Handbook: Resistance and Solid-State Welding and Other Joining Processes*, Miami, FL: American Welding Society, 1980, pp. 312-335.
- [27] EngineeringToolbox.com, "Young Modulus of Elasticity for Metals and Alloys," *The Engineering Toolbox*, 2005.
- [28] H.J. Stokes, "Apparatus for the Measurement of Young's Modulus, Between 200 and 700°C by transverse Vibration in Vacuum," *Journal of Scientific Instruments*, vol. 37, Apr. 1960, pp. 117-120.
- [29] C.H. Thornton, S. Harper, and J.E. Bowers, *A Critical Survey of Available High Temperature Mechanical Property Data for Copper and Copper Alloys*, New York, NY: International Copper Research Association, Inc., 1983.
- [30] R.A. Wilkins, "The Coppers," *Copper and copper base alloys: The physical and mechanical properties of copper and its commercial alloys in wrought form*, New York and London: McGraw-Hill Book Company, Inc, 1943, pp. 1-26.
- [31] J.R. Davis, "Properties of Wrought Copper and Copper Alloys," *Copper and Copper Alloys*, ASM International, 2001, pp. 453-528.
- [32] W.F. Brown, H. Mindlin, and C.Y. Ho, Eds., "Austenitic Stainless Steels (FeA-1300)," *Aerospace Structural Metals Handbook*, West Lafayette, IN:

CINDAS/USAF CRDA Handbooks Operation, Purdue University, 1997, pp. 1301:1-1314:32.

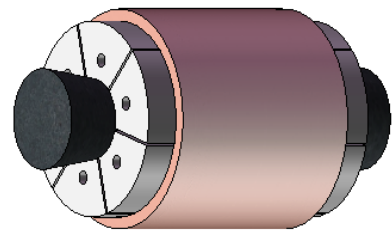
- [33] H.O. Pierson, *Handbook of carbon, graphite, diamond, and fullerenes*, William Andrew, 1993.
- [34] T. Dumitrica, *Trends in Computational Nanomechanics*, Springer, 2009.
- [35] A.C. Ugural and S.K. Fenster, “Axisymmetrically Loaded Members,” *Advanced strength and applied elasticity*, New York: Elsevier, 1987, pp. 261-299.
- [36] E. Garwin, E. Hoyt, and A. Nyairesh, “TiN high temperature diffusion barrier for copper-gasketed stainless-steel flanges,” *Journal of Vacuum Science and Technology (Submitted)*, Mar. 1986.
- [37] X. Nie, E.I. Meletis, J.C. Jiang, A. Leyland, A.L. Yerokhin, and A. Matthews, “Abrasive wear/corrosion properties and TEM analysis of Al₂O₃ coatings fabricated using plasma electrolysis,” *Surface and Coatings Technology*, vol. 149, Jan. 2002, pp. 245-251.
- [38] F.B. Ellis and J. Houghton, “Chemical vapor deposition of silicon dioxide barrier layers for conductivity enhancement of tin oxide films,” *Journal of Materials Research*, vol. 4, Aug. 1989, pp. 863-872.
- [39] E. Oberg, F.D. Jones, H.L. Horton, and H.H. Ryffel, “Punches, Dies, and Press Work,” *Machinery's Handbook*, C.J. McCauley, R.M. Heald, and M.I. Hussain, Eds., New York, NY: Industrial Press, 2004, pp. 1329-1348.
- [40] H.J. Frost and M.F. Ashby, *Deformation-Mechanism Maps: The Plasticity and Creep of Metals and Ceramics*, Pergamon Pr, 1982.
- [41] B.K. Paul and J.S. Thomas, “Thermally Enhanced Edge Registration for Aligning Diffusion-Bonded Laminae,” *Journal of Manufacturing Processes*, vol. 5, 2003, pp. 185-193.

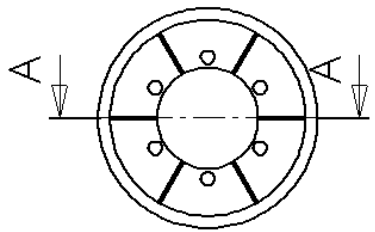
8. APPENDICES

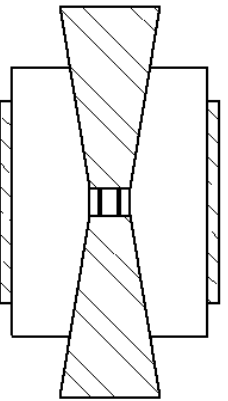
- A. PRESSURE DELIVERY SYSTEM DRAWINGS
- B. HIGH-TEMPERATURE COPPER ELASTIC MODULUS
- C. DESIGN DETAILS PRIOR TO BONDING
- D. ROTATION FIXTURE DRAWINGS
- E. BONDING CYCLE TEMPERATURE PROFILES
- F. PLATEN CREEP MEASUREMENTS
- G. VHP PRESSURE MAGNITUDE CALIBRATION
- H. VOID FRACTION DETAILED RESULTS
- I. MISALIGNMENT DETAILED RESULTS

A. PRESSURE DELIVERY SYSTEM DRAWINGS

ITEM NO.	PART NUMBER	DESCRIPTION	QTY.
1	16core2-solid (shims full)	Core Platen	6
2		Copper Shims (No Fab Req'd)	1
3	graphite_wedge	End Wedge	2



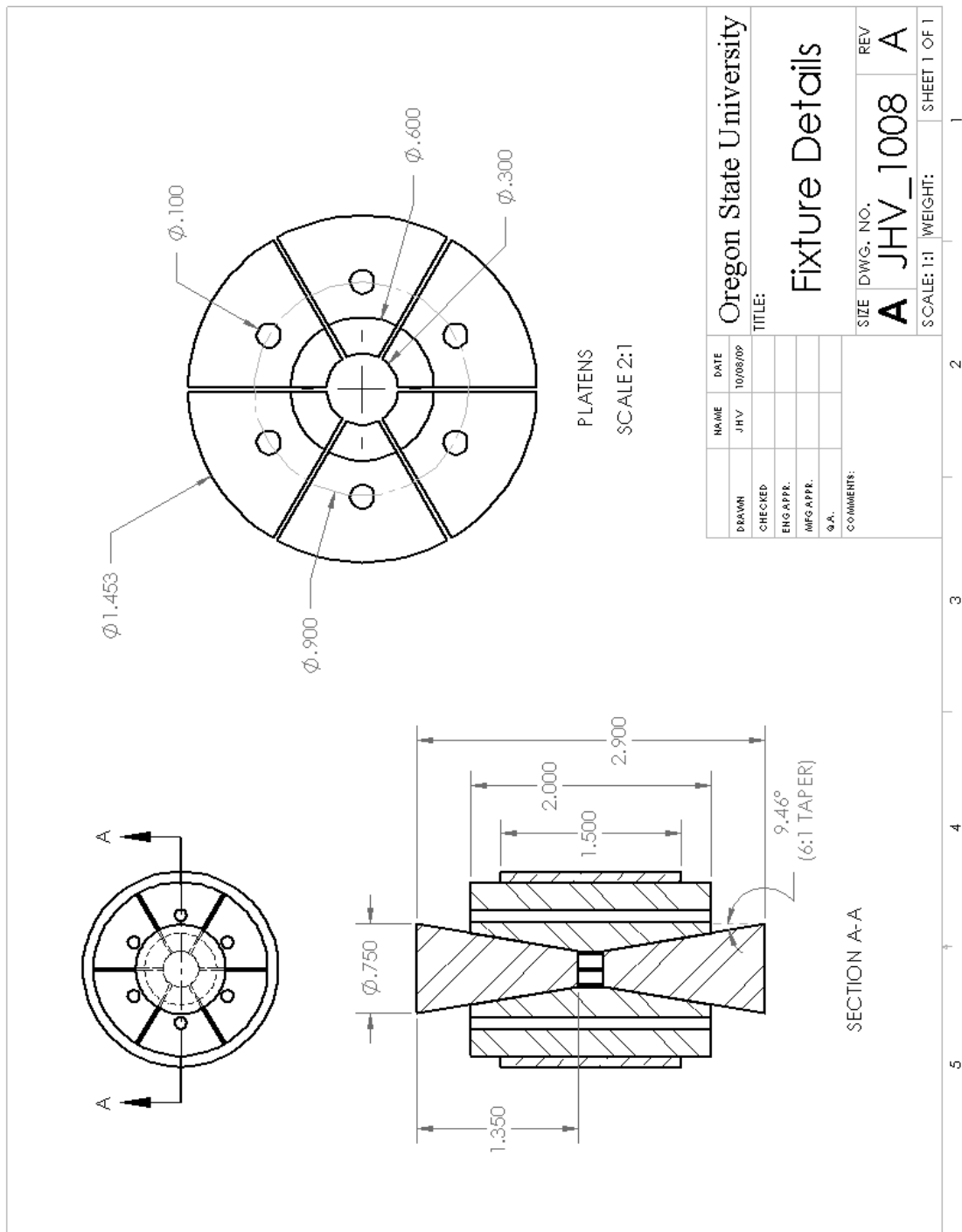




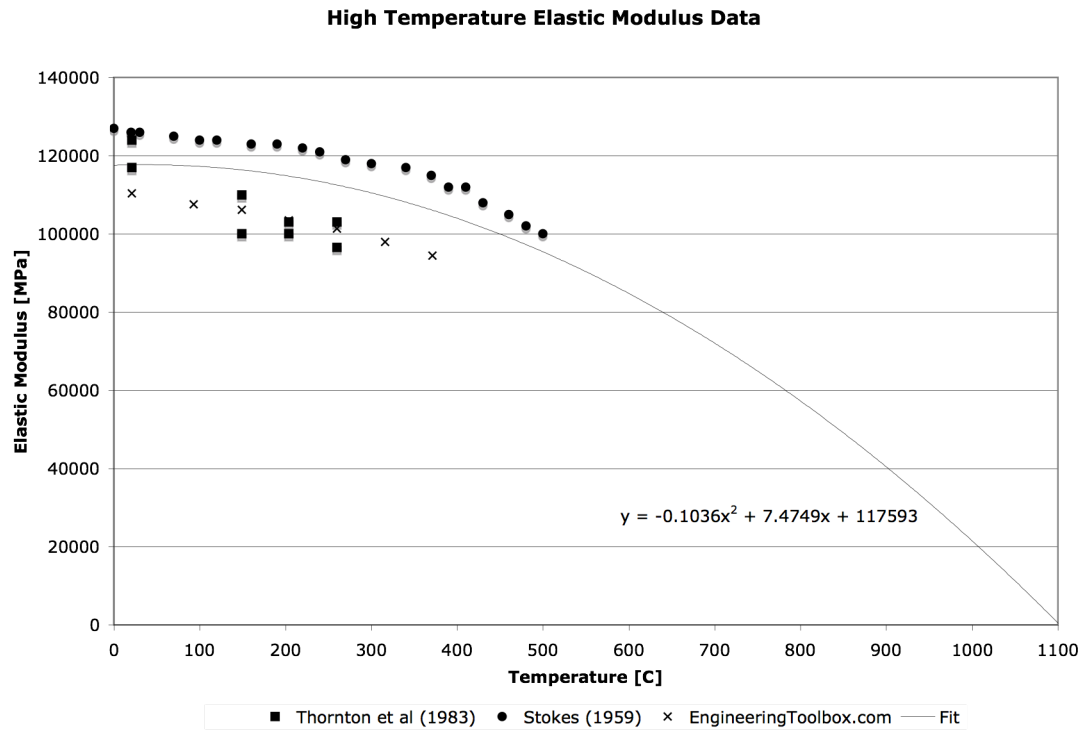
**SECTION A-A
SCALE 1 : 1**

UNLESS OTHERWISE SPECIFIED:		DRAWN BY:	NAME:	DATE:
DIMENSIONS ARE IN INCHES				
TOLERANCES:		CHECKED		
FRACTIONAL: ANGULAR: MACH-2 TWO PLACE DECIMAL: THREE PLACE DECIMAL:		ENG APPR.		
INTERPRETATION: TO LEAVING PER:		MFG APPR.		
COMMENTS:		G.A.		
Copper shims on outside shown for reference only. No fabrication required.				
SIZE:	DWG. NO.:	REV.:		
A	CoreDWG	A		
SCALE: 2:1	WEIGHT:	SHEET 1 OF 3		
3	2	1		

PROPRIETARY AND CONFIDENTIAL
THE INFORMATION CONTAINED IN THIS DRAWING IS THE SOLE PROPERTY OF **INSERER COMPANY NAME HERE**. ANY REPRODUCTION IN PART OR AS A WHOLE WITHOUT THE WRITTEN PERMISSION OF **INSERER COMPANY NAME HERE** IS PROHIBITED.



b. high-temperature copper elastic modulus



At 800° C,

$$y = -0.1036(800)^2 + 7.4749(800) + 117593$$

$$y = 57,269$$

$$\mathbf{E = 57.3 \text{ GPa}}$$

References: Thornton et al. [29], Stokes [28], Engineering Toolbox [27]

C. DESIGN DETAILS PRIOR TO BONDING

*“Omega Readout” describes the VHP onboard pressure readout display.

Tube 1

k = 0

Mean ID measurement: 1.5348 in

Surface area of layer 1: 3751.9925 mm²

Required VHP ram force: 1265 lb

Omega readout: 795

Tube 2

k = 1.0

Mean ID measurement: 1.5335 in

Surface area of layer 1: 3778.99244 mm²

Required VHP ram force: 1274 lb

Omega readout: 802

Tube 3

k = 0.3

Mean ID measurement: 1.5338 in

Surface area of layer 1: 3758.23099 mm²

Required VHP ram force: 1267 lb

Omega readout: 817

Tube 4

k = 0.7

Mean ID measurement: 1.5348 in

Surface area of layer 1: 3773.074 mm²

Required VHP ram force: 1272 lb

Omega readout: 818

Tube 5

k = 0.22

Mean ID measurement: 1.5339 in

Surface area of layer 1: 4272.18653 mm²

Required VHP ram force: 1441 lb

Omega readout: 881

Tube 6

k = 0.22

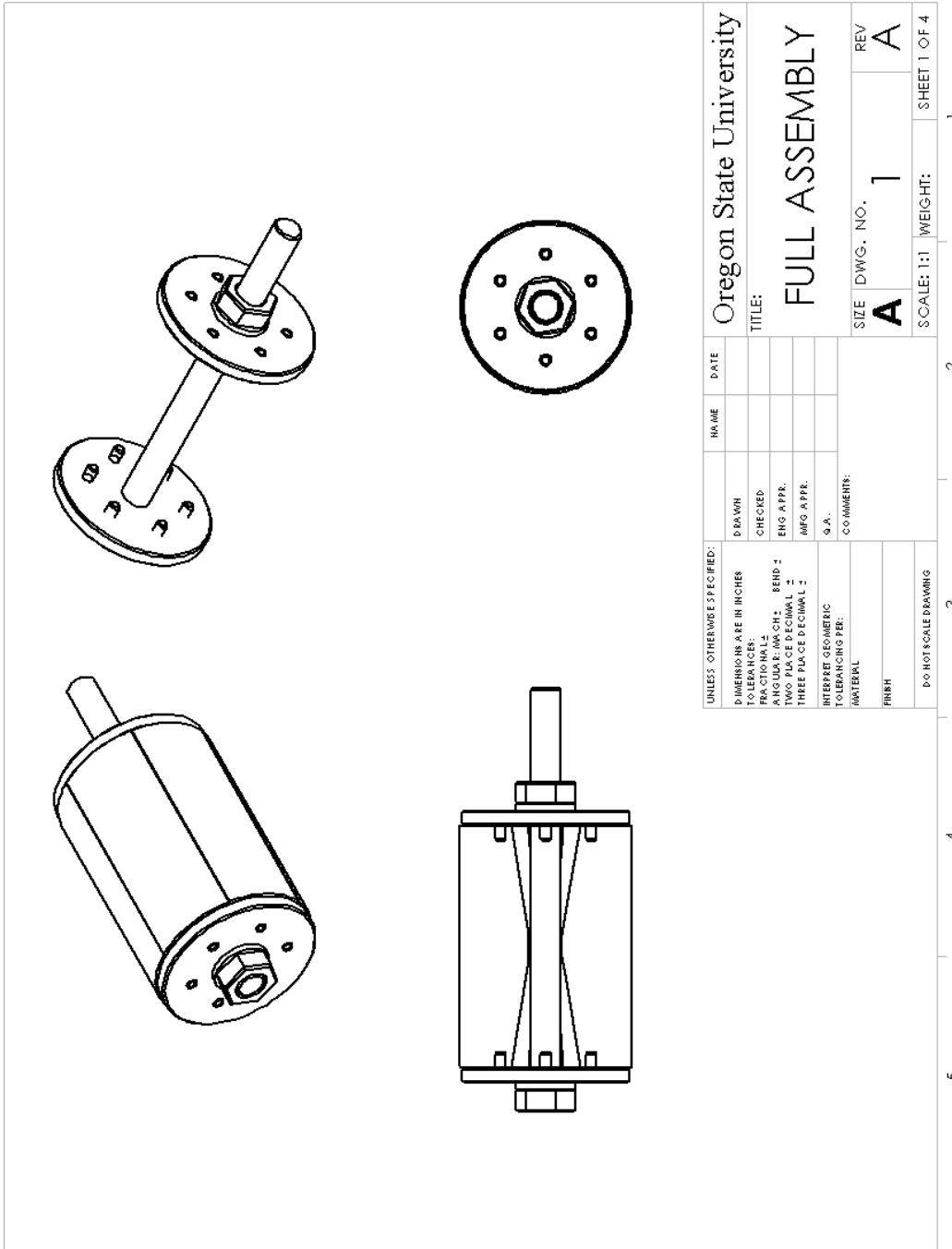
Mean ID measurement: 1.5341 in

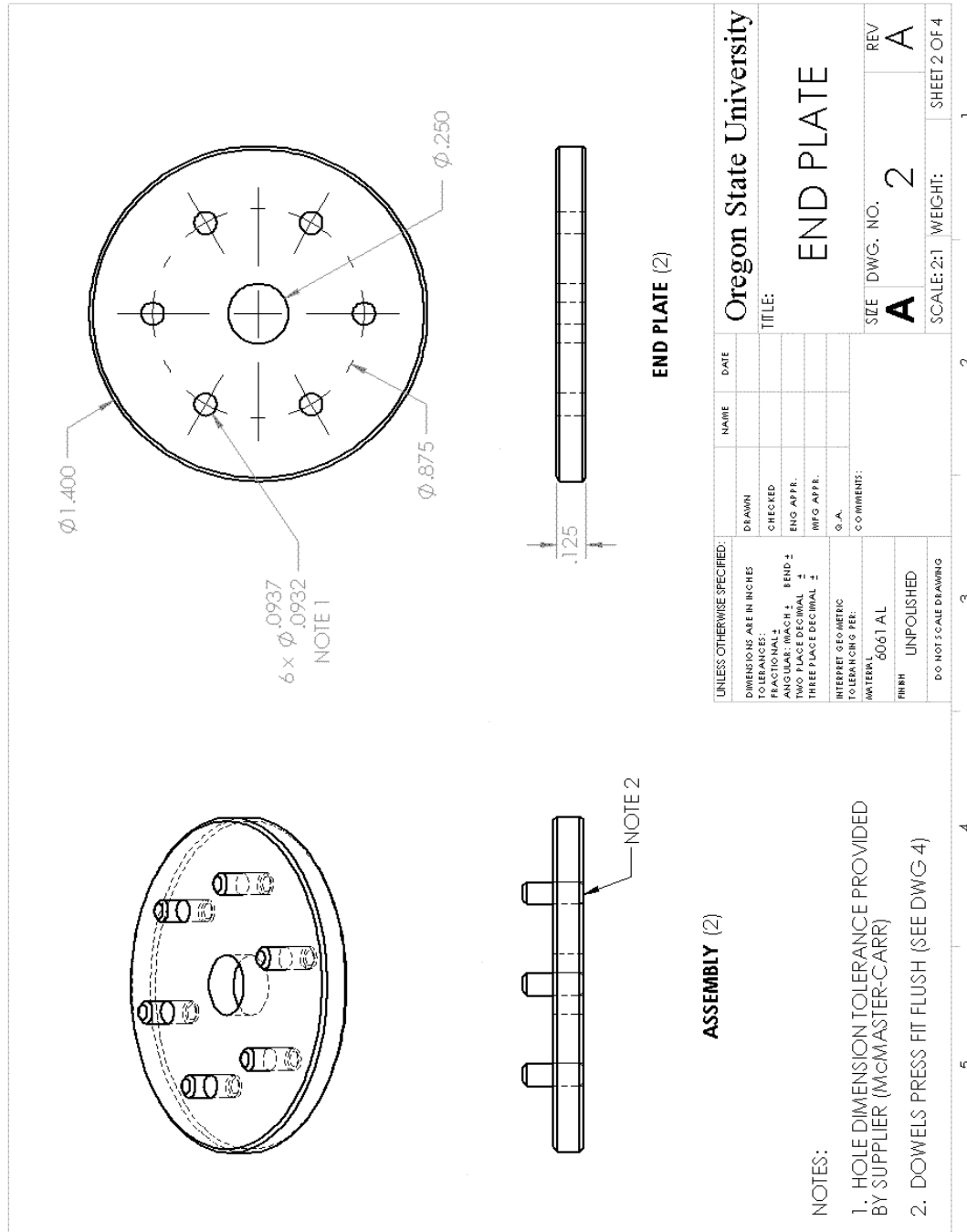
Surface area of layer 1: 4272.79460 mm²

Required VHP ram force: 1441 lb

Omega readout: 880

D. ROTATION FIXTURE DRAWINGS



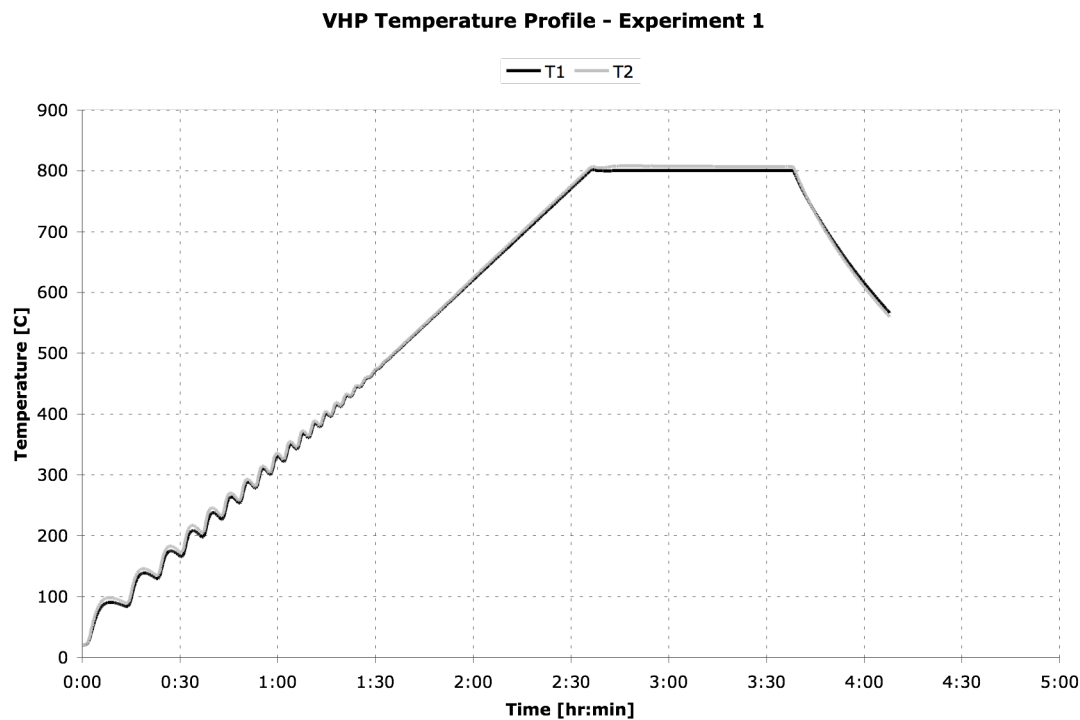


		Oregon State University TITLE: SPACING STUD	
<small>UNLESS OTHERWISE SPECIFIED:</small> DIMENSIONS ARE IN INCHES TOLERANCES: FRACTIONAL: ANGULAR: RADIAL: END: TWO PLACE DECIMAL ONE APPR. THREE PLACE DECIMAL ONE APPR. Q.A. INTERFERING GEOMETRIC TOLERANCING FEATURES MATERIAL: FINISH: BLACK-OXIDE DO NOT SCALE DRAWING		SIZE DWG. NO. REV A 3 A SCALE: 1:1 WEIGHT: SHEET 3 OF 4	
5	4	3	2

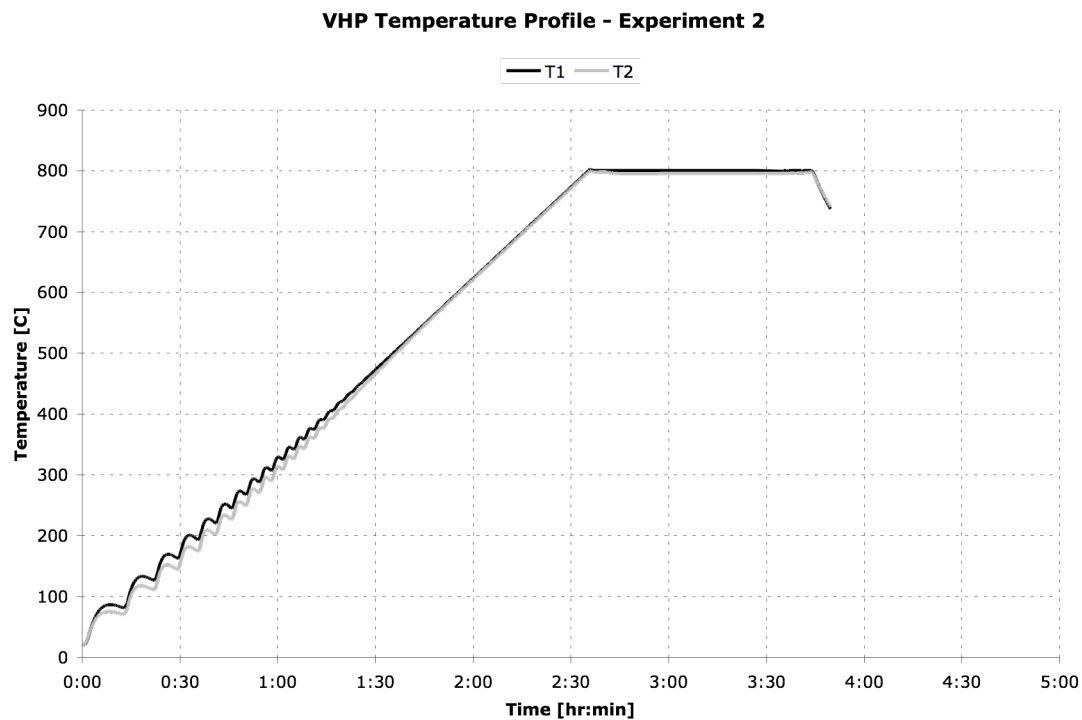
HEX NUT (2)		WASHER (2)		DOWEL (12)													
MATL: STEEL	FINISH: ZINC-PLATED	MATL: STEEL	FINISH: ZINC-PLATED	MATL: STEEL	FINISH: PLAIN												
<p>1/4"-20 THREAD 7/16"</p>		<p>$\phi \frac{17}{64}$ [0.266] Ø.500</p>		<p>$\phi \frac{3}{32}$" .250</p>													
<p>UNLESS OTHERWISE SPECIFIED: DIMENSIONS ARE IN INCHES TOLERANCES: FRACTIONAL: ANGULAR: WHICH 2 BENDS : TWO PLACE DECIMAL : THREE PLACE DECIMAL : INTERPRETATION: ID: DRAWING PER: COMMENTS: MATERIAL: LINE#: DO NOT SCALE DRAWING</p> <p>Oregon State University TITLE:</p> <p>COMPONENTS</p> <table border="1"> <thead> <tr> <th>SIZE</th> <th>DWG. NO.</th> <th>REV</th> </tr> </thead> <tbody> <tr> <td>A</td> <td>4</td> <td>A</td> </tr> <tr> <td></td> <td>SCALE: 2:1</td> <td>WEIGHT:</td> </tr> <tr> <td></td> <td></td> <td>SHEET 4 OF 4</td> </tr> </tbody> </table>						SIZE	DWG. NO.	REV	A	4	A		SCALE: 2:1	WEIGHT:			SHEET 4 OF 4
SIZE	DWG. NO.	REV															
A	4	A															
	SCALE: 2:1	WEIGHT:															
		SHEET 4 OF 4															
5	4	2	3	1													

E. BONDING CYCLE TEMPERATURE PROFILES

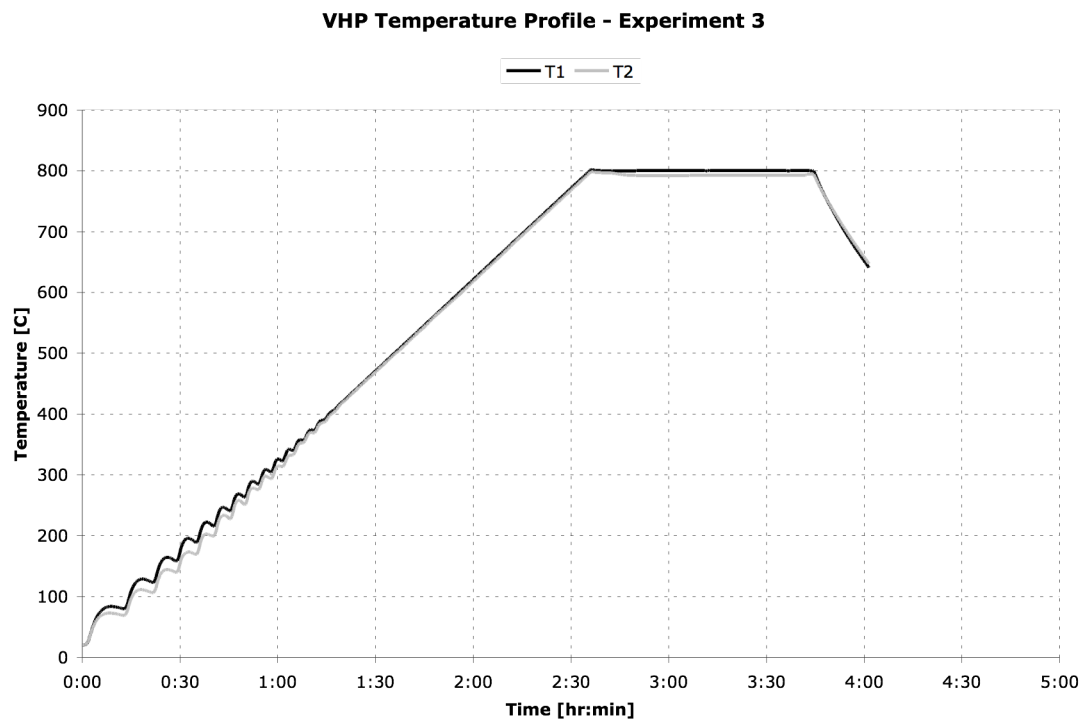
Tube 1:



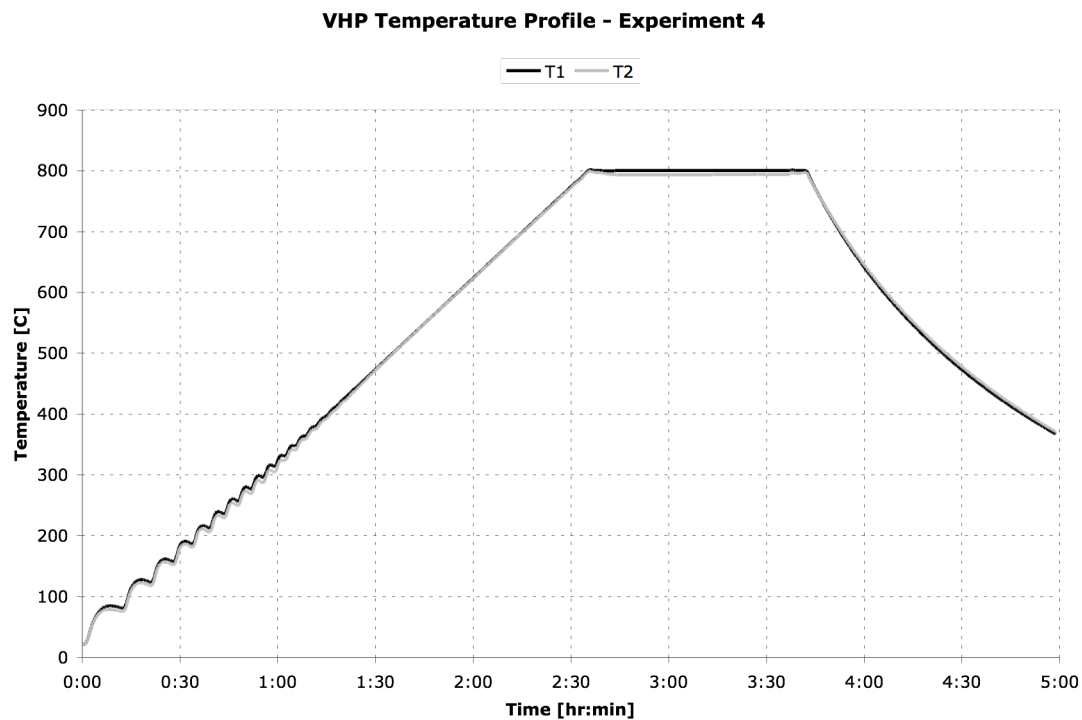
Tube 2:



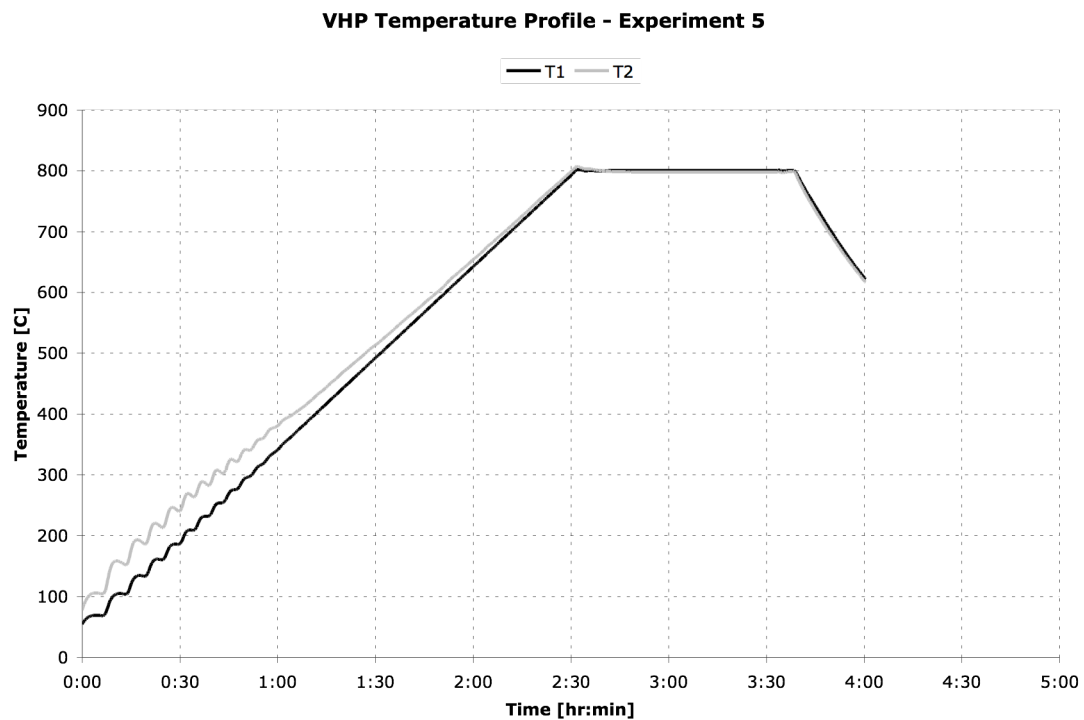
Tube 3:



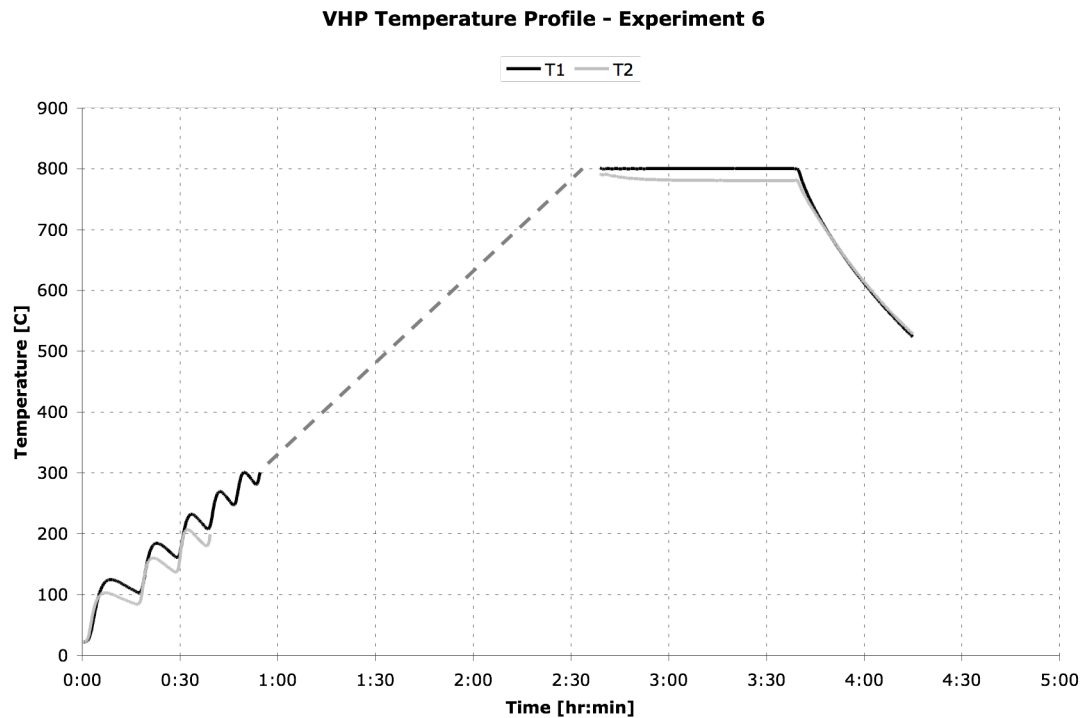
Tube 4:



Tube 5:



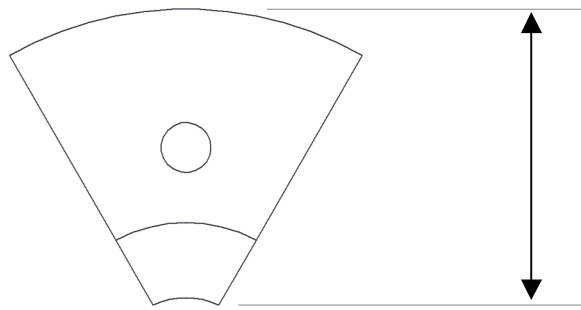
Tube 6:



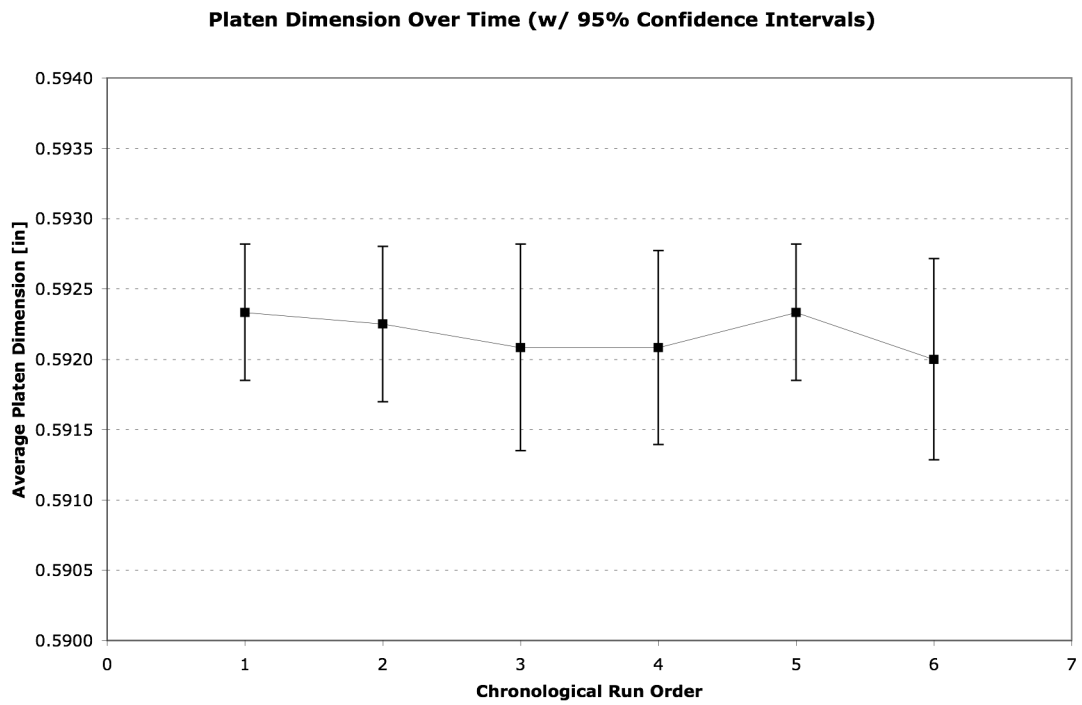
Note: there was a malfunction with the data logger between about minutes 45 and 150. The dashed line represents an estimate of the temperature profile as monitored by eye while fixing the data logger.

F. PLATEN CREEP MEASUREMENTS

The steel platens were measured before and after each run in the following location:

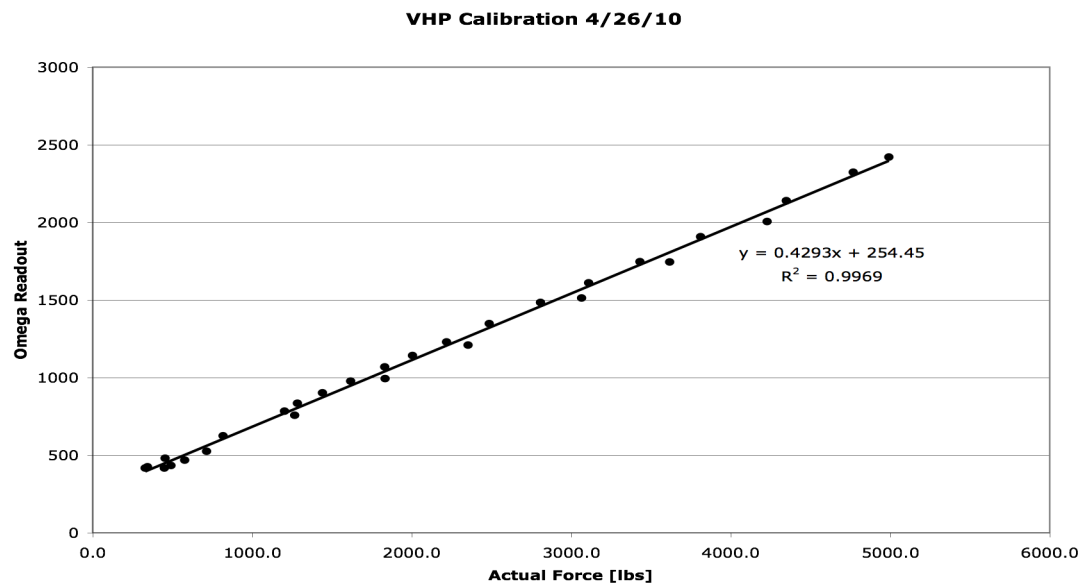
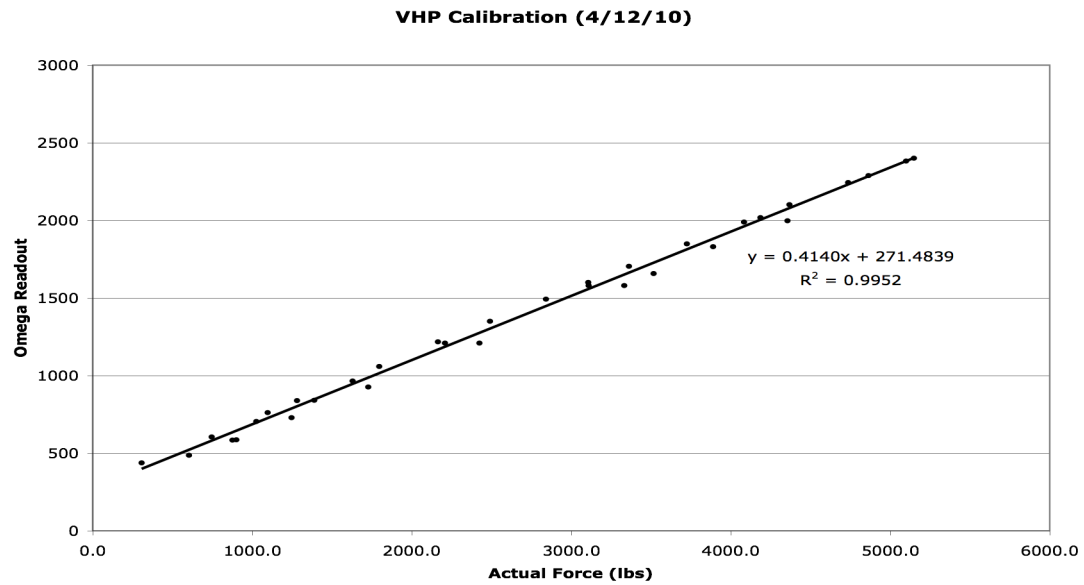


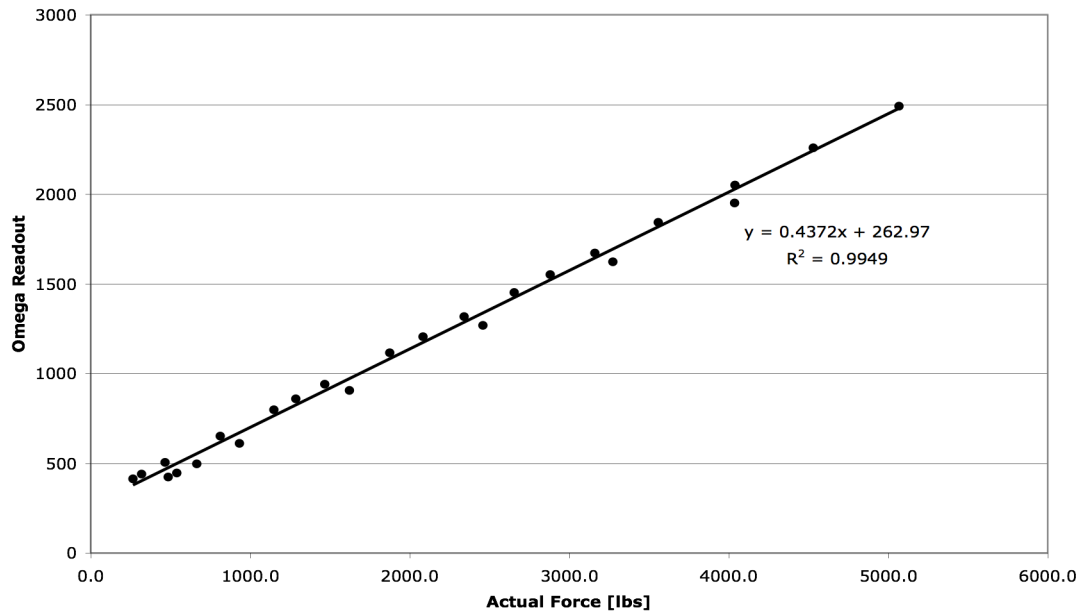
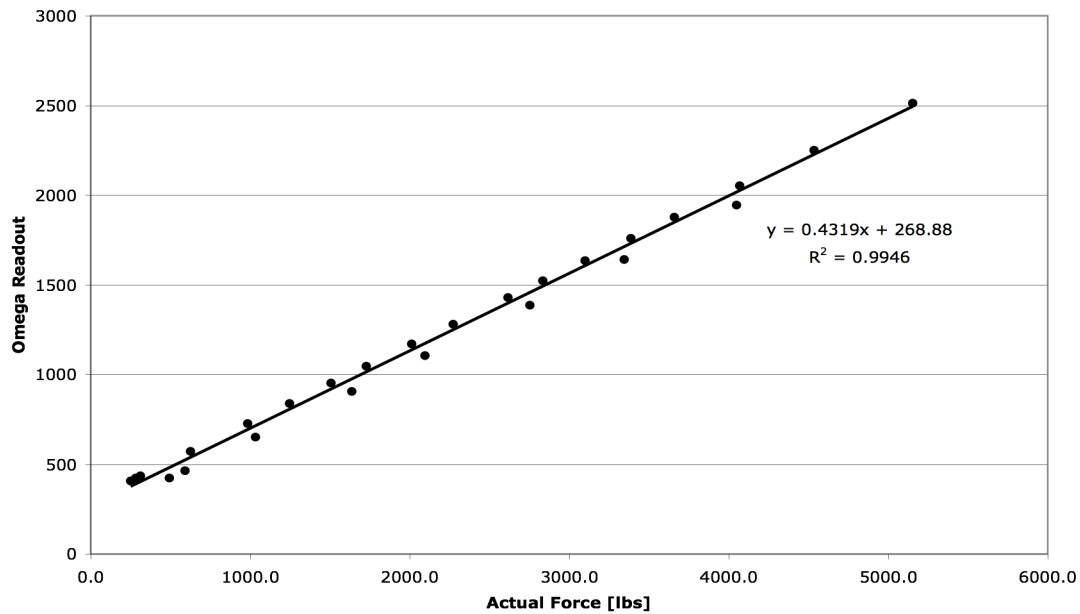
The following plot shows the results of these measurements. No creep was detected.

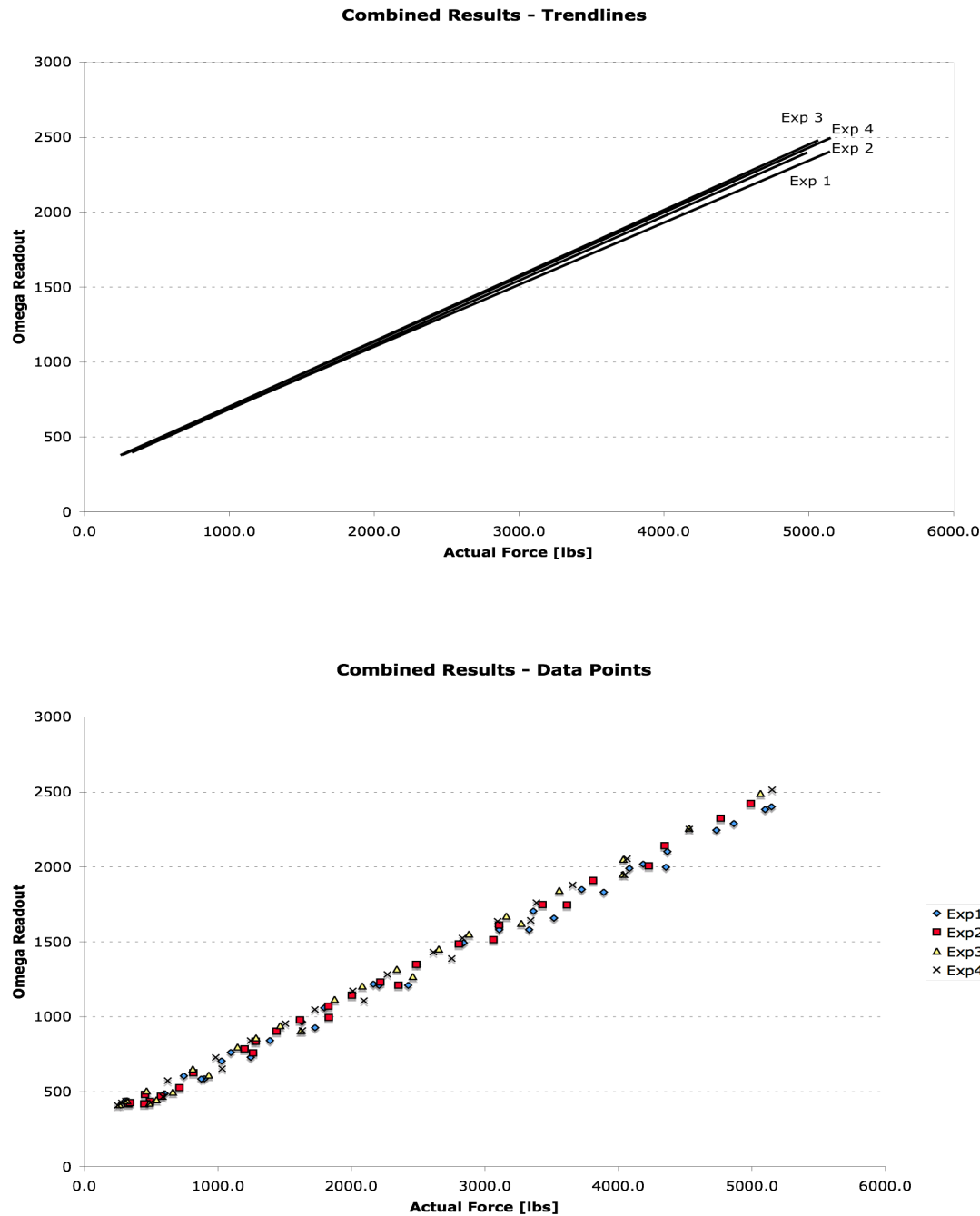


G. VHP PRESSURE MAGNITUDE CALIBRATION

*“Omega Readout” describes the VHP onboard pressure readout display.



VHP Calibration (5/3/10)**VHP Calibration (5/6/10)**



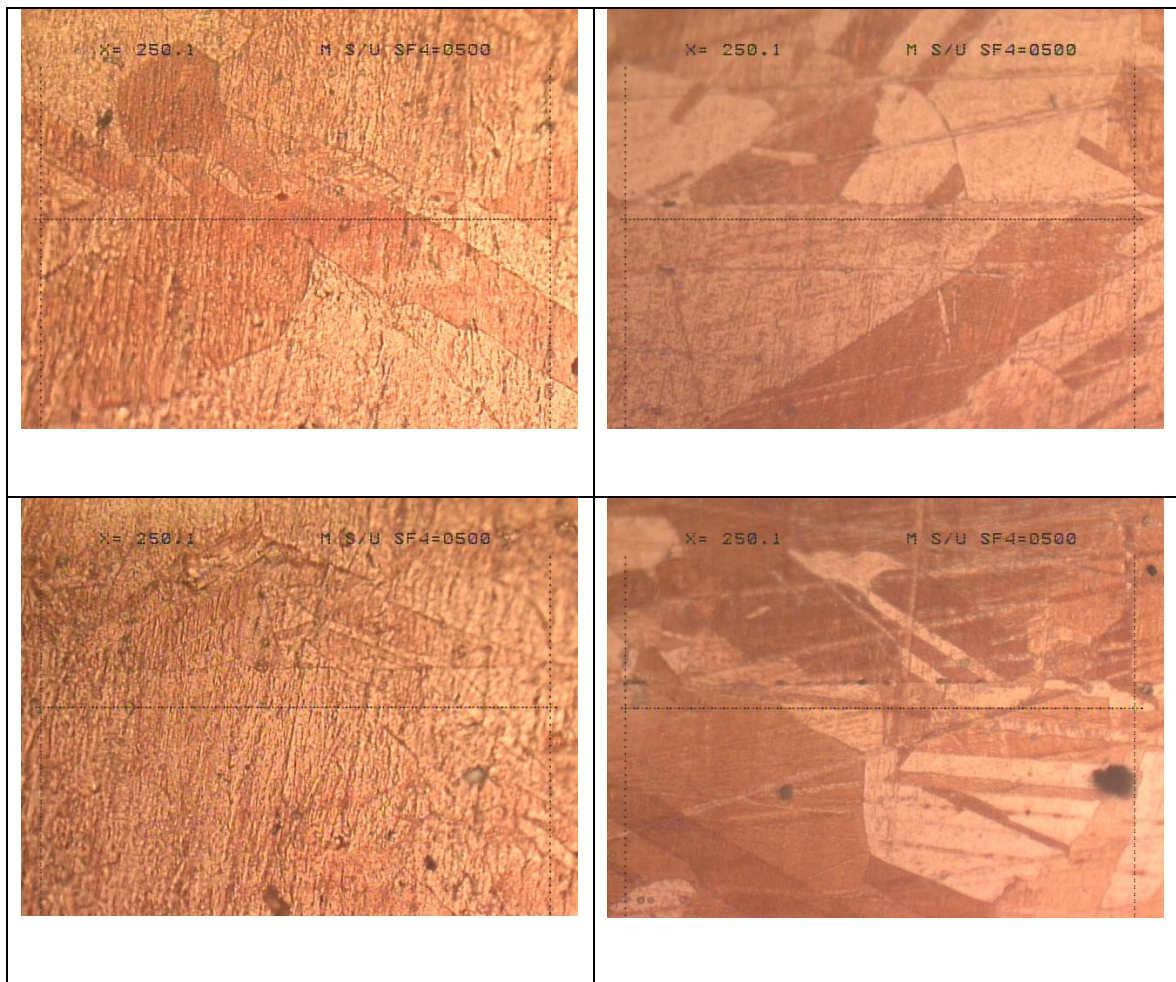
There was no noticeable change in calibration from test to test over time.

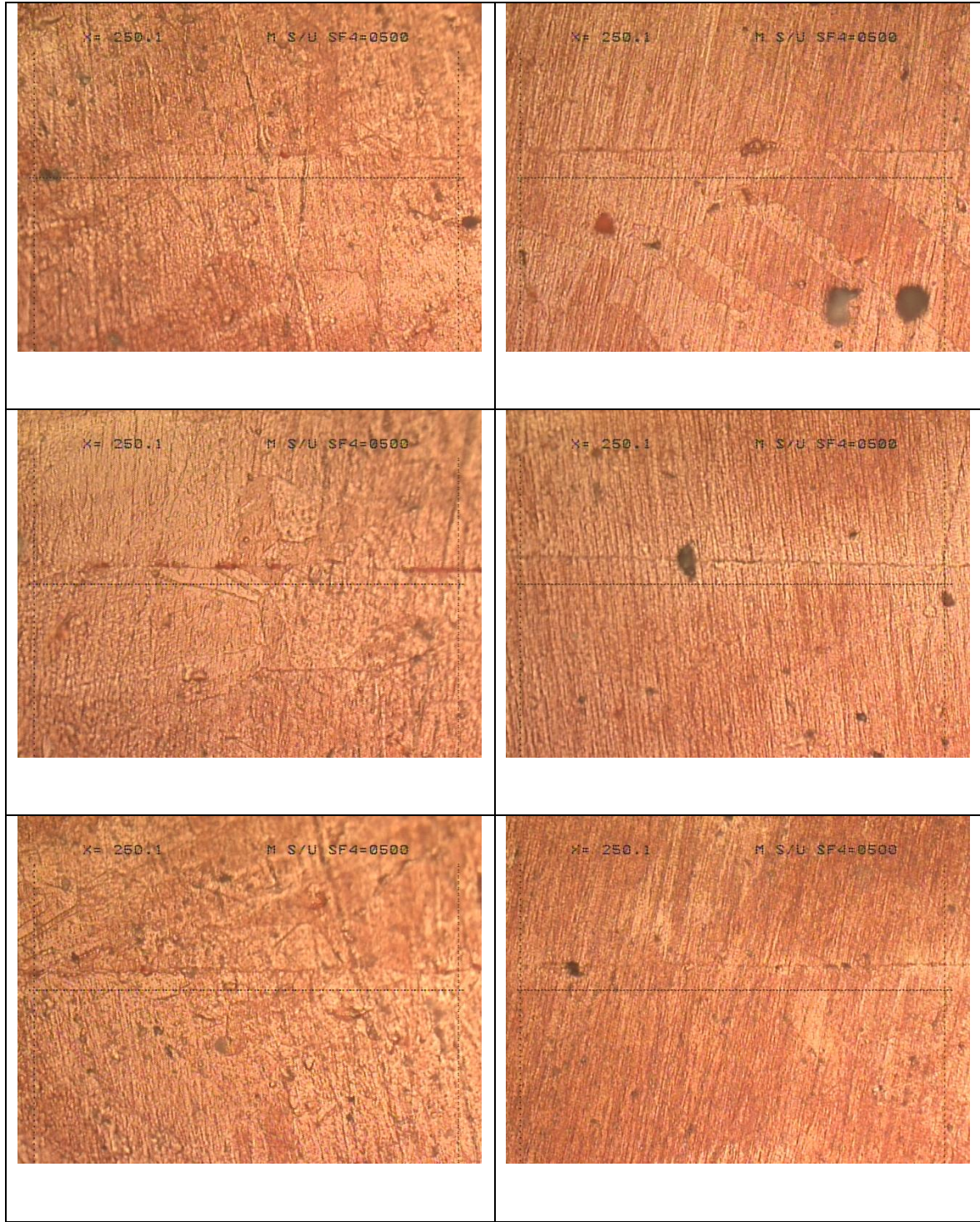
H. VOID FRACTION DETAILED RESULTS

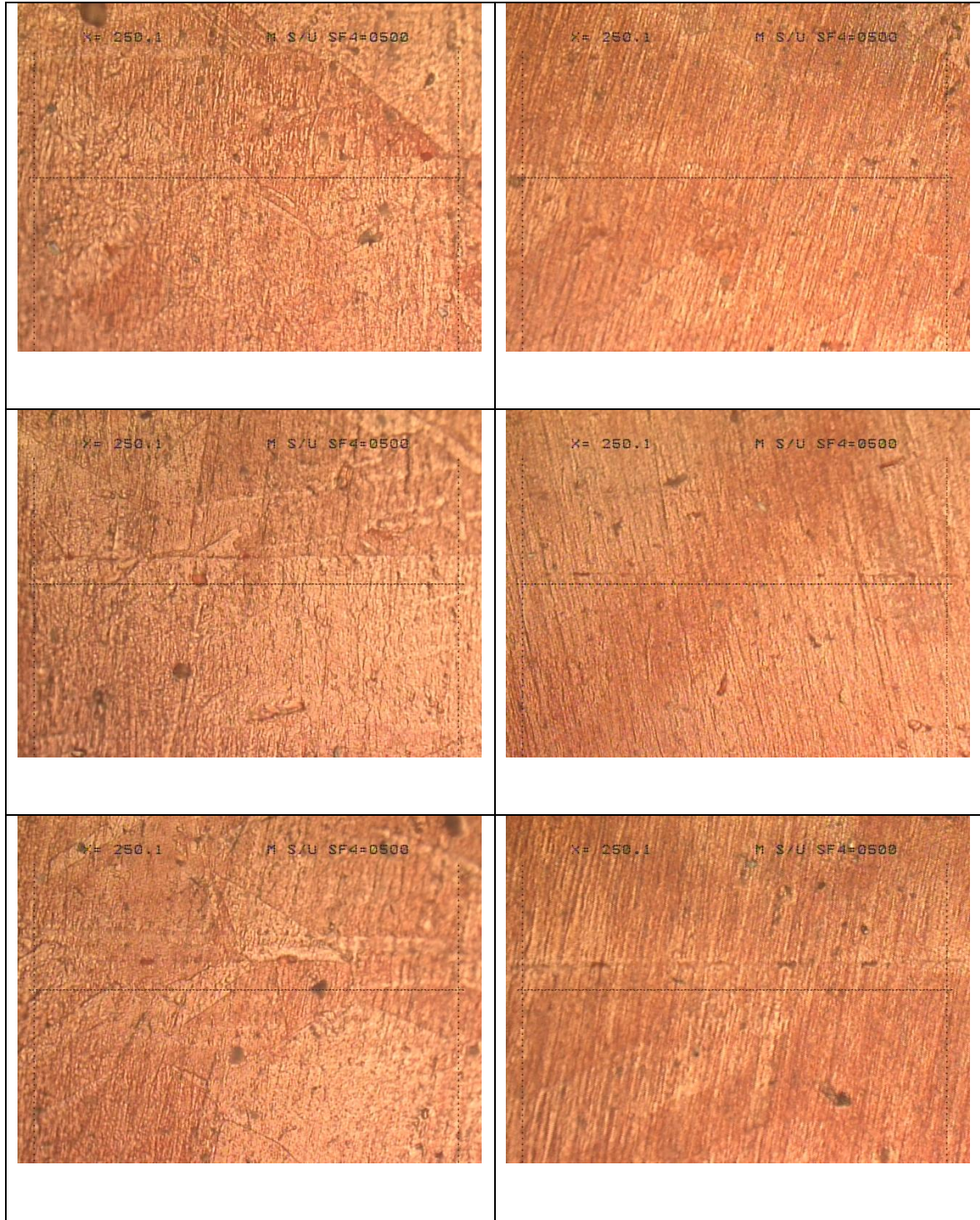
Sample 1:

Center

Edge



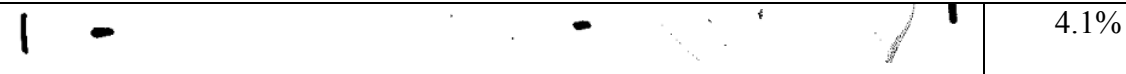
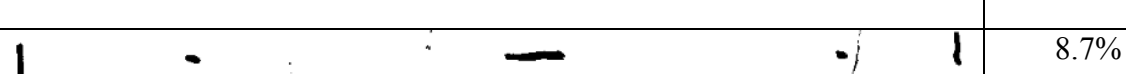
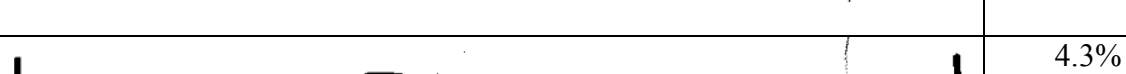
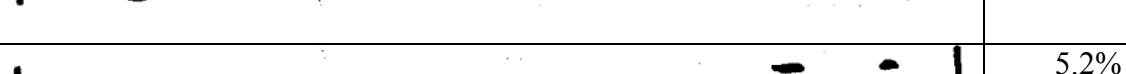
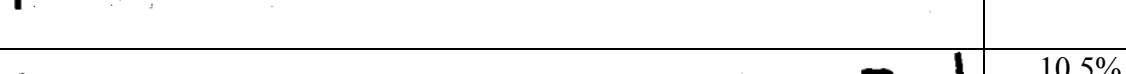


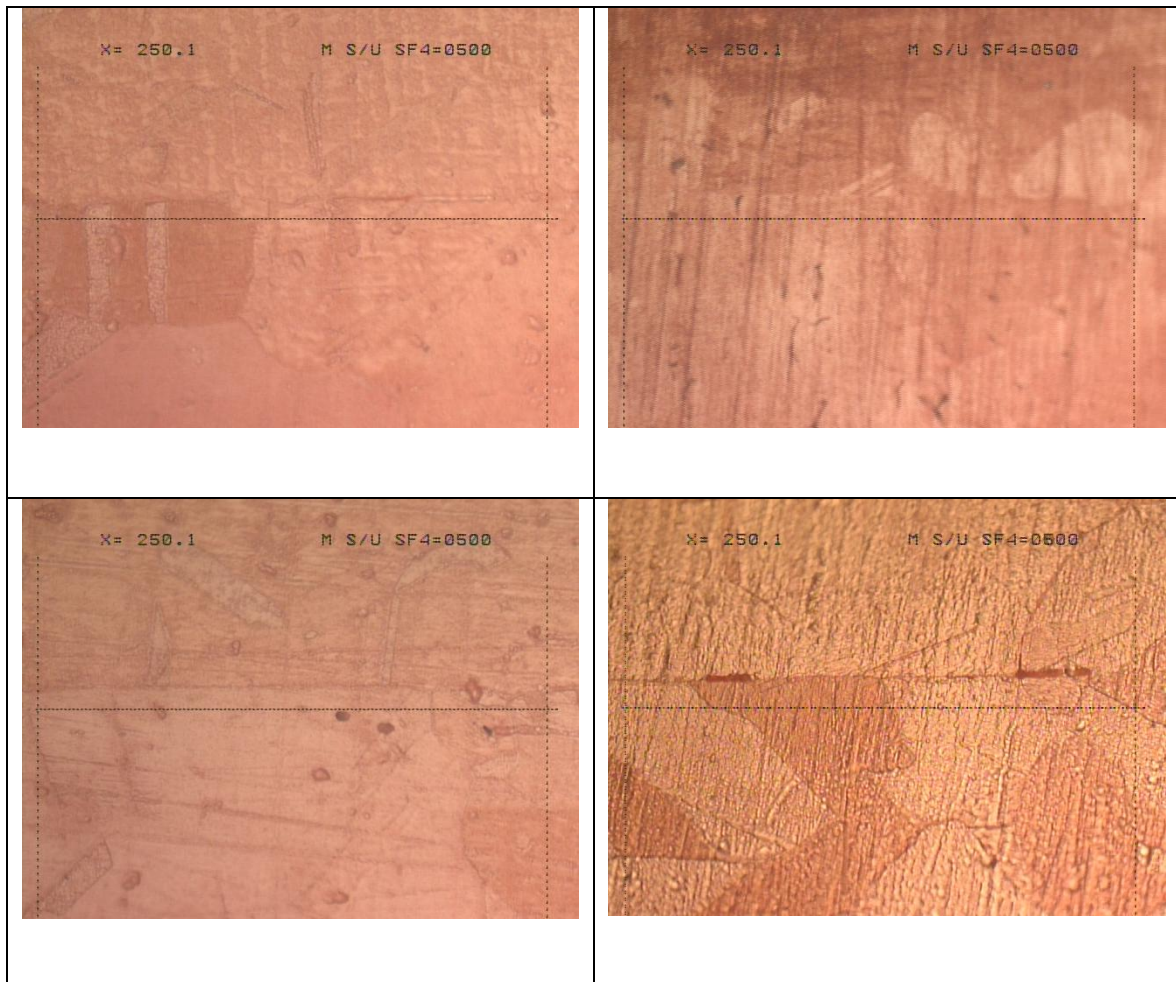


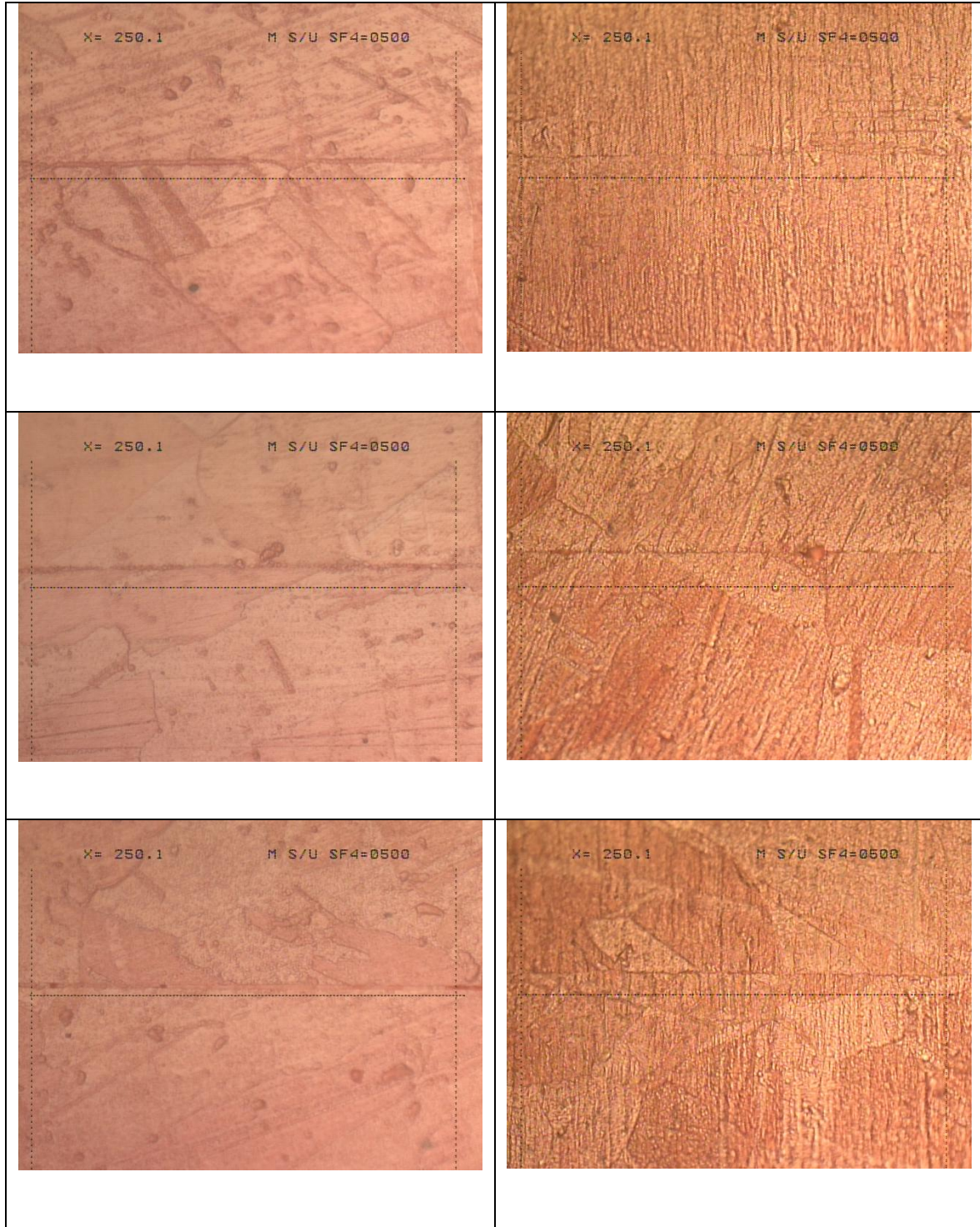
Sample 1, Center Voids:

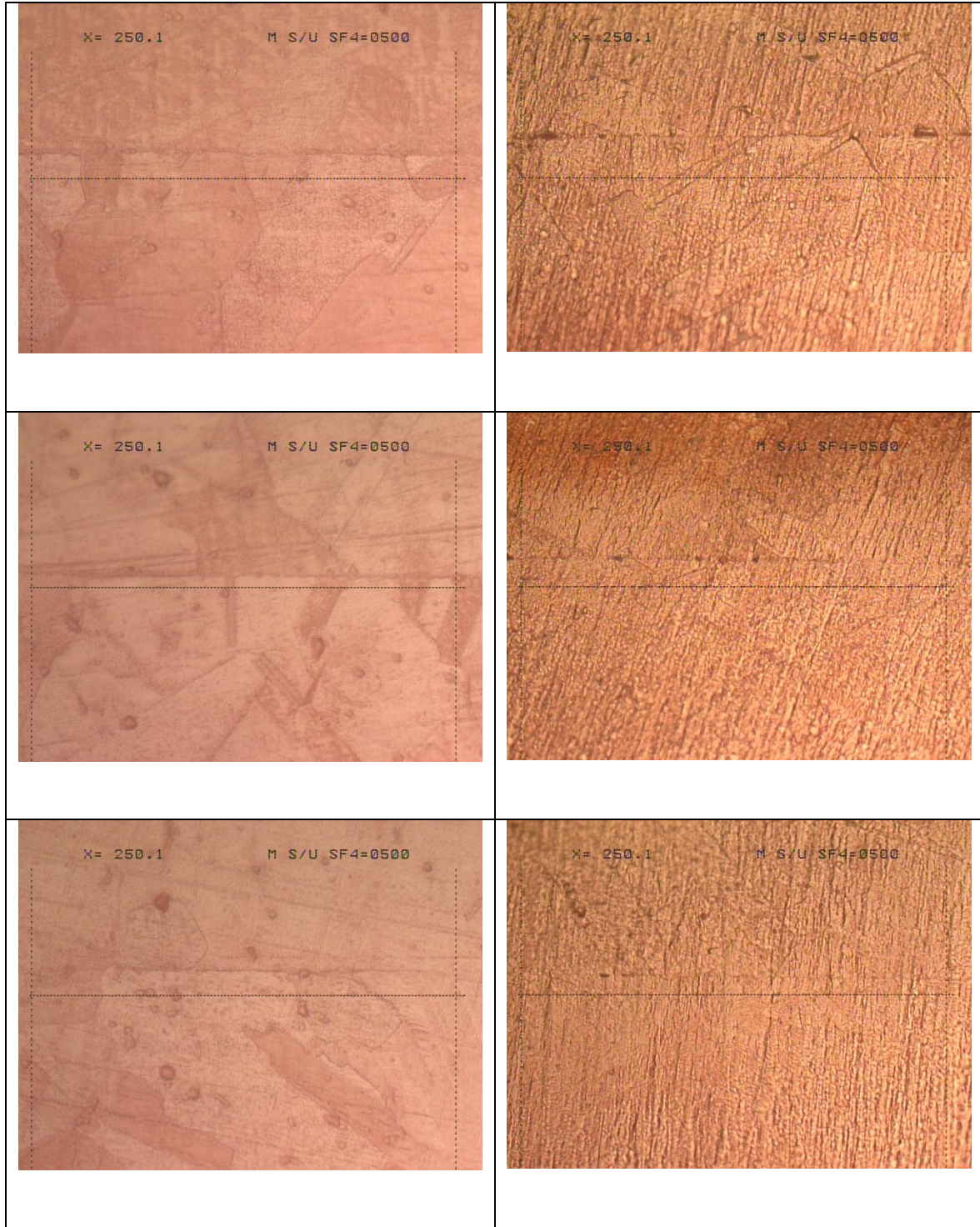
	5.8%
	12.8%
	7.9%
	29.3%
	14.1%
	8.4%
	4.7%
	7.7%
<i>avg 11.4%</i>	

Sample 1, Edge Voids:

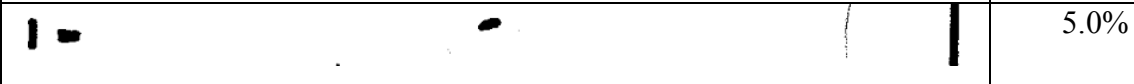
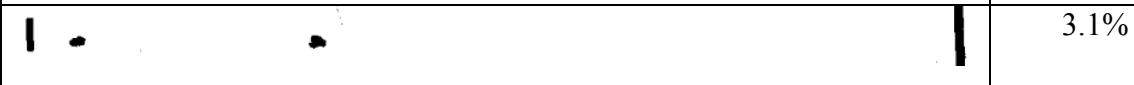
	4.1%
	10.6%
	8.7%
	4.3%
	8.2%
	5.2%
	10.5%
	13.4%
<i>avg 8.1%</i>	

Sample 2:**Center****Edge**



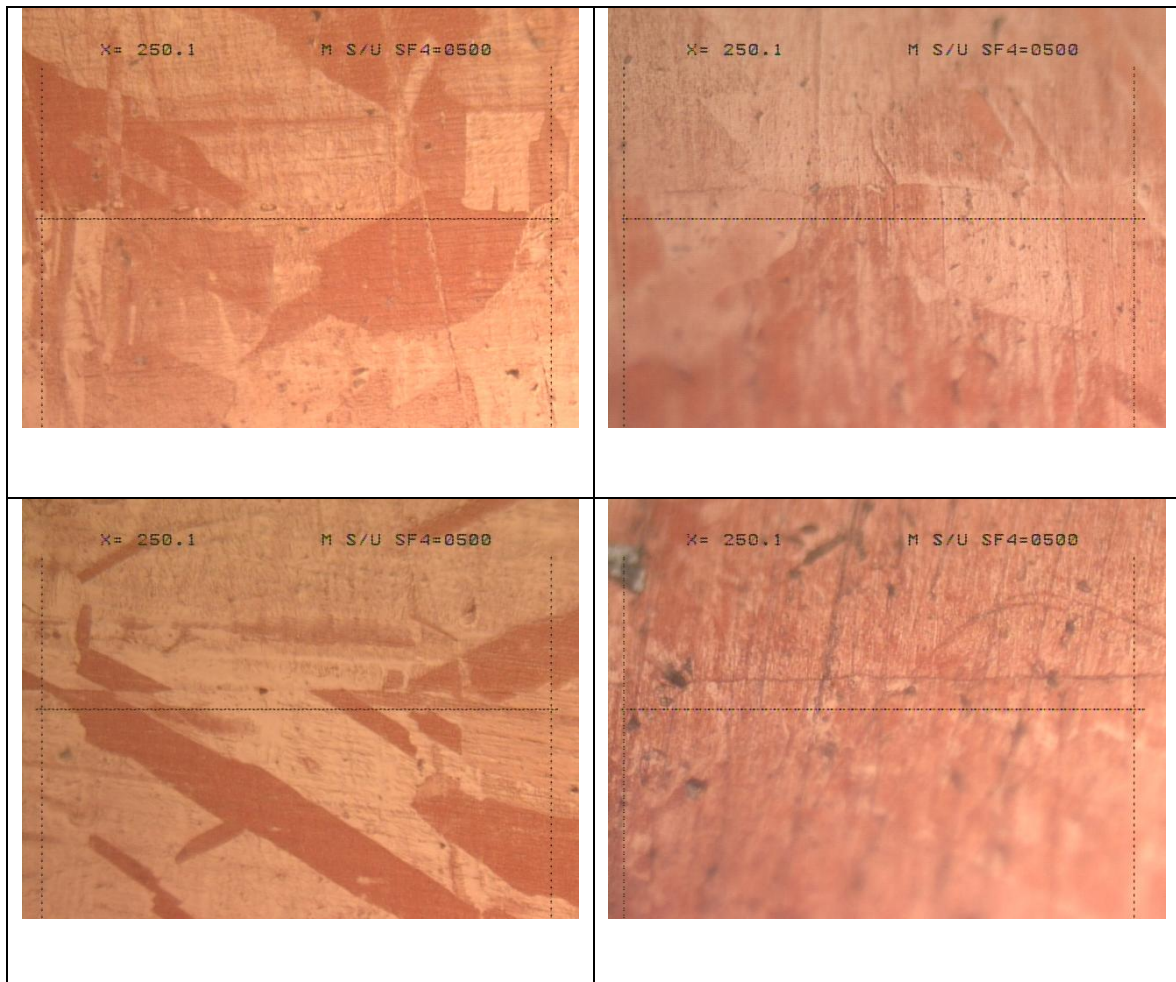


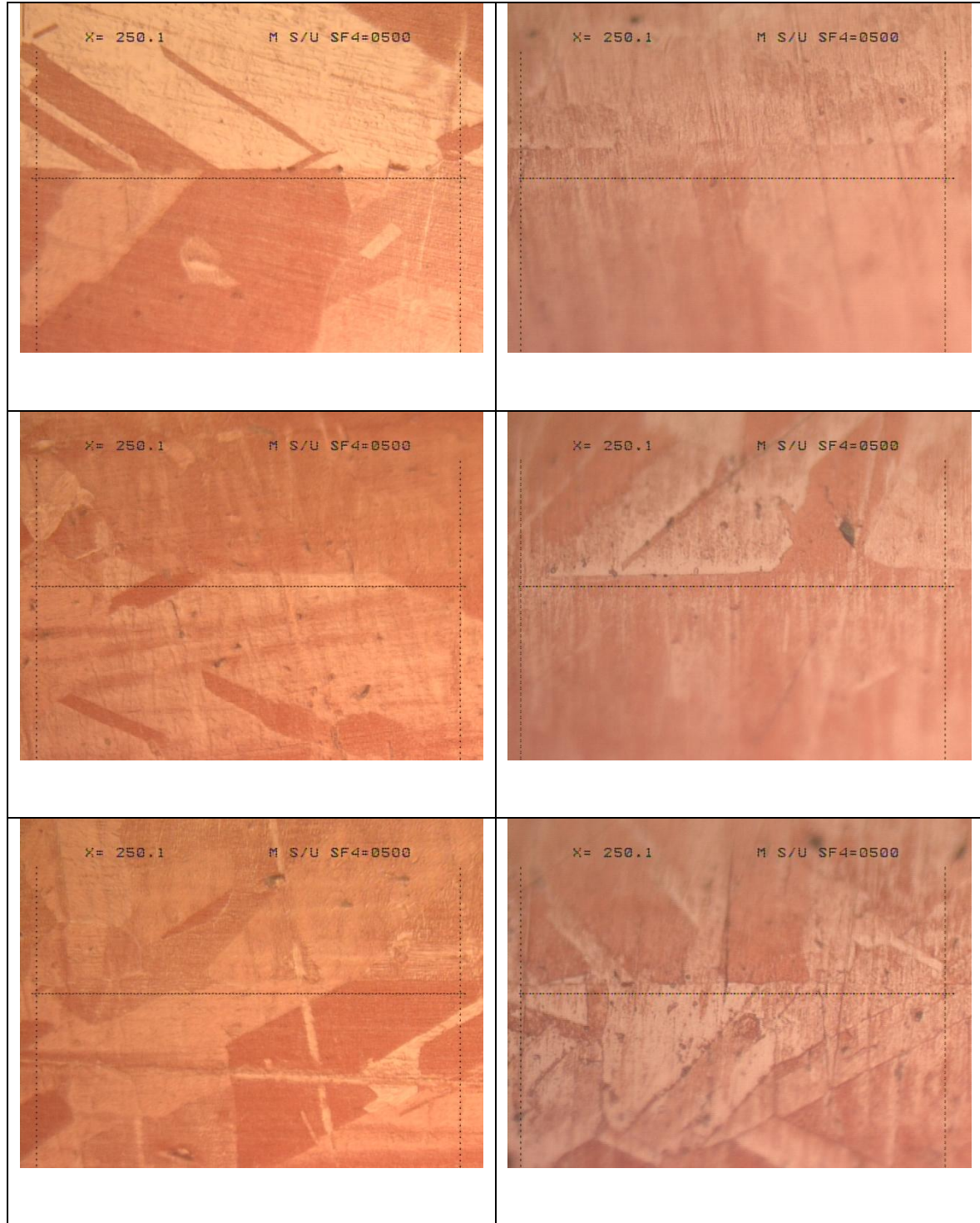
Sample 2, Center Voids:

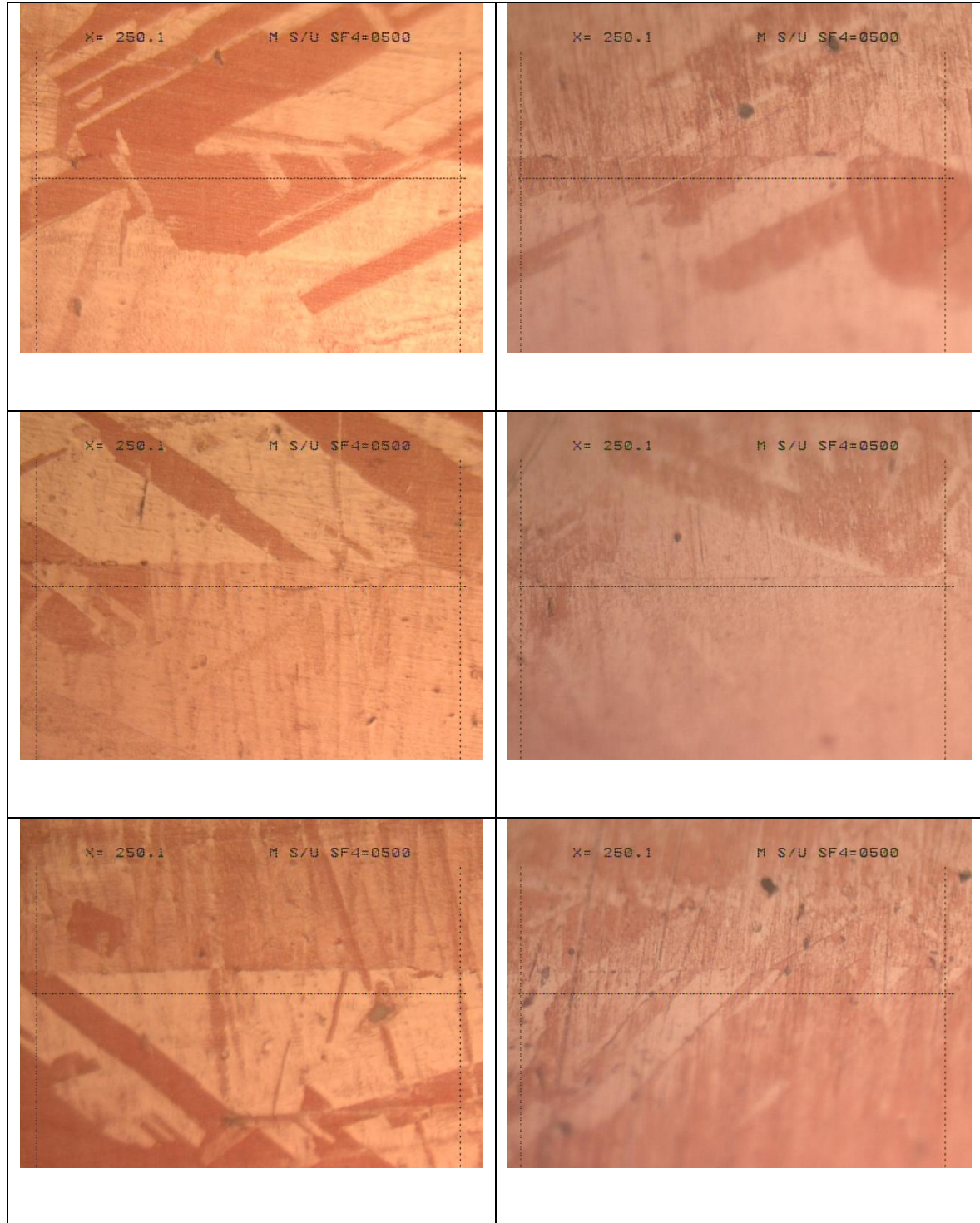
	0.0%
	3.6%
	5.0%
	5.1%
	3.1%
	9.7%
	5.8%
	6.9%
<i>avg 4.9%</i>	

Sample 2, Edge Voids:

	1.3%
	19.0%
	3.3%
	9.8%
	0.0%
	8.8%
	7.2%
	2.0%
<i>avg 6.4%</i>	

Sample 3:**Center****Edge**

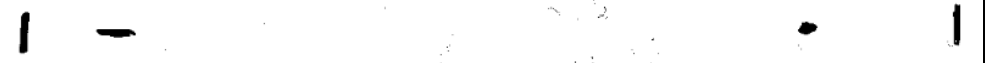
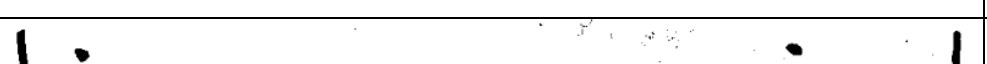
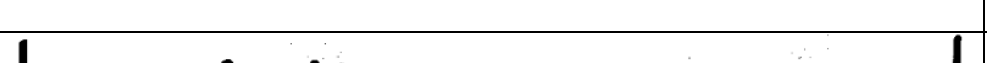
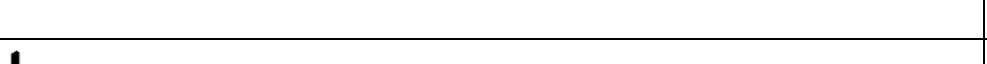
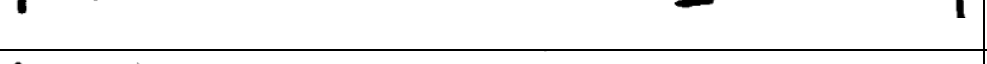


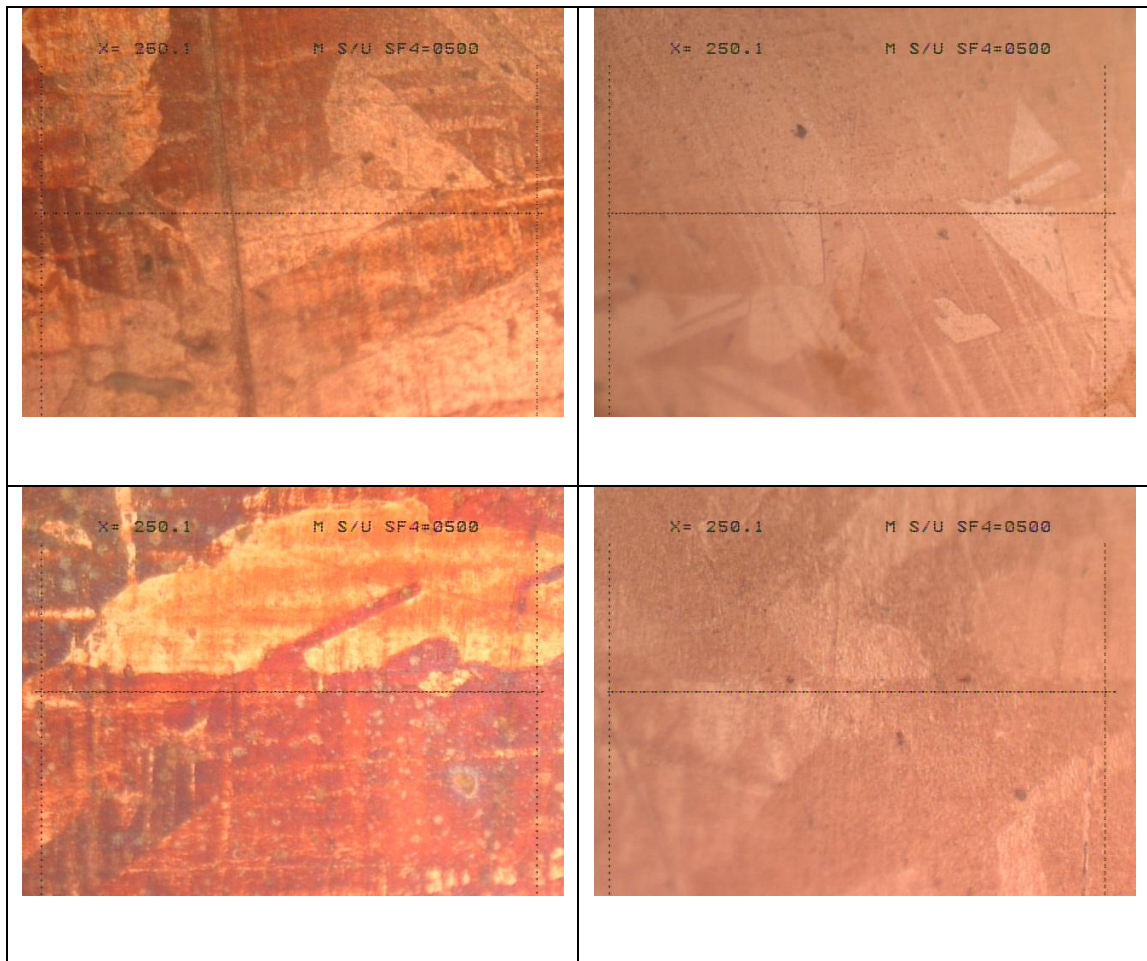


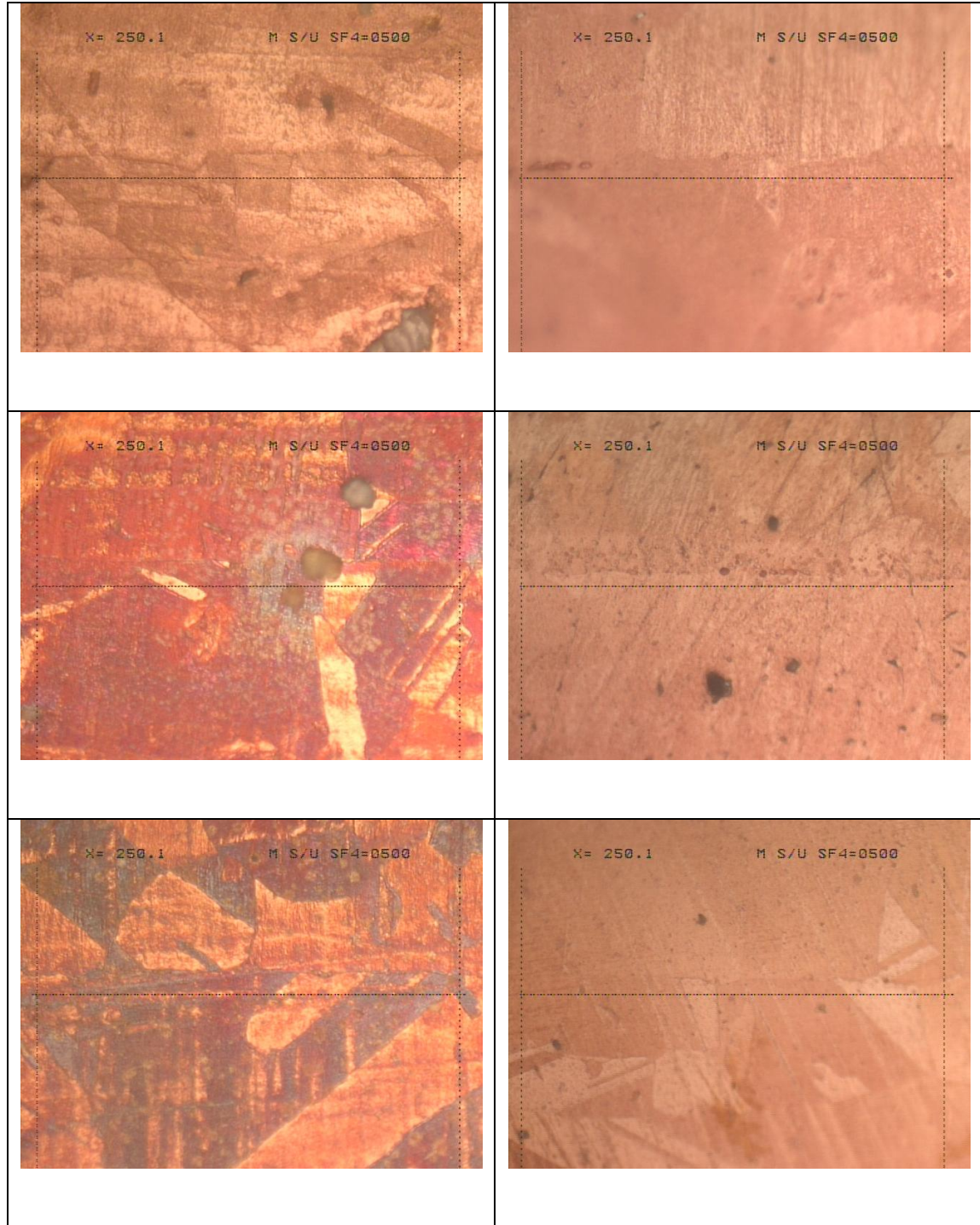
Sample 3, Center Voids:

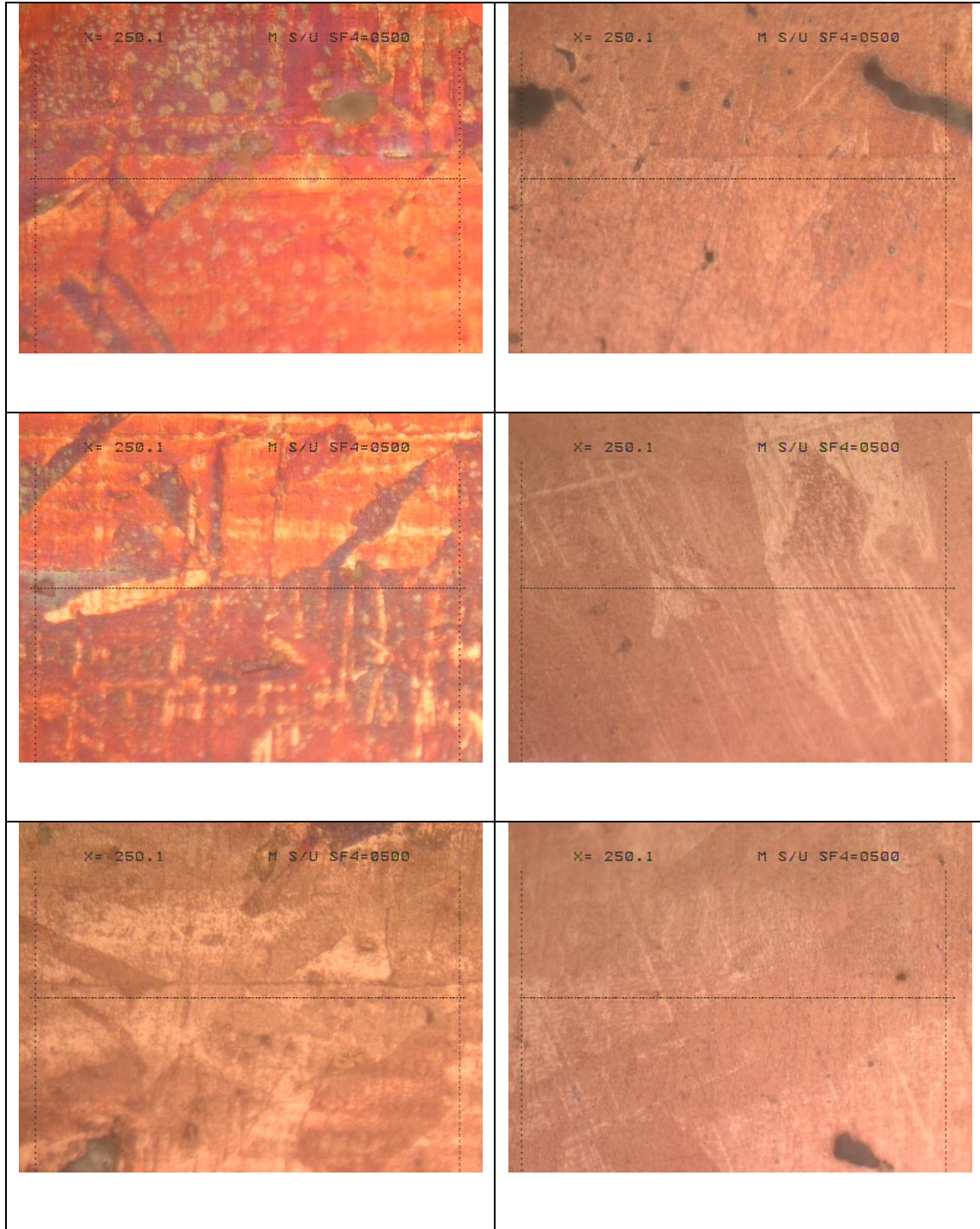
	13.9%
	2.6%
	12.4%
	3.8%
	0.0%
	6.8%
	12.8%
	8.0%
<i>avg 7.5%</i>	

Sample 3, Edge Voids:

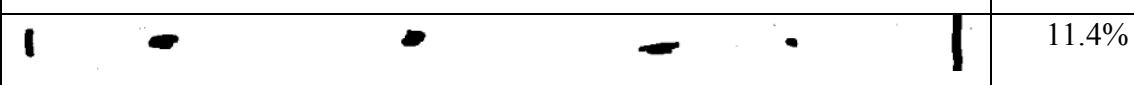
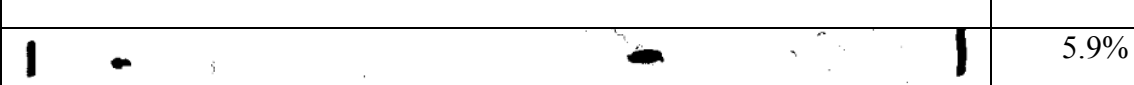
	3.6%
	5.5%
	2.9%
	2.1%
	4.0%
	7.1%
	3.8%
	5.3%
<i>avg 4.3%</i>	

Sample 4:**Center****Edge**





Sample 4, Center Voids:

	7.9%
	8.8%
	8.5%
	13.3%
	11.4%
	11.1%
	6.7%
	5.9%
<i>avg 9.2%</i>	

Sample 4, Edge Voids:

	2.2%
	3.4%
	12.8%
	7.7%
	4.2%
	7.5%
	0.0%
	3.3%
<i>avg 5.1%</i>	

Void Fraction Results Summary

	<u>Center</u>	<u>Edge</u>	<u>Total</u>
<i>Mean</i>	8.2%	6.0%	7.1%
<i>Standard Deviation</i>	5.4%	4.2%	4.9%
<i>95% Confidence</i>	1.9%	1.5%	1.2%

I. MISALIGNMENT DETAILED RESULTS

k	Exp1 0	Exp2 1	Exp3 0.3	Exp4 0.7
1	-593	1549	456	1118
2	-616	1635	436	1237
3	-636	1615	413	1220
4	-680	1656	423	1268
5	-687	1618	444	1232
6	-672	1719	403	
7	-667	1689	393	1255
8	-712	1732	431	1260
9	-639	1711	406	1222
10	-771	1696		
11	-687		423	
12	-809	1711	373	1407
13	-728	1694	396	1263
14	-809	1823	319	1430
15	-712	1711	373	1318
16	-936	1962	193	1592
Average	-709.6	1701.4	392.1	1294.0
Standard deviation	86.8	95.8	64.7	120.3
Confidence*	42.5	48.5	32.7	65.4

*alpha 0.05

<u>Label</u>	<u>Aspect Ratio</u>	<u>1-3</u>	<u>Layers</u>
			<u>3-5</u>
			<u>1-5</u>
5a	5	1113	269
	5	1083	256
	10	1047	218
	10	1123	259
5b	5	900	3
	5	925	58
	10	832	51
	10	946	10
5c	5	969	170
	5	1095	218
	10	956	101
	10	966	152
5d	5	728	-122
	5	837	-81
	10	700	-167
	10	776	-117
6a	5	1699	583
	5	1752	624
	10	1714	568
	10	1739	616
6b	5	1466	426
	5	1592	479
	10	1395	365
	10	1519	439
6c	5	1445	350
	5	1318	322
	10	1192	205
	10	1384	340
6d	5	1696	515
	5	1732	601
	10	1557	479
	10	1749	578

Summary**Experiment #5**

Average	937	80	1017
Std. Deviation	135	148	281
Confidence	66	73	138

Experiment #6

Average	1559	468	2027
Std. Deviation	178	125	302
Confidence	87	61	148

TOTAL

Average	1248	274	1522
Std. Deviation	352	239	588
Confidence	122	83	204

